PHOTONIC ENTANGLEMENT: NEW SOURCES AND NEW APPLICATIONS

JIŘÍ SVOZILÍK

ICFO - INSTITUTO DE CIÈNCIAS FOTÓNICAS

UNIVERSIDAD POLITÈCNICA DE CATALUÑA

BARCELONA, 2014

PHOTONIC ENTANGLEMENT: NEW SOURCES AND NEW APPLICATIONS

JIŘÍ SVOZILÍK

under the supervision of

PROFESSOR JUAN P. TORRES

submitted this thesis in partial fulfilment of
the requirements for the degree of

DOCTOR

by the

UNIVERSIDAD POLITÈCNICA DE CATALUÑA
BARCELONA, 2014

To my daughter Klára.

Acknowledgement

Writing a dissertation thesis is and will be always a challenging task. Therefore, I would like to express, first and foremost, my deepest gratitude to my adviser prof. Juan P. Torres for his generous support and guidance during last four years, that pushed me towards the finalization of this thesis. Many thanks belong to my friend and colleague Roberto de Jesús León-Montiel for illuminating discussions during our studies. I am grateful to Martin Hendrych for his encouraging support during my initial years of joining ICFO. Also, I want to thank my colleagues Adam Vallés Marí, Luís José Salazar-Serrano, Carmelo Rosales Guzmán, Valeria Rodríguez Fajardo, Silvana Palacios Álvarez, Alejandro Zamora, Venkata Ramaiah Badarla, Rafael Betancur and Nathaniel Hermosa for their friendship and support through all these years.

A very special thanks belong to my friends Angélica Santis, Anaid Rosas, and Yannick Alan de Icaza Astiz. Additionally, I would like also to express my gratitude to my colleagues from Palacký University in Olomouc, namely to Jan Peřina Jr., Dalibor Javůrek, Radek Machulka and Jan Soubusta.

Most importantly, my greatest thanks go to my family.

Jiří Svozilík, *16 May 2014, Barcelona*

Statement of originality

I hereby declare that this thesis is my own work and that, to the best of my knowledge and belief, it contains no material previously published or written by another person nor material which to a substantial extent has been accepted for the award of any other degree or diploma of the university or other institute of higher learning, except where due acknowledgement has been made in the text.

Jiří Svozilík, *16 May 2014, Barcelona*

Abstract

Non-classical correlations, usually referred as *entanglement*, are ones of the most studied and discussed features of Quantum Mechanics, since the initial introduction of the concept in the decade of 1930s. Even nowadays, a lot of efforts, both theoretical and experimental, are devoted in this topic, that covers many distinct areas of physics, such as a quantum computing, quantum measurement, quantum communications, solid state physics, chemistry and even biology. The fundamental tasks that one should consider related to the entanglement are:

- How to *create* quantum entangled states.
- How to *maintain* entanglement during propagation against sources of decoherence.
- How to *effectively* detect it.
- How to *employ* the benefits that entanglement offers.

This thesis, divided into four chapters, concentrates on the first and last tasks considered above.

In Chapter 1, a brief introduction and overview of what it is entanglement is given, starting with the famous paper of Einstein, Podolsky and Rosen, and continuing with John Bell's formulation of the so-called Bell's inequalities. We define here general concepts about entangled quantum states and introduce important entanglement measures, that are later used all over the thesis. In this chapter, sources of entangled particles (namely photons) are also mentioned. The importance is put on sources based on the nonlinear process of spontaneous parametric down-conversion. The last part of this chapter is then dedicated to a list of applications that benefit from the use of entangled states.

Chapter 2 is devoted to the systematic study of the generation of entangled and non-entangled photon pairs in semiconductor Bragg reflection waveguides. Firstly, we present a source of photon pairs with a spectrally uncorrelated two-photon amplitude, achieved by a proper tailoring of the geometrical and material dispersions via structural design of

waveguides. Secondly, Bragg reflection waveguides are designed in a such way, that results in the generation of spectrally broadband paired photons entangled in the polarization degree of freedom. Finally, we present experimental results of entangled photon pairs generation in this type of structures.

In Chapter 3, we explore the feasibility of the generation of photon pairs entangled in the spatial degree of freedom, i.e. in the orbital angular momentum (OAM). Firstly, we examine how to create a highly multidimensional Hilbert space using OAM modes obtained in a chirped-poled nonlinear bulk crystals. Here, we show, how an increase of the chirp of the poling can effectively increase the Schmidt number by several orders of magnitude. Secondly, we investigate periodically poled silica glass fibres with a ring-shaped core, that are capable to support the generation of simple OAM modes.

The final Chapter 4 is dedicated to the Anderson localization and quantum random walks. At the beginning of this chapter, we present an experimental proposal for the realization of a discrete quantum random walk using the multi-path Mach-Zehnder interferometer with a spatial light modulator, that allows us to introduce different types of statistical or dynamical disorders. And secondly, we show how the transverse Anderson localization of partially coherent light, with a variable first-order degree of coherence, can be studied making use of entangled photon pairs.

Thesis is based on following publications

J. Svozilík, M. Hendrych, A. S. Helmy, and J. P. Torres, *Generation of paired pho- tons in a quantum separable state in bragg reflection waveguides*, Opt. Express **19**, 3115 (2011).

J. Svozilík, M. Hendrych, and J. P. Torres, *Bragg reflection waveguide as a source of wavelength-multiplexed polarization-entangled photon pairs*, Opt. Express **20**, 15015 (2012).

A. Valles, M. Hendrych, **J. Svozilík**, R. Machulka, P. Abolghasem, D. Kang, B. J. Bijlani, A. S. Helmy, and J. P. Torres, *Generation of polarization-entangled photon pairs in a bragg reflection waveguide*, Opt. Express **21**, 10841 (2013).

J. Svozilík, J. Peřina Jr., and J. P. Torres, *High spatial entanglement via chirped quasi-phase-matched optical parametric down-conversion*, Phys. Rev. A **86**, 052318 (2012).

D. Javůrek, **J. Svozilík**, and J. Peřina Jr., *Generation of photon pairs with nonzero orbital angular in a ring fiber*, submitted to Opt. Express.

J. Svozilík, R. de Jesus Leon-Montiel, and J. P. Torres, *Implementation of a spatial two-dimensional quantum random walk with tunable decoherence*, Phys. Rev. A **86**, 052327 (2012).

J. Svozilík, J. Peřina Jr. , and J. P. Torres, *Measurement-based tailoring of anderson localization of partially coherent light*, Phys. Rev. A **89**, 053808 (2014).

A list with all of author's publications can be found in page 95.

Contents

Chapter 1

What is entanglement?

1.1 Entanglement vs Correlations

1.1.1 Origin of Entanglement

The beginning of quantum theory is usually traced back to the quantization used by Max Planck in 1900 to explain the features of blackbody radiation [1]. The theory was put into solid physical ground in the decade of 1920s by the works of Heisenberg, Schrödinger, Born and others, who gave birth to Quantum Mechanics, arguably one of the most important and successful physical theories that mankind has ever developed.

Einstein, Podolsky and Rosen published in 1935 a paper [2] that described a *Gedanken experiment* concerning correlations between quantum particles. They considered a couple of particles that have been allowed to interact in the past, and as a consequence, show certain correlations in position and momentum between them. Performing measurements of the position of first particle and of the momentum of the second particle, one could, according to their considerations, obtains a completed description of the quantum state of both particles. That would lead to a contradiction with the Heisenberg Uncertainty principle.

In the same year 1935, E. Schrödinger introduced the concept of entanglement [3] to describe the correlations of the two particles considered in the EPR paper:

> When two systems, of which we know the states by their respective representatives, enter into temporary physical interaction due to known forces between them, and when after a time of mutual influence the systems separate again, then they can no longer be described in the same way as before, viz. by endowing each of them with a representative of its own. I would not call that *one*

> but rather *the* characteristic trait of quantum mechanics, the one that enforces its entire departure from classical lines of thought. By the interaction the two representatives (or Ψ-functions) have become entangled.

The strange behaviour of entangled quantum states is essentially an inherent feature of Quantum Mechanics. Entanglement is thus one of the main traits of quantum theory, for some it is even *the weirdest feature of quantum mechanics* [4].

Discussions about the existence of entanglement between spatially distant particles have however continued, especially about the possible existence of a more basic and fundamental *local hidden-variables* theory that could explained all of the weird features of entanglement. The most important contribution to resolve this discussion was made by John Bell in 1964 [5], fifty years ago now. He showed that any theory of local hidden parameters should impose certain constraints (in the form of an inequality) on the possible results obtained in measurements performed on the two-particle system. Surprisingly, non-classically correlated (entangled) quantum states can violate these constraints. Shortly after Bell's paper, in 1969 Clauser, Horne, Shimony simplified the original Bell's inequality making it more experimentally suitable [6]. The CHSC inequality is nowadays used as one, among many others, basic test of the presence of entanglement due to its straightforward experimental attainability (for more details see the Subsection 2.4.3).

1.1.2 Definition of Bipartite Entangled States

We now proceed to a formal mathematical definition of entangled bipartite states, which are of prime interest in this thesis. Let us assume that the full Hilbert space of interest is of the form $\mathcal{H}_{12} = \mathcal{H}_1 \otimes \mathcal{H}_2$, where $\mathcal{H}_1$ and $\mathcal{H}_2$ are Hilbert subspaces. A pure state $|\psi\rangle_{12}$ is *separable*(non-entangled) if it can be expressed as

$$|\psi\rangle_{12} = |\psi\rangle_1 \otimes |\psi\rangle_2, \tag{1.1}$$

where $|\psi\rangle_1 \in \mathcal{H}_1$ and $|\psi\rangle_2 \in \mathcal{H}_2$. Otherwise is *entangled*. A mixed state $\hat{\rho}_{12} \in \mathcal{H}_{12}$ is separable if it can be written as a convex sum

$$\hat{\rho}_{12} = \sum_i p_i \hat{\rho}_{i,1} \otimes \hat{\rho}_{i,2}, \tag{1.2}$$

where $p_i > 0$ are probabilities, $\hat{\rho}_{i,1} \in \mathcal{H}_1$ and $\hat{\rho}_{i,2} \in \mathcal{H}_2$.

In many circumstances, the knowledge of the amount of entanglement, *how much* are quantum states non-classically correlated, is of paramount importance [7, 8]. The Bell's

inequality can be used as an indicator of the presence entanglement, but the degree of violation of the inequality cannot be used as a good measure of entanglement. For a pure state $\hat{\rho}_{12} \in \mathcal{H}_{12}$, where $Tr\left(\hat{\rho}_{12}^2\right)$=1, the amount of entanglement is usually characterized via the *Von Neumann entropy E*

$$E = -Tr\left(\hat{\rho}_1 \ln \hat{\rho}_1\right) = -Tr\left(\hat{\rho}_2 \ln \hat{\rho}_2\right). \tag{1.3}$$

where $\hat{\rho}_1$ ($\hat{\rho}_2$) is the density matrix that describes the quantum state of subsystem 1 (2). For a separable state E is equal to zero. The entanglement can also be quantified by the *Von Neumann mutual information I*

$$I\left(\hat{\rho}_1, \hat{\rho}_2, \hat{\rho}_{12}\right) = E\left(\hat{\rho}_1\right) + E\left(\hat{\rho}_2\right) - E\left(\hat{\rho}_{12}\right). \tag{1.4}$$

Alternatively, as an entanglement measure one can employ the *relative entropy S* defined as

$$S\left(\hat{\rho}_{12} \parallel \hat{\sigma}_{12}\right) = Tr\left(\hat{\rho}_{12} \log \hat{\rho}_{12} - \hat{\rho}_{12} \log \hat{\sigma}_{12}\right), \tag{1.5}$$

where $\hat{\sigma}_{12} \in \mathcal{H}_{12}$ is the closest separable state to $\hat{\rho}_{12}$.

The separability of quantum states can be also quantified by means of the *Schmidt number K* [9]. This number reflects the amount of effectively excited modes that constitute the whole state $|\psi\rangle_{12}$. This measure is based on the use of the Schmidt decomposition [10] applied on the quantum state $|\psi\rangle_{12}$. For the sake of example, let us consider that the Hilbert space $\mathcal{H}$ is the two-dimensional continuous space containing the state

$$|\Psi\rangle_{12} = \int dx \int dy \mathcal{A}\left(x, y\right) |x\rangle_1 |y\rangle_2, \tag{1.6}$$

where $|x\rangle_1 \in \mathcal{H}_1$ and $|y\rangle_2 \in \mathcal{H}_2$. The function $\mathcal{A}$ is the two-photon amplitude satisfying the normalization condition $\int dx \int dy |\mathcal{A}(x,y)|^2 = 1$. Applying the Schmidt decomposition on this function, we can express $\mathcal{A}$ as a sum of a set of orthonormal functions $\{f_n\}$ and $\{g_n\}$

$$\mathcal{A}(x,y) = \sum_{n=1}^{\infty} \sqrt{\lambda_n} f_n(x) g_n(y), \tag{1.7}$$

where λ_n are Schmidt coefficients that correspond to each pair of functions f_n and g_n. The Schmidt number K is obtained as:

$$K = \frac{1}{\sum_n \lambda_n^2}. \tag{1.8}$$

In the case that in the decomposition of $\mathcal{A}$ only one mode is present, there is only one non-vanishing coefficient λ_n, the state is separable and $K = 1$. The decomposition also allows to recover the Shannon entropy S [10, 11] from Eq. (1.3)

$$S = -\sum_{n=1}^{\infty} \lambda_n \log_2(\lambda_n). \tag{1.9}$$

1.2 Generation of Entangled States

Various techniques to prepare entangled fields (or particles) have been developed during the last few decades. In order to be used in many different applications, sources of entanglement should satisfy several requirements as a high efficiency, broad tunability and compactness, and the possibility of integration with other optical components. The most common sources of entangled fields are based on the emission of photons. Photons pose several degrees of freedom, such as a position, momentum, frequency, polarization and spatial shape (or orbital angular momentum, OAM) [12, 13] [A1]. Entanglement can be realized in any of above mentioned degrees of freedom or even in a combination among them, which result in the so-called *hyper-entanglement* [14, 15]. The minimal interaction of photons with an environment predetermines them as a perfect carrier of information.

The first entangled photon sources developed in the seventies of the 20th century used transitions between energy levels of Ca atoms, which allow the generation of photons entangled in polarization [16, 17]. Based on a similar principle, but some time later, it has been shown that also quantum dots allow the generation of entangled photons employing the bi-exciton radiative decay [18, 19].

Spontaneous parametric down-conversion (SPDC) is one of the most commonly used nonlinear phenomenon for preparing various types of quantum states of multiphoton systems. This process is mediated by the atoms of a non-centrosymmetric non-linear medium. A pump photon with high frequency is converted to two photons of lower frequency according to the energy and moment conservation laws, i.e., the *phase-matching conditions*. Studies of photon pair generation presented in Chapters 2 and 3 are based on this process. The initial experimental observation of correlated photons based on SPDC in a nonlinear medium was reported in 1970 by Burnham et al. [20]. The experimental preparation of entangled photon pairs in polarization followed [21], being the demonstration of teleportation one of the greatest achievement achieved making use of polarization entangled photons [22]. Due to the low efficiency of the SPDC process, new approaches has generally pursued the generation of increasingly larger flux rates of entangled photons. This was

the case, for instance of the scheme demonstrated by Kwiat et al., who presented the idea of increasing photon flux utilizing two glued anisotropic crystals with mutually crossed optical axes [23]. Besides bulk crystals, waveguides represent a high-efficient alternatives. Namely, due to advance semiconductor technologies, the generation of entangled photons in AlGaAs materials [24,25] [A2–A4] and Silica [26] has been reported. The modal entanglement in waveguides has been presented in [27,28]. We should mention that entangled photon pairs can be also generated employing other nonlinear optics processes, such as four-wave mixing [29,30].

1.3 Applications of Entanglement

Quantum communications protocols use the unique feature of entanglement, which allows to transfer, in principle, higher amounts of information together with a higher security, in comparison to classical communication channels. Super-dense coding represents a way to enhance channel throughput by using only one bit of quantum information to transfer 2 bits of classical information [31]. Quantum teleportation works on a similar principle [22,32]. Here the initially unknown state of a particle is transferred, using an entangled pair, to a far away receiving station. Even quantum cryptography benefits from the use of entangled photons [33].

Many *quantum computing algorithms* are based on entanglement [8]. D. Deutsch has shown that quantum entanglement allows to speed up a certain group of computing tasks when compared to the same tasks being processed on classical computers [34]. For instance, Deutsch's algorithm allows to determine, with a lower number of measurements, if an unknown function is whether constant for all input cases or not. In a classical procedure, one has to try all possible combinations of input variables to accomplish this task. Employing an entangled state, this task can be done in a single step. The famous Shore's algorithm for factorization of large integer numbers [35] and Grover's searching algorithm [36] are also based on the use of entangled states.

Another area of research where entanglement has pivotal consequences *quantum metrology* [37]. For instance, Ramsey spectroscopy of n-ions exhibits an increase of precision when measuring the frequency of atomic transitions by a factor $\sqrt{n}$ [38]. Probing of biological tissue using quantum optical coherence tomography makes use of entangled photon pairs, showing an increase of the axial resolution of interferometry and some immunity to the presence of certain harmful dispersive effects [39].

Regardless of the high amount of still open questions, there is an on-going discussion regarding the possible role that entanglement can play in the so-called *quantum biology*

[40, 41]. Some evidences have been reported for the harvesting complexes of green plants. There, entanglement seems to play a role accelerating the speed of transfer of excitons [42]. Another system where the role of entanglement in under current discussion is the magnetic navigation compass of sea birds, located in their eyes [43]. The interaction of the planetary magnetic field with an entangled pair of radicals results in certain chemical reactions that might indicate to the bird's brain its orientation with respect to this field.

Chapter 2

Generation of entanglement in semiconductor Bragg Reflection Waveguides

2.1 Introduction

In nonlinear optics, waveguides are a very convenient tool for enhancing the efficiency of nonlinear conversion interactions. By confining electromagnetic field to a small transverse area, one can increase the efficiency of a nonlinear interaction by several orders of magnitude in a comparison to bulk crystals, as shown, for instance, in [44, A13]. In SPDC in bulk crystals, photons are emitted into a large continuum spatial modes, consequently the use of waveguides provides us a way of reducing the number of spatial modes wherein photons are generated. In a typical waveguide, only a few number of discrete guided modes are supported [45]. Thus the overall efficiency of nonlinear interactions is dramatically boosted [44]. Moreover, waveguide structures offer a broad tunability to tailor the characteristics of quantum states, the spatial shape and frequency content of the down-converted photons generated. Compactness makes possible to use the photon source under a greater variety of circumstances, such as, for instance, would be the case of free space applications [46].

A fundamental challenge in the design of waveguide structures is to ensure the perfect phase-matching (PM) of all interacting fields. Several methods have been developed to overcome the natural phase-mismatch caused by a material dispersion. The easiest way for birefringent materials is to use differences in the index of refraction for different polarization of fields. The collinear regime of propagation in waveguides precludes to achieve

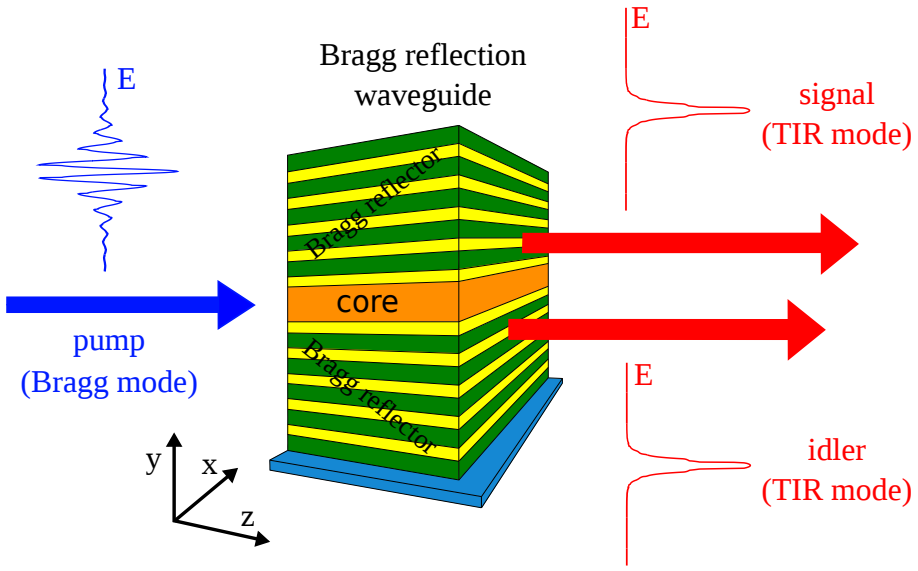

Figure 2.1: Illustration of a Bragg reflection waveguide, showing also the basic guided modes involved in the SPDC process, whose profiles are presented in 1D cuts along the y-axis.

the phase-matching via the non-collinear regime typical for bulk crystals. However, since guided spatial modes exhibit distinct propagation constants, modal phase-matching can be accomplished between different types of modes [47–50]. Alternatively, PM can be achieved by an additional structural modification which introduces a periodic modulation of the non-linear susceptibility $\chi^{(2)}$ [51]. The periodic poling [52] is a standard fabrication technique now. This modulation can be achieved in ferroelectric crystals, such as $LiNbO_3$, SLT and KTP materials. The basic principle is the application of a high voltage static field that cases a permanent reorientation of ferroelectric domains in a crystal, generating a corresponding periodic alternation of the sign of $\chi^{(2)}$. The advantage of this method is a wide tunability of phase-matching conditions between different degrees of freedom.

Semiconductor Bragg reflection waveguides (BRWs) make use of the previously mentioned modal-phase-matching in non-linear materials, since they lack birefringence [50]. This kind of waveguides is usually composed of two Bragg mirrors placed around the core (see Fig.2.1), allowing light to be trapped in the transverse direction. BRWs support generally two basic types of guided modes. The first one, the Bragg mode, is guided by distributed reflections in the mirrors and the second one is the total-internal-reflection (TIR) mode. Methods of solving the Helmholtz equation for BRWs are described in the Appendix A. If the pump beam propagates as the Bragg mode and down-converted pho-

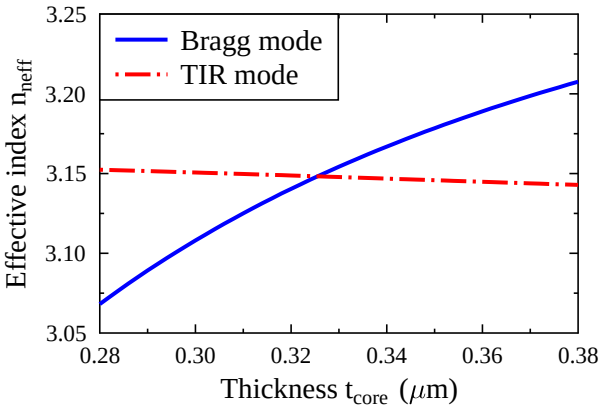

Figure 2.2: Effective indices of Bragg (at 775 nm) and TIR modes (at 1550 nm) as a function of the core of the waveguide thickness. This represents one of many ways how to reach PM. Structural parameters of the representative waveguide were taken from [50] and guided modes were found using the FEM method A.2. As it is easily noticed, the Bragg mode exhibits strong modal dispersion in comparison to TIR modes, which are less dispersive regardless of wavelength.

tons as TIR modes, the phase-matching between them can be achieved by the proper design of the structure. This is the principle of modal phase-matching in BRWs as depicted in Fig.2.2. As shown, the Bragg mode exhibits a strong modal dispersion on the contrary to the fundamental TIR mode, which is less dispersive [53, 54]. Additionally, the strong modal dispersion in BRWs offers significant control over the spectral width [55] and the type of spectral correlations of the emitted photons (see the next section). Recently, the possibility of generation of hyper-entangled fields in BRWs has been considered [15].

BRWs based on the III-V ternary semiconductor materials, such as $Al_xGa_{1-x}As$ and $Al_xGa_{1-x}N$, benefit from mature fabrication technologies that offers many possibilities of integration of all optical elements in a single semiconductor platform. Even more, since typical operation wavelengths lie close to the material bang gap, they exhibit extraordinary large non-linear coefficients ($d_{\text{eff}}^{\text{GaAs}} \sim 119$ pm/V [56] and $d_{\text{eff}}^{\text{GaN}} \sim 3$ pm/V [57, 58]). Other important properties are broad transparency windows, large damage thresholds and low linear propagation losses.

In the last few years, different non-linear processes have been experimentally observed in $Al_xGa_{1-x}As$ BRWs, such as second-harmonic generation [50, 59], difference-frequency generation [60] and SPDC [25]. Furthermore , BRWs have been demonstrated as edge-emitting diode lasers where the fundamental lasing mode is the photonic band-gap mode or the Bragg mode [61]. Electrically pumped parametric fluorescence employing BRWs

has been demonstrated subsequently [62].

In the following sections, we present two applications of BRWs. Firstly, in Section 2.2, we introduce a novel approach for the generation of separable quantum state using BRWs based on the AlGaN semiconductor. The separability in the frequency domain is shown for two different scenarios of spectral properties of photon pairs, which are reached by a proper engineering of modal dispersion. In the next Section 2.3, BRWs are proposed as part of a scheme aimed at developing an integrated source of polarization-entangled photon pairs highly suitable for its use in a multi-user quantum-key-distribution system. Finally, in Section 2.4, an experimental realization of SPDC in BRW is presented. In the experiment, entangled photon pairs in the polarization degree of freedom are generated at the telecommunication wavelength. The non-classicality of such generated photon pairs is confirmed by the violation of the Clauser-Horne-Shimony-Holt Bell-like inequality.

2.2 BRW as a Source of Uncorrelated Photon Pairs

In most applications the goal of using SPDC is the generation of entangled photon pairs. However, the generation of photon pairs that lack any entanglement (quantum separability), but are generated in the same time window, is also of paramount importance for quantum networking and quantum information processing [63–65]. By and large, separable photon pairs are not harvested directly at the output of the down-converting crystal [66] and their generation in a separable quantum state requires intricate control of the properties of the down-converted photons in all the degrees of freedom. Although one can always resort to strong spectral filtering to enhance the quantum separability of the two-photon state [67], this entails a substantial reduction in the brightness of the photon source. Alternatively, for example, elimination of the frequency correlation of photon pairs can be achieved when the operating wavelength, the nonlinear material and its length are appropriately chosen [68], as has been demonstrated in [69]. The use of achromatic phase matching, or tilted-pulse techniques, allows the generation of separable two-photon states independently of the specific properties of the nonlinear medium and the wavelength used [70–72]. Non-collinear SPDC also allows the control of the generation of frequency-uncorrelated photons by controlling the pump-beam width and the angle of emission of the down-converted photons [73, 74]. It is indeed possible to map the spatial characteristics of the pump beam into the spectra of the generated photons (spatial-to-spectral mapping) [75], thus providing another way to manipulate the joint spectral amplitude of the biphoton, as has been demonstrated in [76]. The combination of using the pulse-tilt techniques described above together with using non-collinear geometries further expands

the possibilities to control the joint spectrum of photon pairs [77]. Another approach to control the frequency correlations is to use nonlinear crystal superlattices [78].

The methods mentioned above are based on tuning the dispersive properties of the nonlinear medium by steering the propagation of light in a bulk crystal. However, as it has already been mentioned, waveguides do not allow this, so the quantum separability has to be achieved via another approach. In this section, we demonstrate that BRWs made of N slabs of Al_x Ga_{1-x} can be tailored to generate photon pairs in a quantum separable state. For obtaining separability in the frequency domain, the signal photon has to propagate as a Bragg mode and pump beam as a TIR mode. Since PM cannot be achieved in the usual way (by appropriate design of the BRW layers), quasi-phase-matching (QPM) of the core slab is used to satisfy the phase-matching condition, while the tailoring of the dispersive properties of the waveguide allows us to control the frequency correlations between the down-converted photons.

2.2.1 Quantum State of Uncorrelated Photon Pairs

The quantum state of the down-converted photons (the signal and idler) at the output face of the waveguide, while neglecting the vacuum contribution, can be written as

$$|\Psi\rangle = \int d\Omega_s d\Omega_i \Phi(\Omega_s, \Omega_i) \hat{a}_s^\dagger(\omega_s^0 + \Omega_s) \hat{a}_i^\dagger(\omega_i^0 + \Omega_i) |0\rangle_s |0\rangle_i, \tag{2.1}$$

where $\hat{a}_s^\dagger(\omega_s + \Omega_s)$ and $\hat{a}_i^\dagger(\omega_i + \Omega_i)$ designate the creation operators of signal and idler photons at frequencies $\omega_s^0 + \Omega_s$ and $\omega_i^0 + \Omega_i$, respectively. $\omega_s^0 = \omega_i^0$ are the central frequencies of the signal and idler photons, and $\Omega_{s,i}$ designate the frequency deviations from the corresponding central frequencies. The signal and idler photons are generated in specific spatial modes of the waveguide as will be described later.

The biphoton amplitude $\Phi(\omega_s, \omega_i)$ is given by

$$\Phi(\Omega_s, \Omega_i) = \mathcal{N} E_p(\omega_p^0 + \Omega_p) \mathrm{sinc}\left(\frac{\Delta_k L}{2}\right) \exp\left(i \frac{s_k L}{2}\right), \tag{2.2}$$

where $\Delta_k = k_p - k_s - k_i$ and $s_k = k_p + k_s + k_i$. $k_{p,s,i}$ are the longitudinal (z) components of the wavevector of all the interacting photons. E_p is the spectral amplitude of the pump beam at the input face of the waveguide, which is assumed to be Gaussian, with central frequency $\omega_p^0 = \omega_s^0 + \omega_i^0$. As such, $E_p(\Omega_p) \sim \exp\left(-\Omega_p^2/\Delta\omega_p^2\right)$, where $\Omega_p = \Omega_s + \Omega_i$. $\mathcal{N}$ is a normalizing constant, which ensures that $\int\int d\Omega_s d\Omega_i |\Phi(\Omega_s, \Omega_i)|^2 = 1$.

The spatial modes of the pump, signal and idler photons that we will considered here

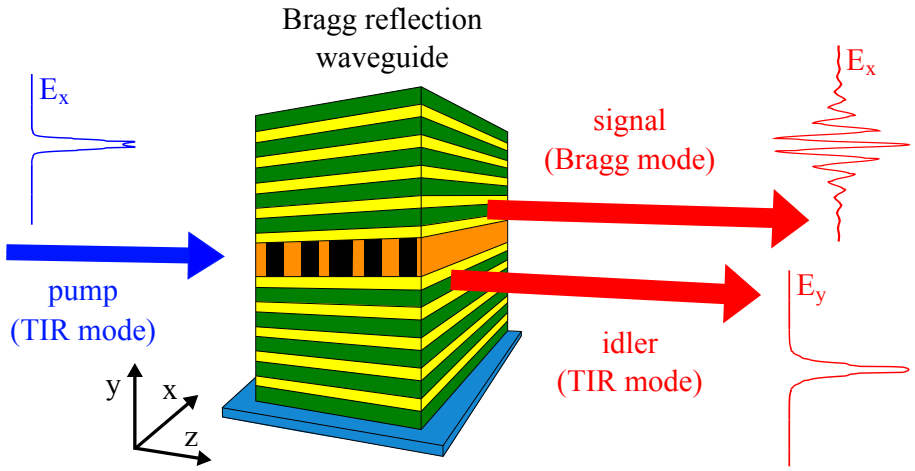

Figure 2.3: General scheme for generating frequency-uncorrelated photon pairs. The waveguide is pumped by a TIR mode with TE polarization. The down-converted photons with TE polarization propagate in a Bragg mode, while the down-converted photons with TM polarization propagate in a TIR mode. The two structures presented here make use of the same combination of modes and the spatial shapes of the modes are almost identical for both structures. The Bragg and TIR modes have different group velocities that can be properly engineered by modifying the waveguide structure.

are shown schematically in Fig. 2.3. The pump and idler photons propagate as TIR modes. The signal photons propagate as Bragg modes. The use of different spatial modes for the signal and idler enhances the control of the dispersive properties of the SPDC process.

In order to get further insight into the procedure to search for BRW configurations that generate separable paired photons, we expand the longitudinal wavevectors to first order, so that $k_j = k_j^0 + N_j\Omega_j$ with $j = p, s, i$. $k_j^{(0)}$ are the longitudinal wavevectors at the central frequencies ω_j^0, and N_j are the inverse group velocities. Under these conditions, the biphoton amplitude can be written as

$$\Phi(\Omega_s, \Omega_i) = \mathcal{N} \exp\left\{-\frac{(\Omega_s + \Omega_i)^2}{\Delta w_p^2}\right\} \operatorname{sinc}\left\{\left[(N_p - N_s)\,\Omega_s + (N_p - N_i)\,\Omega_i\right]\frac{L}{2}\right\}$$
$$\times \exp\left\{i\left[(N_p + N_s)\Omega_s + (N_p + N_i)\Omega_i\right]\frac{L}{2}\right\}. \tag{2.3}$$

Upon inspecting of Eq.(2.3), one can show that if the inverse group velocities of the signal

(idler) and pump are equal $N_p = N_s$ ($N_p = N_i$), increasing the bandwidth of the pump beam bandwidth such that $\Delta\omega_p \gg 1/|N_p - N_{s,i}|L$ allows us to erase all the frequency correlations between the signal and idler photons. Notice that in this case, even though there is no entanglement between the signal and idler photons, the bandwidth of one the photons is larger than the bandwidth of the other photon. The quantum state is separable but the photons are distinguishable by their spectra.

To generate uncorrelated and indistinguishable photon pairs, the condition $N_p = (N_s + N_i)/2$ should be fulfilled together with the condition for the bandwidth

$$\Delta\omega_p \simeq \frac{2}{\alpha L\sqrt{N_s - N_p}\sqrt{N_p - N_i}}. \tag{2.4}$$

This condition is obtained from approximating the sine cardinal function sinc(x) in Eq. (2.3) by a Gaussian function $\exp\left[-(\alpha \mathrm{x})^2\right]$ with $\alpha = 0.439$.

To quantify the degree of entanglement of the generated two-photon state, we calculate the Schmidt decomposition of the biphoton amplitude (introduced on page 2) , i.e., $\Phi(\Omega_s, \Omega_i) = \sum_{n=0}^{\infty} \sqrt{\lambda_n} U_n(\Omega_s) V_n(\Omega_i)$, where λ_n are the Schmidt eigenvalues and U_n and V_n are the corresponding Schmidt modes. The degree of entanglement of the two-photon state is then quantified by means of the Schmidt number K defined by Eq. (1.8) and the entropy E given by Eq. (1.9).

2.2.2 Design of BRW Structures to Generate Uncorrelated Photon pairs

Let us consider the generation of paired photons in the C-band of the optical communication window, i.e., let the central wavelength of both emitted photons be 1550 nm. Therefore, for the frequency-degenerate case, the central wavelength of the pump beam must be 775 nm. The main parameters that characterize the dispersion properties of the Bragg modes, and that can be engineered to tailor the spectral properties of the down-converted photons, are the thickness of the layers and their aluminium fraction.

BRW structures for the generation of frequency-uncorrelated photon pairs were obtained by numerically solving the Maxwell equations inside the waveguide using the finite element method described in the Appendix A.2 for the 1D case. Since many solutions were found, a genetic algorithm was used to select waveguides with the properties that are most suitable for practical implementation. The thicknesses and the corresponding aluminium fractions of two of the structures obtained are given in Table 2.1.

The refractive indices for the calculations were taken from [79]. The Bragg reflection waveguides are composed of 12 bi-layers above and below the core. Both structures were

Table 2.1: (a) Parameters of the waveguide structure: t_c - core thickness; $t_{1,2}$ - thicknesses of the alternating layers of the Bragg reflector; x_c - aluminium concentration in the core; $x_{1,2}$ - aluminium concentration in the reflector's layers; Λ - quasi-phase-matching period. Both structures are 4 mm long and they are optimized for type-II SPDC. (b) Profile of the refractive index along the y-axis of the Bragg reflection waveguide.

(a)

Parameter	Structure 1	Structure 2
$t_c(nm)$	1037	986
$t_1(nm)$	463	430
$t_2(nm)$	810	533
$x_c(\%)$	57	56
$x_1(\%)$	44	39
$x_2(\%)$	88	65
$\Lambda(\mu m)$	10.4	7.4

(b)

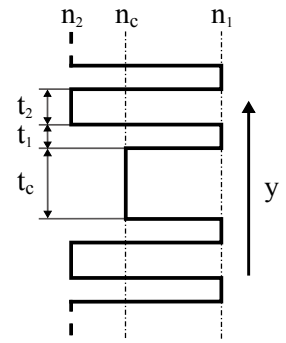

optimized for the Bragg mode propagation at the quarter-wave condition for the central wavelength, which maximizes the energy confinement in the core. The spatial shapes of the modes (pump, signal and idler) that propagate in Structure 1 are shown in Fig.2.3. The spatial modes corresponding to Structure 2 are almost identical and therefore are not shown.

Type-II SPDC interactions are considered for both structures, even though structures with type-I or type-0 interactions can also be designed. One of the advantages of type-II phase-matching is that the generated photons can easily be separated at the output of the waveguide by its different polarization. The pump and signal photons have TE polarization and the idler photons have TM polarization. The signal photon propagates as a Bragg mode, whereas the idler photon propagates as a TIR mode. The quasi-phase-matching can be achieved, for example, by the method described in [80]. The quasi-phase-matching periods Λ were calculated from the phase-matching condition $\Delta_k - 2\pi/\Lambda = 0$, where the phase-mismatch function Δ_k is taken at the central frequencies of all the interacting waves.

The spatial overlap between the modes of the interacting photons is defined as

$$\Gamma = \int dx\, u_p(x) u_s^*(x) u_i^*(x), \tag{2.5}$$

where $u_j(x)$, $j = p, s, i$ are the mode functions describing the transverse distribution of the electric field in the waveguide. The overlap reaches 40.5% for Structure 1 and 19.4% for Structure 2. The combination of the high effective nonlinear coefficient and the overlap

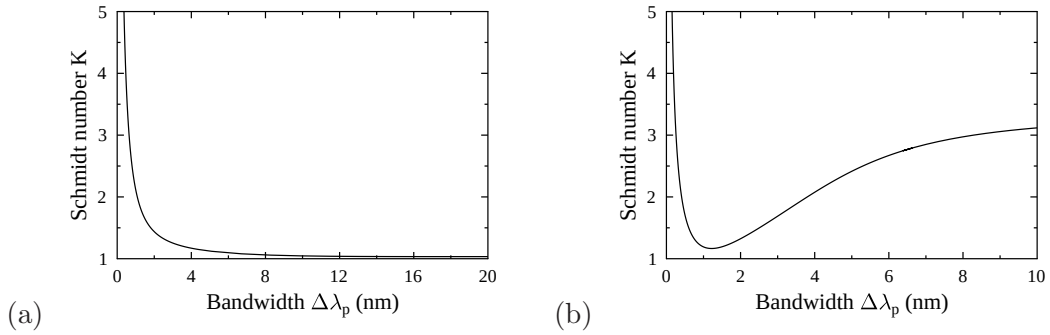

Figure 2.4: The Schmidt number K as a function of the bandwidth of the pump beam $\Delta\lambda_p$ for (a) Structure 1 and (b) Structure 2.

results in an efficiency that is still much higher than with other phase-matching platforms in waveguides or in bulk media. Although the thickness of the core of both structures is sufficiently large so that higher-order modes (both TIR and Bragg modes) could exist, they lack phase-matching and their overlap is very small.

Uncorrelated photon pairs with different spectra

Structure 1 provides a configuration to generate a quantum separable state with different spectral bandwidths for the signal and idler photons. The group velocities of the pump and signal photons are equal. We find that $\mathrm{v}_p = \mathrm{v}_s = 0.445c$, where c is the speed of light in vacuum. The dependency of the Schmidt number K on the pump beam bandwidth is plotted in Fig.2.4(a). A highly separable quantum state can be obtained for a pump beam bandwidth $\Delta\lambda_p \geq 10$ nm. For values of $\Delta\lambda_p < 1$ nm, the paired photons turn out to be

!

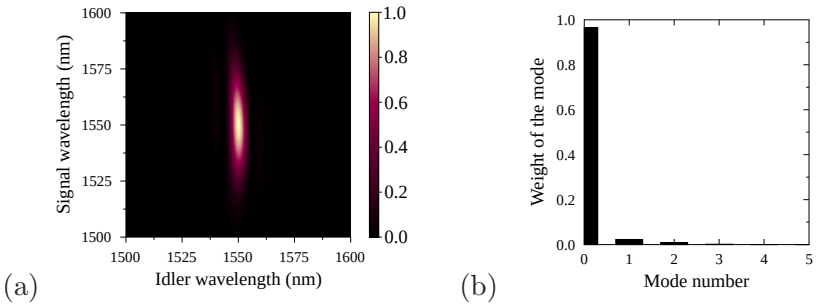

Figure 2.5: (a) Joint spectral intensity of the biphoton generated in Structure 1 for $\Delta\lambda_p$=10 nm. (b) The Schmidt decomposition corresponding to this quantum state.

anti-correlated.

The joint spectral intensity of the biphoton is showed in Fig.2.5(a). It shows a cigar-like shape oriented along the signal wavelength axis, as expected from the fulfillment of the condition $N_p = N_s$. The Schmidt decomposition is shown in Fig. 2.5(b). Clearly, this decomposition corresponds to a nearly ideal case of frequency-uncorrelated photons. For the case shown in Fig. 2.5, with a pump beam bandwidth (FWHM) of 10 nm, the bandwidths of the signal and idler photons are 47.5 nm and 8 nm, respectively. The entropy of entanglement is used as a measure of spectral correlation [8] and is defined by Eq.1.9. The obtained value is 0.257 in this case.

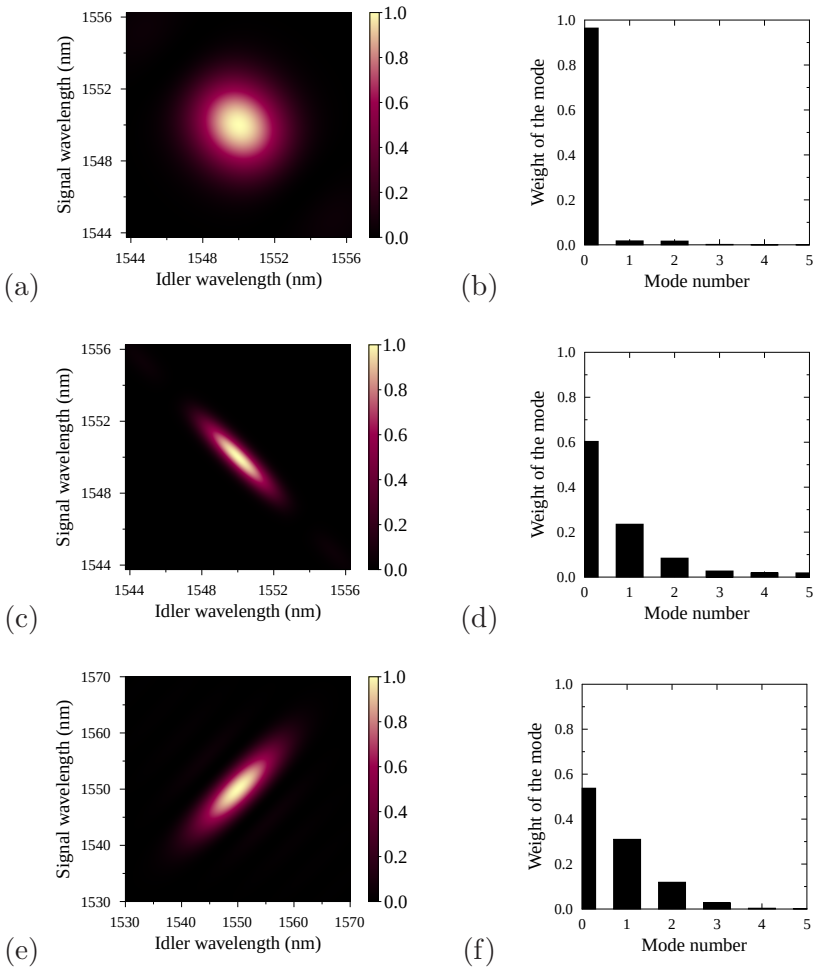

Figure 2.6: Joint spectral intensity of photons generated in Structure 2 for different pump bandwidths: (a) $\Delta\lambda_p = 1.3$ nm, (c) $\Delta\lambda_p = 0.3$ nm and (e) $\Delta\lambda_p = 4.8$ nm. Plots (b), (d) and (f) in the second column are the corresponding Schmidt decompositions.

Uncorrelated photon pairs with identical spectra

Structure 2 is designed for the generation of a separable two-photon state where both photons exhibit the same spectra. The calculated values of the group velocities of all the waves are $v_p = 0.441c$, $v_s = 0.425c$ and $v_i = 0.456c$. Figure 2.4(b) shows the value of the Schmidt number K as a function of the pump beam bandwidth. The optimum pump bandwidth for the generation of frequency-uncorrelated photons is found to be $\Delta\lambda_p = 1.3$ nm, for which K achieves its lowest value. The value of K cannot reach the ideal value of 1 due to the presence of the side-lobes of the sinc function in the anti-diagonal direction and a Gaussian profile in the diagonal direction that introduces a slight asymmetry (see Eq.(2.3)). Figure 2.6(a) shows the joint spectral intensity of frequency-uncorrelated photons, when this optimum value of the pump bandwidth is used. Figure 2.6(b) shows the corresponding Schmidt decomposition. The entropy of entanglement is 0.267 and the bandwidth is 4.5 nm for both signal and idler photons.

For smaller values of the pump beam bandwidth, the photons generated in Structure 2 correspond to photon pairs that are anticorrelated in frequency (see Fig. 2.6(c)), whereas the use of larger values allows the generation of frequency-correlated photon pairs (see Fig. 2.6(e)). Figures 2.6(d) and (f) show the Schmidt decompositions corresponding to each of these cases.

2.3 BRW as a Source of Polarization-Entangled Photon Pairs

One application that is attracting recently a lot of interest due its potential key role in future quantum communication networks is multi-user quantum key distribution (QKD) [81]. In order to implement a multi-user QKD network, one needs various frequency channels that can expediently be employed for transmitting individual entangled pairs. In this way, one can re-route on demand specific channels between users located in different sites of the optical network. Similar schemes, considering the emission of photon pairs in different spectral and spatial modes, have been presented in [82, 83] for an on-demand single-photon source based on a single crystal.

To prepare polarization-entangled paired photons in many frequency channels at the same time, one needs to engineer an SPDC process with an ultra-broad spectrum. Usually type-I or type-0 configurations are preferred. With the type-II phase-matching, the two down-converted photons have different polarizations and consequently different group velocities, which reduces dramatically their bandwidth. For instance, the FWHM bandwidth of an SPDC process in a type-II periodically-poled (PP) KTP crystal at 810 nm

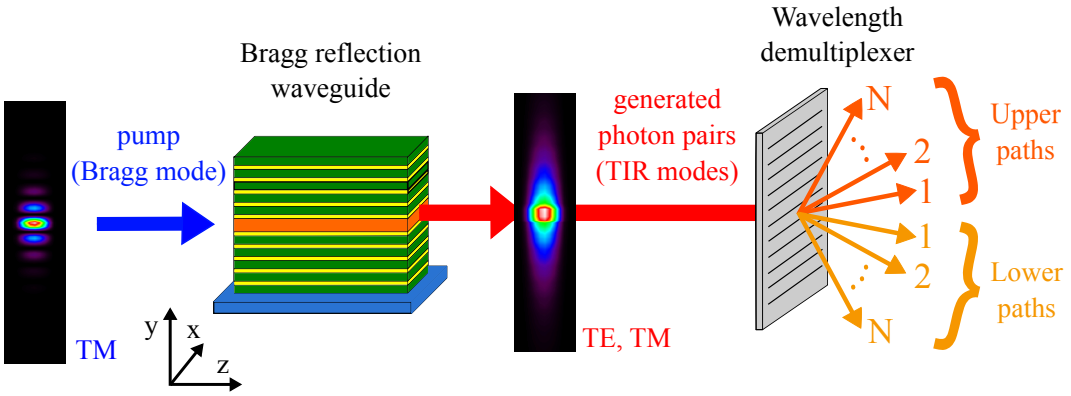

Figure 2.7: General scheme for the generation of polarization-entangled photon pairs in various frequency channels by making use of the Bragg reflection waveguide. In this scheme, a dichroic mirror or a grating can be used as the wavelength demultiplexer.

is $\Delta\lambda(\text{nm}) = 5.52/\text{L(mm)}$, where L is the length of the crystal [84]. For $L = 1$ mm, the bandwidth is $\Delta\lambda \sim 5.5$ nm. On the other hand, in a type-0 PPLN configuration with the same crystal length $L = 1$ mm, Lim et al. [85] achieved an approximate tenfold increase of the bandwidth $\Delta\lambda \sim 50$ nm. Even though one can always reduce the length of the nonlinear crystal in a type-II configuration to achieve an increase of the bandwidth, this results in a reduction of the spectral brightness of the source.

Alternatively to short bulk crystals, Bragg reflection waveguides (BRWs) based on III-V ternary semiconductor alloys ($Al_xGa_{1-x}As$) offer the possibility to generate polarization-entangled photons with an ultra-large bandwidth, as is shown in this section. The most striking feature of the use of BRW as a photon source is the capability of controlling the dispersive properties of all interacting waves in the SPDC process, which in turn allows the tailoring of the bandwidth of the down-converted photons: from narrowband ($1 - 2$ nm) to ultra-broadband (hundreds of nm) [55, 86, 87], considering both type-I and type-II configurations. Therefore, one can design a type-II SPDC process in BRWs with a bandwidth typical for type-I or type-0 processes.

2.3.1 Quantum State of Entangled Photon Pairs

In order to investigate the potential of the proposed design for generating wavelength-multiplexed polarization-entangled photon pairs over many frequency channels, let us examine biphoton generation in a collinear type-II phase-matching scheme in the Bragg reflection waveguide (see Fig. 2.7). A continuous-wave TM-polarized pump beam with

frequency ω_p illuminates the waveguide and mediates the generation of a pair of photons with mutually orthogonal polarizations (signal: TE polarization; idler: TM polarization). The frequencies of the signal and idler photons are $\omega_s = \omega_0 + \Omega$ and $\omega_i = \omega_0 - \Omega$, respectively, where ω_0 is the degenerate central angular frequency of both photons, and Ω is the angular frequency deviation from the central frequency. The signal photon (TE) propagates as a TIR mode of the waveguide with spatial shape $U_s(x, y, \omega_s)$ and propagation constant $\beta_s(\omega_s)$. The idler photon (TM), also a TIR mode, has a spatial shape $U_i(x, y, \omega_i)$ and propagation constant $\beta_i(\omega_i)$. The pump beam is a Bragg mode of the waveguide with spatial shape $U_p(x, y, \omega_p)$ and propagation constant $\beta_p(\omega_i)$.

At the output face of the nonlinear waveguide, the quantum state of the biphoton can be written as [88]

$$|\Psi_1\rangle = |\text{vac}\rangle_s|\text{vac}\rangle_i + \sigma L F_p^{1/2} \int d\Omega \Phi(\Omega) |\text{TE}, \omega_0 + \Omega\rangle_s |\text{TM}, \omega_0 - \Omega\rangle_i, \tag{2.6}$$

where the nonlinear coefficient σ is

$$\sigma = \left[\frac{\hbar \omega_0^2 \omega_p \left[\chi^{(2)}\right]^2 \Gamma^2}{16\pi\epsilon_0 c^3 \, n_s(\omega_0) n_i(\omega_0) n_p(\omega_p)} \right]^{1/2}. \tag{2.7}$$

F_p is the flux rate of pump photons, $\Gamma = \int d\mathbf{r}_\perp U_p(\mathbf{r}_\perp) U_s^*(\mathbf{r}_\perp) U_i^*(\mathbf{r}_\perp)$ is the overlap integral of the spatial modes of all interacting waves in the transverse plane, and $n_{p,s,i}$ are their refractive indices. The joint spectral amplitude $\Phi(\Omega)$ has the form

$$\Phi(\Omega) = \text{sinc}\left[\Delta_k(\Omega) L/2\right] \exp\left\{i s_k(\Omega) L/2\right\}. \tag{2.8}$$

The ket $|\text{TE}, \omega_0 + \Omega\rangle_s$ ($|\text{TM}, \omega_0 - \Omega\rangle_i$) designates a signal (idler) photon that propagates with polarization TE (TM) in a mode of the waveguide with the spatial shape U_s (U_i) and frequency $\omega_0 + \Omega$ ($\omega_0 - \Omega$). The phase-mismatch function reads $\Delta_k(\Omega) = \beta_p - \beta_s(\Omega) - \beta_i(-\Omega)$, and $s_k(\Omega) = \beta_p + \beta_s(\Omega) + \beta_i(-\Omega)$. The function $|\Phi(\Omega)|^2$ is proportional to the probability of detection of a photon with polarization TE and frequency $\omega_0 + \Omega$ in coincidence with a photon with TM polarization and frequency $\omega_0 - \Omega$.

After the waveguide, a wavelength demultiplexer is used to separate all n frequency channels into coupled fibers leading to the users of the network. The bandwidth of each channel is $\Delta\omega$ and their central frequencies are $\omega_{U,L}^n = \omega_0 \pm n\Delta$, where Δ is the inter-channel frequency spacing and the letter U(L) indicates the upper (lower) path (see Fig. 2.7). After the demultiplexer, the quantum state of the down-converted photons can

be written as

$$
\begin{aligned}
&|\Psi_2\rangle = |\mathrm{vac}\rangle_s|\mathrm{vac}\rangle_i \\
&+1/\sqrt{2}\ \sigma L F_p^{1/2} \int_{B_n} d\Omega \left\{\Phi\left(\Omega\right)|\mathrm{TE},\omega_0+\Omega\rangle_U|\mathrm{TM},\omega_0-\Omega\rangle_L\right. \\
&\left.+\Phi\left(-\Omega\right)|\mathrm{TM},\omega_0+\Omega\rangle_U|\mathrm{TE},\omega_0-\Omega\rangle_L\right\},
\end{aligned}
\tag{2.9}
$$

where $\int_{B_n}$ designates the frequency bandwidth from $\omega_{U,L}^n - \Delta\omega/2$ to $\omega_{U,L}^n + \Delta\omega/2$ coupled into every single fiber. Since we are interested in generating polarization-entangled paired photons coupled into single-mode fibers, the signal and idler photons in the upper and lower paths are projected into the fundamental mode (U_0) of the fiber. The coupling efficiency between the signal and idler modes, and the fundamental mode of the single-mode fiber are given by $\Gamma_s = |\int dxdyU_s(x,y,\omega_s)U_0^*(x,y,\omega_0)|^2$ and $\Gamma_i = |\int dxdyU_i(x,y,\omega_i)U_0^*(x,y,\omega_0)|^2$. They yield a value of $\Gamma_s = \Gamma_i \approx 0.88$ in the whole bandwidth of interest, showing a minimal frequency dependence. All the modes are normalized so that $\int dxdy|U_j(x,y,\omega)|^2 = 1$ for $j = s,i,0$.

Neglecting the vacuum contribution in the final quantum state, normalizing and tracing out the frequency degree of freedom, the two-photon state can be represented by the following density matrix, where we use the conventional ordering of rows and columns as $\{|\mathrm{TE}\rangle_U|\mathrm{TE}\rangle_L, |\mathrm{TE}\rangle_U|\mathrm{TM}\rangle_L, |\mathrm{TM}\rangle_U|\mathrm{TE}\rangle_L, |\mathrm{TM}\rangle_U|\mathrm{TM}\rangle_L\}$:

$$
\hat{\rho}_n = \begin{pmatrix} 0 & 0 & 0 & 0 \\ 0 & \alpha_n & \gamma_n & 0 \\ 0 & \gamma_n^* & \beta_n & 0 \\ 0 & 0 & 0 & 0 \end{pmatrix},
\tag{2.10}
$$

where

$$
\begin{aligned}
\alpha_n &= 1/2 \int_{B_n} d\Omega |\Phi(\Omega)|^2, \\
\beta_n &= 1/2 \int_{B_n} d\Omega |\Phi(-\Omega)|^2, \\
\gamma_n &= 1/2 \int_{B_n} d\Omega \Phi\left(\Omega\right)\Phi^*\left(-\Omega\right),
\end{aligned}
\tag{2.11}
$$

with $\mathrm{Tr}[\hat{\rho}_\mathrm{n}] = \alpha_\mathrm{n} + \beta_\mathrm{n} = 1$.

Table 2.2: Parameters of the structure: t_c - core thickness; $t_{1,2}$ - thicknesses of the alternating layers of the Bragg reflector; x_c - aluminium concentration in the core; $x_{1,2}$ - aluminium concentrations in the reflector's layers; n_c - the refractive index in the core; $n_{1,2}$ - refractive indices in the reflector's layers; $\partial\beta_{s(i)}/\partial\Omega$ -the inverse group velocity of the signal (idler) photon. The structure is optimized for the collinear type-II SPDC.

Parameter	Value
t_c (nm)	370
t_1 (nm)	127
t_2 (nm)	309
$n_c(x_c = 0.7)$	3.177
$n_1(x_1 = 0.4)$	3.655
$n_2(x_2 = 0.9)$	3.064
Ridge width (nm)	1770
$\partial\beta_s/\partial\Omega$ (ns/m)	10.55
$\partial\beta_i/\partial\Omega$ (ns/m)	10.56
Waveguide length (mm)	1

2.3.2 Numerical Results

In the waveguide structure considered, the pump wavelength is 775.1 nm. The frequency spacing between channels is $\Delta = 50$ GHz and the bandwidth of each channel is 50 GHz, which corresponds approximately to 0.4 nm at 1550 nm. The channel width and the spacing between channels were chosen according to the typical values used in commercial WDM systems. Channel $n = 1$ corresponds to the wavelength 1549.6 nm in the upper path and to 1550.6 nm in the lower path.

In order to reach a high number of frequency channels, the BRW structure must be designed in such way, so as to permit the generation of signal-idler pairs with an ultra-broad spectrum in the type-II configuration. This is achieved when the group velocities of the TE and TM modes are equal [72, 89], i.e., $|\frac{\partial\beta_s}{\partial\Omega} - \frac{\partial\beta_i}{\partial\Omega}| \to 0$. The modes of the structure and its propagation constants are obtained as a numerical solution of the Maxwell equations inside the waveguide using the finite element method (see the Appendix A.2). The waveguide design has been optimized by a genetic algorithm according to the requirements. The final BRW design is composed of two Bragg reflectors, one placed above and one below the core. Each reflector contains 8 bi-layers. The Sellmeier equations for the refractive indices of the layers were taken from [90]. Table 2.2 summarizes the main parameters of the structure.

Inspection of Eq. (2.7) shows that the effective nonlinearity σ of the waveguide SPDC

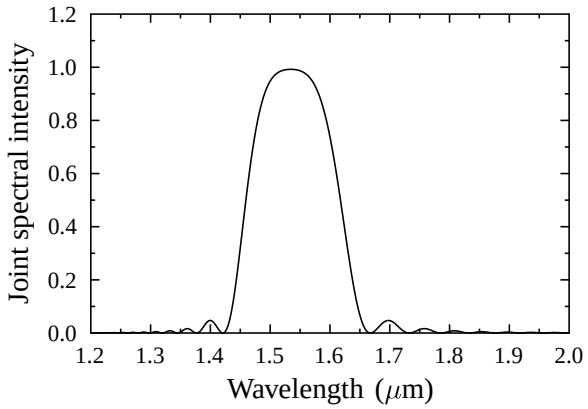

Figure 2.8: Joint spectral intensity $\sim |\Phi(\lambda)|^2$ of the biphoton generated in the Bragg reflection waveguide for type-II phase-matching (TM $\rightarrow$ TE + TM).

process depends on the effective area ($A_{\text{eff}} = 1/\Gamma^2$), which is related to the spatial overlap of the pump, signal and idler modes. For the structure considered, the effective area exhibits only minimal frequency dependence in the bandwidth of interest and it is equal to $A_{\text{eff}} = 35.3\ \mu\text{m}^2$. Despite the fact that the large effective area will reduce the strength of the interaction, the high nonlinear coefficient still results in an efficiency that is a much higher than for other phase-matching platforms in waveguides or in bulk media. The total emission rate [91] can be expressed using Eq. (2.8) as $R = \sigma^2 L^2 \int d\Omega |\Phi(\Omega)|^2$. For our BRW, the emission rate is $R_{\text{BRW}} \approx 5.7 \times 10^7$ photons/s/mW. For comparison, for a typical PPLN waveguide (type-0) similar to the one used in [85], we obtain $R_{\text{PPLN}} \approx 3.3 \times 10^7$ photons/s/mW. The intensity of the joint spectral amplitude, given by Eq. (2.8), is displayed in Fig. 2.8. Even though we are considering a type-II configuration, the width (FWHM) of the spectrum is a staggering 160 nm.

The degree of entanglement in each spectral channel can be quantified by calculating the concurrence C_n of the biphoton [92,93]. The concurrence is equal to 0 for a separable state and to 1 for a maximally entangled state. For the density matrix of Eq. (2.10) we obtain [94]

$$C_n = 2|\gamma_n|, \tag{2.12}$$

so the degree of entanglement depends on the symmetry of the spectral amplitude $\Phi(\Omega)$, i.e., if $\Phi(\Omega) = \Phi(-\Omega)$ the concurrence is maximum.

Figure 2.9 shows the values of α_n, β_n and C_n for the first 200 channels. $C_n > 0.9$ is reached for the first 179 channels. The decrease (increase) of the parameters β_n

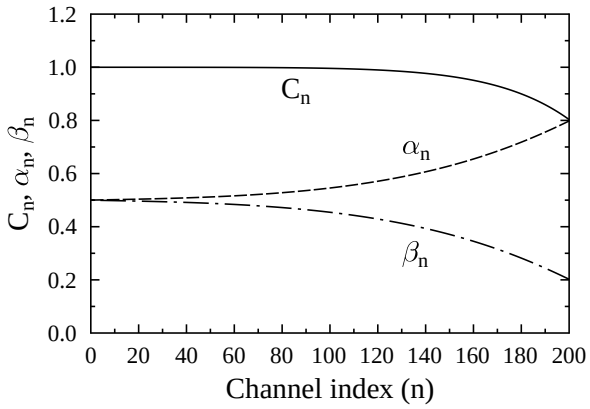

Figure 2.9: Coefficients C_n (solid line), α_n (dashed line) and β_n (dotted-and-dashed line) as a function of the frequency channel.

(α_n) reflects the fact that for frequency channels with a large detuning from the central frequency, one of the two polarization components of the polarization entangled state, $|\mathrm{TE}\rangle_1|\mathrm{TM}\rangle_2$ or $|\mathrm{TM}\rangle_1|\mathrm{TE}\rangle_2$, shows a greater amplitude probability. In this case, one of the two options predominates. Therefore, if the goal is to generate a quantum state of the form $|\Psi_2\rangle = 1/\sqrt{2}\ (\,|\mathrm{TE}\rangle_1|\mathrm{TM}\rangle_2 + |\mathrm{TM}\rangle_1|\mathrm{TE}\rangle_2\,)$ in a specific frequency channel with $\alpha_n, \beta_n \neq 1/2$, one can always modify the diagonal elements of the density matrix with a linear transformation optical system, keeping unaltered the degree of entanglement.

The number of frequency channels available depends on the concurrence required for the specific application. A good example is a linear optical gate relying on the interference of photons on a beam splitter [95, 96]. This would be especially important for the implementation of quantum teleportation, where the fidelity of the protocol depends strongly on the spectral indistinguishably between polarizations of the entangled state [97]. In Fig. 2.10 we plot the number of frequency channels available as a function of the minimum concurrence required. For instance, if we select only frequency channels with $C_n > 0.95$, we have at our disposal 162 channels, while for $C_n > 0.99$ this number is reduced to 121 channels.

In the implementation of the system considered here in a *real* fiber-optics network, the number of frequency channels available can be limited by several factors. For instance, it can be limited by the operational bandwidth of the demultiplexer (see Fig.1). This device should be designed to operate with the same broad spectral range of the photon pairs generated in the BRW waveguide.

When using a large number of channels, inspection of Fig. 2.8 shows that channels

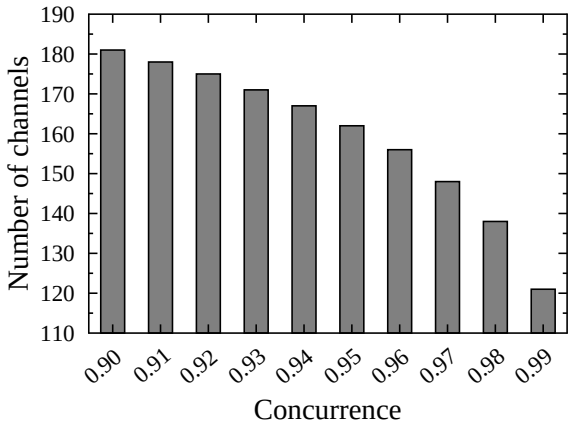

Figure 2.10: Number of channels available as a function of the minimum value of the concurrence required.

far apart from the central frequency will exhibit a lower brightness. In this case, spectral shapers or appropriately designed filters, should be used to flatten the emission spectrum, similarly to the case of broadband gain-flattened Erbium doped fiber amplifiers (EDFA). Notwithstanding, this might introduce some losses in the generation process, especially when considering a large number of channels, deteriorating the flux rate of the source. Interestingly, a similar problem appears in the context of optical coherence tomography (OCT), where large bandwidths are required to increase the imaging resolution. In OCT, spectral shapers are used to obtain an optimum (Gaussian-like) spectral shape [98].

Finally, we should mention that the generation of polarization-entangled photons with the large bandwidths considered here require a precise control the group velocities of the interacting waves, which in turn requires a precise control of the waveguide parameters: refractive index and layer widths. The effective number of available frequency channels in a specific application is inevitably linked to the degree of control of the fabrication process. Since both down-converted photons are propagating as TIR modes, they are more resistant to fabrication imperfections. For example, a change of about 10% in the aluminium concentration in the core will reduce the spectral bandwidth to 145 nm. Notwithstanding, it has to be stressed that the phase-matching condition for interacting waves is highly sensitive to any fabrication imperfection, therefore any small change of the structural parameters will lead to a shift of the central (phase-matched) wavelength.

2.4 Experimental Results for a typical Bragg Reflection Waveguide

In a previous work [25], the existence of time-correlated paired photons generated by means of SPDC in BRWs was reported, but the existence, and quality, of the entanglement present was never explored. The generation of polarization entanglement in alternative semiconductor platforms has been demonstrated recently in a silicon-based wire waveguide [26], making use of four-wave mixing, a different nonlinear process to the one considered here, and in a AlGaAs semiconductor waveguide [99], where as a consequence of the opposite propagation directions of the generated down-converted photons, two type-II phase-matched processes can occur simultaneously.

In this section, we experimentally demonstrate that the use of BRWs allows the generation of highly entangled pairs of photons in polarization via the observation of the violation of the Clauser-Horne-Shimony-Holt (CHSH) Bell-like inequality [6]. Bell's inequalities are a way to demonstrate entanglement [100], since the violation of a Bell's inequality makes impossible the existence of one joint distribution for all observables of the experiment, returning the measured experimental probabilities [101].

2.4.1 Device Description and Waveguide Characterization with Second Harmonic Generation

A schematic of the BRW used in the experiment is shown in Fig. 2.11. Grown on an undoped [001] GaAs substrate, the epitaxial structure has a three-layer waveguide core consisting of a 500 nm thick $Al_{0.61}Ga_{0.39}As$ layer and a 375 nm $Al_{0.20}Ga_{0.80}As$ matching-layer on each side. These layers are sandwiched by two symmetric Bragg reflectors, with each consisting of six periods of 461 nm $Al_{0.70}Ga_{0.30}As$/129 nm $Al_{0.25}Ga_{0.65}As$. A detailed description of the epitaxial structure can be found in [102]. The wafer was then dry etched along [110] direction to form ridge waveguides with different ridge widths. The device under test has a ridge width of 4.4 μm, a depth of 3.6 μm and a length of 1.2 mm. The structure supports three distinct phase-matching schemes for SPDC, namely: type-I process where the pump is TM-polarized and the down-converted photon pairs are both TE-polarized; type-II process where the pump is TE-polarized while the photons of a pair have mutually orthogonal polarization states, and type-0 process where all three interacting photons are TM-polarized [103]. For the experiment here, we investigate type-II SPDC, which is the nonlinear process that produce the polarizations of the down-converted photons required to generate polarization entanglement. Since both photons show orthogonal

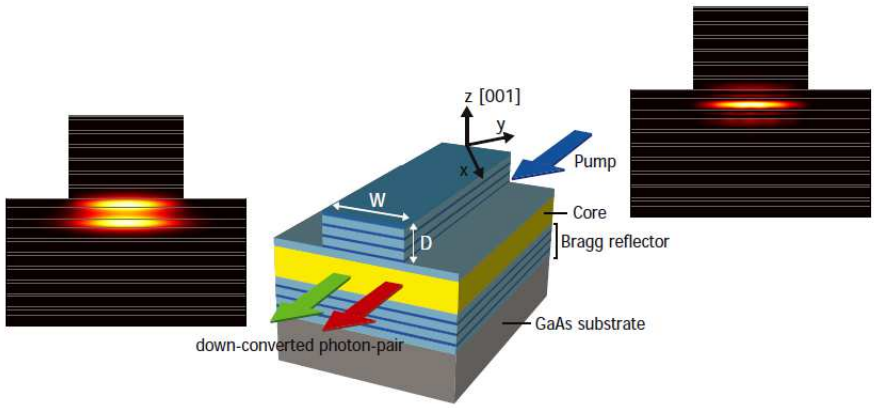

Figure 2.11: Bragg reflection waveguide structure used to generate paired photons correlated in time and polarization (type-II SPDC) at the telecommunication window (1550 nm). The insets show the spatial shape of the pump mode that propagates inside the waveguide as a Bragg mode, and the spatial shape of the down-converted, which are modes guided by total internal reflection (TIR). W: width of the ridge; D: depth of the ridge.

polarizations, after traversing a non-polarizing beam splitter and introducing in advance an appropriate temporal delay between them, they can result in a polarization-entangled pair of photons.

During the fabrication process of the BRW, slight changes in the thickness and aluminium concentration of each layer result in small displacements of the actual phase-matching wavelength from the design wavelength. For this reason, we first use second harmonic generation (SHG) before examining SPDC to determine the pump phase-matching wavelength for which the different schemes (type-I, type-II or type-0) are more efficient.

The experimental arrangement for SHG is shown in Fig. 2.12(a). The wavelength of a single-frequency tunable laser (the fundamental beam) was tuned from 1545 nm to 1575 nm. An optical system shapes the light into a Gaussian-like mode, which is coupled into the BRW to generate the second harmonic beam by means of SHG. At the output, the power of the second harmonic wave is measured to determine the efficiency of the SHG process. Figure 2.12(b) shows the phase-matching tuning curve showing the dependency of generated second-harmonic power on the fundamental wavelength. From the figure, three resonance SH features could be resolved corresponding to the three supported phase-matching schemes. As mentioned earlier, the process of interest here is type-II. For this particular type of phase-matching, maximum efficiency takes place at the fundamental wavelength of 1555.9 nm. To generate the second harmonic beam by means of type-II

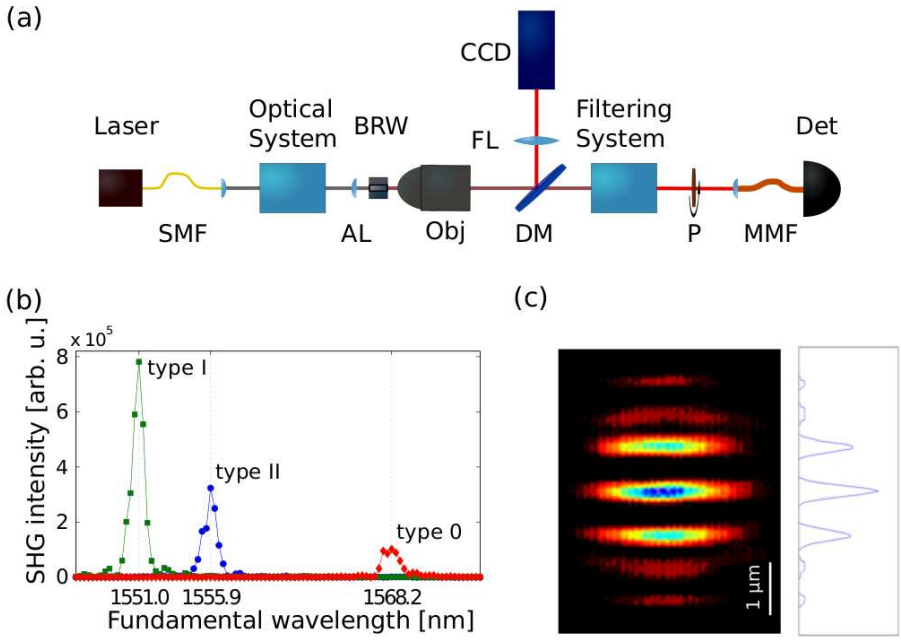

Figure 2.12: (a) Experimental setup for SHG. The pump laser is a tunable external-cavity semiconductor laser (TLK-L1550R, Thorlabs). The Optical System consists of a linear power attenuator, polarization beam splitter and a half-wave plate. The Filtering System consists of a neutral density filter and low-pass filter. SMF: single-mode fiber; AL: aspheric lens; BRW: Bragg reflection waveguide; Obj: Nikon 50×; DM: dichroic mirror; FL: Fourier lens; CCD: Retiga EXi Fast CCD camera; P: polarizer; MMF: multi-mode fiber; Det: single-photon counting module (SPCM, PerkinElmer). (b) Phase-matching curve of the BRW as a function of the wavelength of the fundamental wave. (c) Beam profile of the Bragg mode of the second harmonic wave generated by means of the SHG process, captured with a CCD camera after imaging with a magnification optical system of 100× (Fourier lens with focal length f=400 mm).

SHG in Fig. 2.12(b), we use a half-wave plate to rotate the polarization of the fundame ntal light coming from the laser by 45-degrees, to generate the required fundamental beams with orthogonal polarizations.

In BRW, phase-matching takes place between different types of guided modes which propagate with different longitudinal wavevectors. The fundamental beam (around 1550 nm) corresponds to a total internal reflection (TIR) mode, and the second harmonic beam (around 775 nm) is a Bragg mode. The measured spatial profile of this Bragg mode is shown in Fig. 2.12(c).

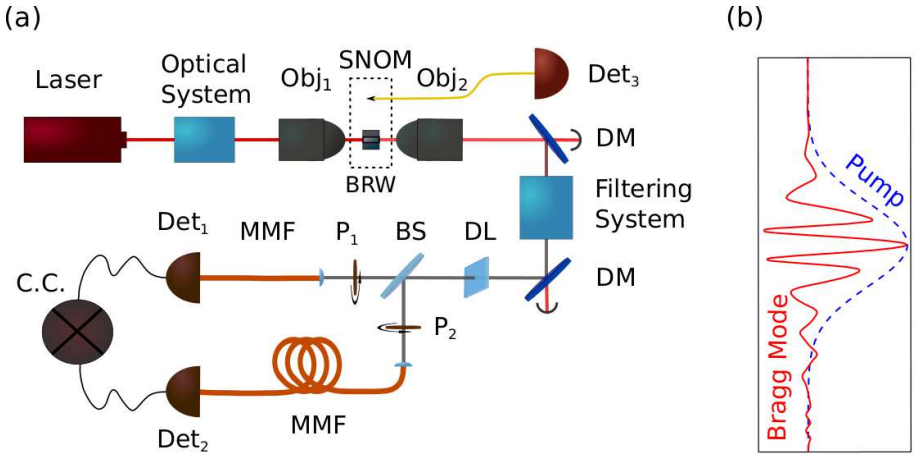

Figure 2.13: (a) Experimental setup for SPDC. The Optical System is composed of a linear power attenuator, spatial filter and beam expander. SNOM: scanning near-field optical microscope probe; BRW: Bragg reflection waveguide; Objectives: Obj_1 (Nikon 100×) and Obj_2 (Nikon 50×); DM: dichroic mirror; Filtering System: 2 DMs, band-pass and long-pass filters; DL: delay line (birefringent plate); BS: beam splitter; P_1 and P_2: linear film polarizers; MMF: multi-mode fiber; D_1 and D_2: InGaAs single-photon counting detection modules; D_3: low-power silicon detector; C.C.: coincidence-counting electronics. (b) Amplitude profiles of the theoretical Bragg mode and the Gaussian-like pump beam.

2.4.2 Generation of Polarization Entangled Photons

The experimental setup used to generate polarization-entangled paired photons and the measurement of the Bell-like inequality violation is shown in Fig. 2.13(a). The pump laser is a tunable single-frequency diode laser with an external-cavity (DLX 110, Toptica Photonics) tuned to 777.95 nm. Light from the laser traverses an optical system, with an attenuator module, spatial filter and beam expander, in order to obtain the proper input beam. Even though the optimum option for exciting the pump Bragg mode would be to couple directly into the photonic bandgap mode using a spatial light modulator (SLM), the small feature size in the field profile of the Bragg mode and its oscillating nature imposed serious challenges for using an SLM. Therefore, we choose instead to pump the waveguide with a tightly focused Gaussian pump beam (see Fig. 2.13(b)) with a waist of ~ 1.5 μm, that is coupled into the waveguide using a 100× objective. Our calculations show that the estimated modal overlap between the Gaussian pump beam and the Bragg mode of the waveguide is around 20%, which should be added to the total losses of the system. A scanning near-field optical microscope (SNOM) probe was attached to the support of the BRW, in order to perform sub-micrometric 3D beam profile scans to maximize the

coupling efficiency of the incident pump beam into the pump Bragg mode. The power of the laser light before the input objective was measured to be 13 mW. Taking into account the transmissivity of the objective for infrared light (70%), the transmissivity of the facet of the BRW (73%) and the calculated overlap between the laser light and the Bragg mode of the waveguide (around 20%), the estimated pump power available for SPDC process inside the waveguide is $\sim$ 1.3 mW.

The generated down-converted photons are collected using a 50× objective and separated from the pump photons using four dichroic mirrors (DM), band-pass and long-pass filters. Each DM has a 99% transmissivity at the pump wavelength. The attenuation of the band-pass filter (45 nm FWHM bandwidth centered at 1550 nm) is 10^{-4}, and the long-pass filter (cut-on wavelength: 1500 nm) introduces an additional attenuation of 10^{-3} at the pump wavelength.

In general, photons propagating in a waveguide with orthogonal polarizations have different group velocities (group velocity mismatch, GVM), which in conjunction with non-negligible group velocity dispersion (GVD), result in different spectra for the cross-polarized photons [89]. As a consequence, the polarization and frequency properties of the photons are mixed. The two photons of a pair could be, in principle, distinguished by their time of arrival at the detectors, as well as their spectra, which diminishes the quality of polarization entanglement achievable. In order to obtain high-quality polarization entanglement, it is thus necessary to remove all the distinguishing information coming from the temporal/frequency degree of freedom. For this reason, the 45 nm band pass filter was applied to remove most of the distinguishing spectral information, and off-chip compensation was implemented with a delay line to remove arrival time information.

A quartz birefringent plate with a length of 1 mm, vertically tilted around 30° was used to introduce a 32 fs time delay between photons, which is experimentally found to be the optimum value to erase temporal distinguishing information caused by the group velocity mismatch (GVM) and the GVD. The calculated group velocities for TE and TM down-converted photons are 8.98×10^7 m/s and 9.01×10^7 m/s, respectively. The GVD parameter is $D \sim$ -7.9×10^2 ps/(nm·km) for both polarizations. When considering these values of the GVM and GVD, our calculations show that the optimum delay for generating the highest degree of polarization entanglement is $\sim$ 31.2 fs, which agrees with the value obtained experimentally.

The down-converted photons are separated into arms 1 and 2 with a 50/50 beam

splitter (BS) in order to generate a polarization-entangled two-photon state of the form

$$\left|\Psi^{+}\right\rangle = \frac{1}{\sqrt{2}}\left\{\left|H\right\rangle_1\left|V\right\rangle_2 + \left|V\right\rangle_1\left|H\right\rangle_2\right\}, \tag{2.13}$$

where $|H\rangle$ and $|V\rangle$ denote the two possible polarizations of the photons (horizontal and vertical), propagating in arms 1 or 2. Horizontal (vertical) photons corresponds to photons propagating inside the waveguide as TE (TM) mode. We neglect cases where both photons leave the BS through the same output port, by measuring only coincidences between photons propagating in arms 1 and 2 (post-selection), which implies that 50% of the generated pairs are not considered. Finally, to measure Bell's inequality violations, the entangled photons are projected into different polarization states with linear film polarizers, and coupled into multi-mode fibers connected to InGaAs single-photon detection modules (id201, idQuantique), where optical and electronic delays are introduced to measure coincidental events with time-to-amplitude converter (TAC) electronics. The coincidences window for all measurements was set to 3 ns.

2.4.3 Violation of the CHSH Inequality

To obtain a first indication that the pairs of photons propagating in arms 1 and 2 are truly entangled in the polarization degree of freedom, so that their quantum state can be written of the form given by Eq. (2.13), one detects one of the photons, i.e., the photon propagating in arm 1, after projection into a specific polarization state $\left|\Psi\right\rangle_1 = \cos\theta_1\left|H\right\rangle_1 - \sin\theta_1\left|V\right\rangle_1$ [1], and measures in coincidence the remaining photon after projection into a set of polarization bases $\left|\Psi\right\rangle_2 = \cos\theta_2\left|V\right\rangle_2 + \sin\theta_2\left|H\right\rangle_2$, with θ_2 spanning from 0 to 2π [104]. Ideally, the coincidence counts as a function of θ_2 should follow the form of $\cos^2(\theta_1+\theta_2)$, which yields a visibility $V = (Max - Min)/(Max + Min)$ of 100%. Therefore, the highest the visibility measured, the highest the quality of the generated polarization-entangled state.

Figures 2.14(a) and (b) show the results of the measurements for two specific cases: $\theta_1 = 0°$ and $\theta_1 = 45°$. The measured visibility, subtracting the accidental coincidences, is 98% for $\theta_1 = 0°$, and to 91% for $\theta_1 = 45°$. Without subtraction of accidental coincidences, the corresponding measured visibility is 80% for $\theta_1 = 0°$ and 77% for $\theta_1 = 45°$. The accidental coincidences, with respect to the total number of events counted, were measured experimentally, introducing an electronic delay in the trigger of the second detector driving it out of the detection window of the first detector. The same electronic delay had to be introduced before the TAC electronics in order to have the coincidence events from the

[1] The chosen polarization states mirror the experimental arrangement implemented

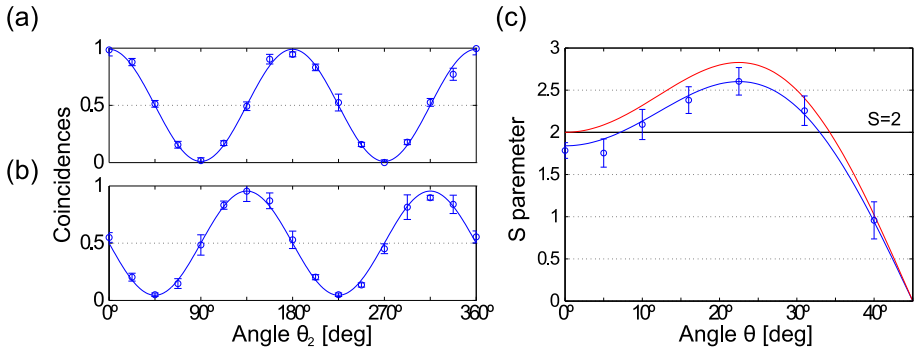

Figure 2.14: Normalized coincidence measurements as a function of the polarization state of photon 2 when photon 1 is projected into a polarization state with: (a) $\theta_1 = 0°$ and (b) $\theta_1 = 45°$. The data shown in (a) and (b) is subtracting from the raw data the number of accidental coincidences. (c) Violation of the CHSH inequality. Parameter S as a function of the angle θ. The small blue circles with error bars represent the experimental data with their standard deviations. The blue solid curves in (a) and (b) are theoretical predictions assuming that the visibility is 98% in (a) and 91% in (b). The red (upper) curve in (c) is the theoretical prediction for S. The blue curve in (c) is the best fit. The inequality holds if $S \leq 2$. The maximum value attained is $S = 2.61 \pm 0.16$. The data shown in (c) is without subtraction of accidental coincidences.

same amount of single events, but totally uncorrelated in this case. This technique made possible to measure the correct visibility of the fringes using the maximum efficiency detector settings, in order to obtain lower standard deviation of the measurements. The optimum trigger rate for this experiment was found to be 100 KHz, measuring an average of $3,550$ and $6,200$ photon counts per second in each detector, and a maximum flux rate of coincidences of 3 pairs of photons per second. The low trigger rate is one of the reasons for the observation of such a low flux rate of down-converted photons observed, since it implies that the detectors are closed most of the time. The detection window for these measurements was set to 100 ns.

In a CHSH inequality experiment [6], one measures photon coincidences between photon 1, after being projected into a polarization state defined by angles θ_1 or θ_1', and photon 2, after a similar polarization projection defined by angles θ_2 or θ_2'. The CHSH inequality holds if

$$S = |E(\theta_1, \theta_2) - E(\theta_1, \theta_2^{'}) + E(\theta_1^{'}, \theta_2) + E(\theta_1^{'}, \theta_2^{'})| \leq 2, \tag{2.14}$$

where

$$E(\theta_1,\theta_2)=\frac{C(\theta_1,\theta_2)+C(\theta_1^{\perp},\theta_2^{\perp})-C(\theta_1^{\perp},\theta_2)-C(\theta_1,\theta_2^{\perp})}{C(\theta_1,\theta_2)+C(\theta_1^{\perp},\theta_2^{\perp})+C(\theta_1^{\perp},\theta_2)+C(\theta_1,\theta_2^{\perp})} \tag{2.15}$$

and $\theta_{1,2}^{\perp}=\theta_{1,2}+90°$. Figure 2.14(c) shows the value of the parameter S as a function of the angle θ, where $\theta\equiv\theta_2-\theta_1=\theta_2^{'}+\theta_1^{'}=-\theta_2-\theta_1^{'}$, which attains the maximum possible violation, i.e., $S=2\sqrt{2}$. For the ideal case, one would obtain $S(\theta)=3\cos 2\theta-\cos 6\theta$, which is the red (upper) curve depicted in Fig. 2.14(c). Sixteen measurements were performed for each value of the angle θ. For the maximum inequality violation ($\theta=22.5°$), the polarizer settings were $\theta_1=0°$, $\theta_1^{'}=-45°$, $\theta_2=22.5°$ and $\theta_2^{\prime}=67.5°$. In this case, we obtained a value of the inequality of $S=2.61\pm0.16$, which represents a violation by more than 3 standard deviations. This represents a stronger violation of the CHSH inequality than previously reported [99] for a vertically pumped BRW structure, where the measured value was $S=2.23\pm0.11$.

Regarding the measurements of the S parameter, no accidental coincidences were subtracted from the absolute measurement obtained. In order to increase the signal-to-noise ratio, the detection window in both detectors was decreased to 20% of its previous time duration (from 100 ns to 20 ns), having thus a corresponding decrease in total number of single and coincidence counts detected. Now, the measured average flux rate is 600 and 500 photon counts per second in each detector, and a maximum value of 0.3 pairs of photons per second.

To estimate the efficiency of the SPDC process, we take into account that the detection window is $\tau=20$ ns, and the trigger rate of detection is 100 kHz. The efficiency of each single-photon detector is 25%. The pump power injected into the BRW waveguide is estimated to be around 1.3 mW. Assuming that the transmissivity of each optical system, traversed by signal/idler photons, not including detection efficiency, is $\sim 10\%$, it results in an estimated SPDC efficiency of $\sim 10^{-10}$ in the filtering bandwidth.

Summary of this Section

In Section 2.2, we have presented and analyzed a new source for photon pairs that allows the generation of paired photons that lack any frequency correlation. These are of paramount importance for quantum networking technologies and quantum information processing. The source is based on Bragg reflection waveguides composed of $Al_xGa_{1-x}N$. Quasi-phase-matching of the waveguide core is used to achieve phase-matching at the desired wavelength. The control of waveguide dispersion is used to control the frequency correlation between the generated photons. Two Bragg reflection waveguide structures

have been presented. One of the structures allows us to generate uncorrelated photons with different spectra. The down-converted uncorrelated photons generated in the second structure are spectrally indistinguishable. This technique offers a promising route for the realization of electrically pumped, monolithic photon–pair sources on a chip with versatile characteristics.

In Section 2.3, BRWs are shown as a highly efficient waveguide source for generating polarization-entangled photon pairs for its use in multi-frequency QKD networks. In spite of being a type-II SPDC source, the achieved bandwidth is even larger than the bandwidth usually obtained with type-I or type-0 sources. The key enabling factor that allows us to achieve high efficiency of the nonlinear process together with a bandwidth increase is the fact that we can use a longer nonlinear material in a type-II configuration, while at the same time keeping the broadband nature of the SPDC process through the appropriate design of the Bragg reflection waveguide structure.

Finally, in Section 2.4, we have demonstrated that polarization-entangled paired photons generated in a semiconductor Bragg reflection waveguide (BRW) show a visibility higher than 90% in all the bases measured, a requisite for obtaining high quality entanglement. It has also been experimentally demonstrated that the generated two-photon state clearly violate the CHSH inequality, and that the presented BRW source can be considered an expedient source of high-quality polarization-entangled two-photon states.

Publications related to the content of this Section

The main results presented in this chapter have been published in the following papers:

J. Svozilík, M. Hendrych, A. S. Helmy, and J. P. Torres, Opt. Express 19, 3115 (2011).
J. Svozilík, M. Hendrych, and J. P. Torres, Opt. Express 20, 15015 (2012).
A. Valles, M. Hendrych, J. Svozilík, R. Machulka, P. Abolghasem, D. Kang, B. J. Bijlani, A. S. Helmy, and J. P. Torres, Opt. Express 21, 10841 (2013).

Chapter 3

Entanglement in the Spatial Degree of Freedom: new sources

3.1 Introduction

The boom of interest in light possessing orbital angular orbital momentum (OAM) was ignited by a paper published in 1992 by Allen et al. [105], which showed that certain light beams, easily generated, such as Laguerre Gauss beams, posses indeed OAM as a natural feature. Prior to this paper, there were many studies considering waves with singularities, waves with an helical phase profile around these singularities (see, for instance, [106,107]). Production of the above mentioned phase-singularities in light has been shown by Vaughan and Willetts [108], who make use of the fact that a combination of Hermite-Gaussian modes leads to Laguerre-Gaussian beams, which show a helically-phased wave-front. These beams also represents an important modeling tool of laser dynamics [109].

The basic property of light with OAM is a helical phase-front with the amount of interwined helices corresponding to the OAM (winding) number $l \in \mathcal{Z}$ [110]. This number is unbounded and its limitation, in experiments, is given only by selected technologies. For these beams, it is characteristic an azimuthal field dependence of the formexp $(il\theta)$. As a paraxial light beam can posses both spin angular momentum (SAM) σ (which is related to the right- or left- handed circular polarization) together with the OAM, the total angular momentum of light can be expressed as $(l + \sigma)\hbar$. This expression has a lot of physical implications, namely in the case of mechanical effects of light [111]. Besides the above mentioned Laguerre- Gaussian beams, also Mathieu beams and Bessel beams can exhibit a non-zero orbital angular momentum. Bessel beams are considered later as a natural orthogonal basis for the transverse domain mode decomposition and the

subsequent determination of the spiral spectra [112]. These spectral decompositions can be related to the concept of Heisenberg uncertainty in the transverse domain of light [113].

During the last few years, many effective ways to create and measure the OAM of light have been developed. Most of these methods can be reversed and used for the estimation of the winding number l. The simple use of a forked diffraction grating transforms an incident beam to a helical one, and vice versa, in the first diffraction order [114]. Other method is based on the use of spiral phase-plates [115]. Anisotropic and inhomogeneous crystals, so called "q-plate", can be used to mutually couple the spin and orbital angular momentum degrees of freedom [116]. Additionally, a set of cylindrical lenses provides a conversion method of Hermite- Gaussian modes to Laguerre-Gaussian modes [105]. Recently, a large amount of fiber-based techniques for preparing ligth with OAM light have been presented [117, 118]. For instance, a ring resonator with periodic grating was shown to be able generate vortex beams [119]. Optical fields with a non-zero OAM are of great interest in a myriad of scientific and technological applications, such as secure communications [120], ultra-precise measurements [13, 121], nano-particle manipulation [122] or quantum computing [123].

In Section 3.2, we present an scenario for the generation of many entangled OAM modes in a periodically poled nonlinear crystal. We make use of crystals with chirped quasi-phase-matching that leads to an enormous enhancement of the spectrum of OAM modes generated. In the next Section 3.3, we introduce a novel method of generation of photon pairs with a well-defined OAM in a non-linear SiO_2 silica fiber with a ring shaped core (that allows to preserve OAM modes). We consider thermally induced χ^2 non-linearity, since standard silica-based fibers lack this kind of non-linearity.

3.2 High Spatial Entanglement via Chirped Quasi-Phase-Matched Optical Parametric Down-conversion

Entangling systems in higher dimensional systems (frequency and spatial degrees of freedom) is important both for fundamental and applied reasons. For example, noise and decoherence tend to degrade quickly quantum correlations. However, theoretical investigations predict that physical systems with increasing number of dimensions can maintain non-classical correlations in the presence of more hostile noise [124, 125]. Higher dimensional states can also exhibit unique outstanding features. The potential of higher-dimensional quantum systems for practical applications is clearly illustrated in the demonstration of the so-called *quantum coin tossing* protocol, where the power of higher dimensional spaces

is clearly visible [126].

The amount of spatial entanglement generated depends of the SPDC geometry used (collinear vs non-collinear), the length of the nonlinear crystal (L) and the size of the pump beam (w_0). To obtain an initial estimate, let us consider a collinear SPDC geometry. Under certain approximations [1], the entropy of entanglement can be calculated analytically. Its value can be shown to depend on the ratio L/L_d, where $L_d = k_p w_0^2/2$ is the Rayleigh range of the pump beam and k_p is its longitudinal wavenumber. Therefore, large values of the pump beam waist w_0 and short crystals are ingredients for generating high entanglement [127]. However, the use of shorter crystals also reduce the total flux-rate of generated entangled photon pairs. Moreover, certain applications might benefit from the use of focused pump beams. For instance, for a $L = 1$ mm long stoichiometric lithium tantalate (SLT) crystal, with pump beam waist $w_0 = 100$ μm, pump wavelength $\lambda_p = 400$ nm and extraordinary refractive index $n_e(\lambda_p) = 2.27857$ [128], one obtains $E \sim 8.5$. For a longer crystal of $L = 20$ mm, the amount of entanglement is severely reduced to $E \sim 4.2$ ebits.

We put forward here a scheme to generate massive spatial entanglement, i. e., an staggering large value of the entropy of entanglement, independently of some relevant experimental parameters such as the crystal length or the pump beam waist. This would allow to reach even larger amounts of entanglement that possible nowadays with the usual configurations used, or to attain the same amount of entanglement but with other values of the nonlinear crystal length or the pump beam waist better suited for specific experiments.

Our approach is based on a scheme originally used to increase the bandwidth of parametric down-conversion [129, 130, A5]. A schematic view of the SPDC configuration is shown in Fig.3.1. It makes use of chirped quasi-phase-matching (QPM) gratings with a linearly varying spatial frequency given by $K_g(z) = K_0 - \alpha(z + L/2)$, where K_0 is the grating's spatial frequency at its entrance face ($z = -L/2$), and α is a parameter that represents the degree of linear chirp. The period of the grating at distance z is $p(z) = 2\pi/K_g(z)$, so that the parameter α writes:

$$\alpha = \frac{2\pi}{L}\frac{p_f - p_i}{p_f p_i} \tag{3.1}$$

where p_i is the period at the entrance face of the crystal, and p_f at its output face.

The key idea is that at different distances along the nonlinear crystal, signal and

[1] The approximation consist of substituting the sinc function appearing later on in Eq. (3.7) by a Gaussian function, i.e. $\operatorname{sinc} bx^2 \approx \exp\left[-\gamma b x^2\right]$ with $\gamma = 0.499$, so that both functions coincide at the 1/2-intensity. For a detailed calculation, see K. W. Chan, J. P. Torres, and J. H. Eberly, Phys. Rev. A **75**, 050101 (2007).

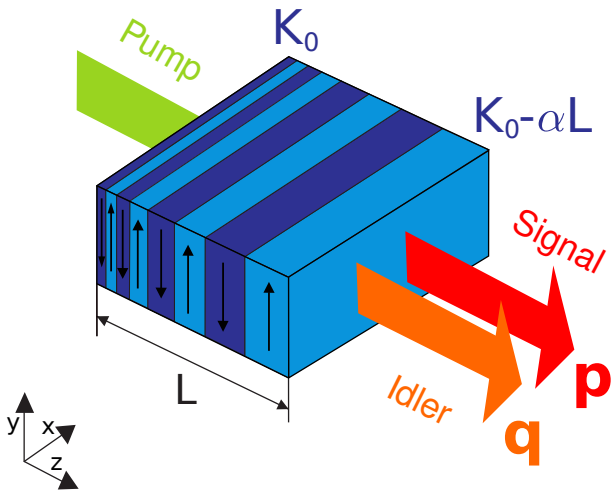

Figure 3.1: Scheme of SPDC in a linearly chirped quasi-phase-matched nonlinear crystal. The pump beam is a Gaussian beam, and **p** and **q** designate the transverse wave numbers of the signal and idler photons, respectively. K_0 is the grating wave-vector at the input face of the nonlinear crystal, and $K_0 - \alpha L$ at its output face. The signal and idler photons can have different polarizations or frequencies. The different colors (or different direction of arrows) represent domains with different sign of the nonlinear coefficient.

idler photons with different frequencies and transverse wavenumbers can be generated, since the continuous change of the period of the QPM gratings allows the fulfillment of the phase-matching conditions for different frequencies and transverse wavenumbers. If appropriately designed narrow-band interference filters allow to neglect the frequency degree of freedom of the two-photon state, the linearly chirped QPM grating enhance only the number of spatial modes generated, leading to a corresponding enhancement of the amount of generated spatial entanglement.

3.2.1 Theoretical Model

In order to determine how much spatial entanglement can be generated in SPDC with the use of chirped QPM, let us consider a nonlinear optical crystal illuminated by a quasi-monochromatic laser Gaussian pump beam of waist w_0. Under conditions of collinear propagation of the pump, signal and idler photons with no Poynting vector walk-off, which would be the case of a noncritical type-II quasi-phase matched configuration, the amplitude of the quantum state of the generated two-photon pair generated in SPDC

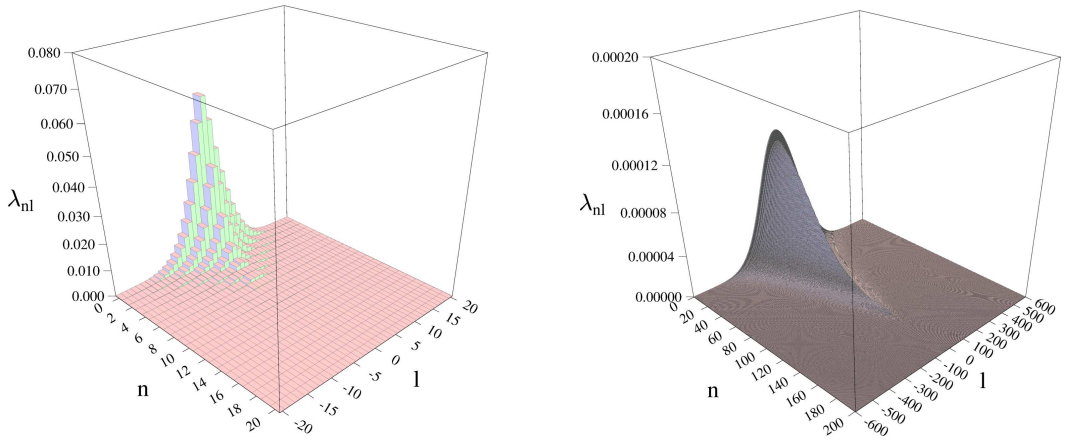

(a) (b)

Figure 3.2: Weight of the Schmidt coefficients λ_{nl} for (a) $\alpha = 0\ \mu m^{-2}$ and (b) $\alpha = 10 \times 10^{-6}\ \mu m^{-2}$. The nonlinear crystal length is $L = 20$ mm and the pump beam waist is $w_0 = 100\ \mu m$.

reads in transverse wavenumber space:

$$|\Psi\rangle = \int d\mathbf{p} \int d\mathbf{q} \Psi\left(\mathbf{p},\mathbf{q}\right) |\mathbf{p}\rangle_s |\mathbf{q}\rangle_i, \tag{3.2}$$

where $\mathbf{p}$ ($\mathbf{q}$) is the transverse wavenumber of the signal (idler) photon. Ψ is the joint amplitude of the two-photon state, so that $|\Psi\left(\mathbf{p},\mathbf{q}\right)|^2$ is the probability to detect a signal photon with transverse wave-number $\mathbf{p}$ in coincidence with an idler photons with $\mathbf{q}$.

The joint amplitude that describes the quantum state of the paired photons generated in a linearly chirped QPM crystal, using the paraxial approximation, is equal to

$$\begin{aligned} \Psi\left(\mathbf{p},\mathbf{q}\right) &= C \exp\left(-\frac{w_0^2}{4}|\mathbf{p}+\mathbf{q}|^2\right) \\ &\times \int_{-L/2}^{L/2} dz \exp\left[i\frac{|\mathbf{p}-\mathbf{q}|^2}{2k_p} z + i\alpha\left(z+\frac{L}{2}\right)z\right], \end{aligned} \tag{3.3}$$

where C is a normalization constant ensuring $\int d\mathbf{q} \int d\mathbf{p} |\Psi\left(\mathbf{p},\mathbf{q}\right)|^2 = 1$. Notice that the value of $K_0 = 2\pi/p(-L/2)$ does now show up in Eq.(3.4), since we make use of the fact that there is phase matching for $\mathbf{p} = \mathbf{q} = 0$ at certain location inside the nonlinear crystal, which in our case it turns out to be the input face ($z = -L/2$).

After integration along the z-axis one obtains

$$\begin{aligned}\Psi(\mathbf{p},\mathbf{q}) &= C\sqrt{\frac{i\pi}{4\alpha}}exp\left[-\frac{w_0^2}{4}|\mathbf{p}+\mathbf{q}|^2 - i\left(\frac{\alpha L^2}{16}+\frac{L|\mathbf{p}-\mathbf{q}|^2}{8k_p}+\frac{|\mathbf{p}-\mathbf{q}|^4}{16\alpha k_p^2}\right)\right] \\ &\times\left[\mathrm{erf}\left(\frac{3\sqrt{\alpha}L}{4\sqrt{i}}+\frac{|\mathbf{p}-\mathbf{q}|^2}{4k_p\sqrt{i\alpha}}\right)-\mathrm{erf}\left(-\frac{\sqrt{\alpha}L}{4\sqrt{i}}+\frac{|\mathbf{p}-\mathbf{q}|^2}{4k_p\sqrt{i\alpha}}\right)\right], \qquad (3.4)\end{aligned}$$

where erf refers to the error function. Notice that Eq.(3.4) is similar to the one describing the joint spectrum of photon pairs in the frequency domain, when the spatial degree of freedom is omitted [130,A5]. The reason is that both equations originate in phase matching conditions along the propagation direction (z axis).

Since all the configuration parameters that define the down conversion process show rotational symmetry along the propagation direction z, the joint amplitude given by Eq. (3.4) can be written as

$$\Psi(\mathbf{p},\mathbf{q}) = \sum_{l=-\infty}^{\infty} B_l(p,q)\, e^{il(\varphi_p-\varphi_q)}. \qquad (3.5)$$

Here, we have made use of polar coordinates in the transverse wave-vector domain for the signal, $\mathbf{p} = (p\cos\varphi_p, p\sin\varphi_p)$, and idler photons $\mathbf{q} = (q\cos\varphi_q, q\sin\varphi_q)$, where $\varphi_{p,q}$ are the corresponding azimuthal angles, and p, q are the radial coordinates. The specific dependence of the Schmidt decomposition on the azimuthal variables φ_p and φ_p reflects the conservation of orbital angular momentum in this SPDC configuration [131], so that a signal photon with OAM winding number $+l$ is always accompanied by a corresponding idler photon with OAM winding number $-l$. The probability of such coincidence detection for each value of l is the spiral spectrum [132] of the two-photon state, i.e., the set of values $P_l = \int pdp\, qdq\, |B_l(p,q)|^2$. Recently, the spiral spectrum of some selected SPDC configuration have been measured [133].

The Schmidt decomposition [9, 134] of the spiral function, i.e.,

$$B_l(p,q) = \sum_{n=0}^{\infty}\sqrt{\lambda_{nl}} f_{nl}(p) g_{nl}(q), \qquad (3.6)$$

is the tool to quantify the amount of entanglement present. λ_{nl} are the Schmidt coefficients (eigenvalues), and the modes f_{nl} and g_{nl} are the Schmidt modes (eigenvectors). Here we obtain the Schmidt decomposition by means of a singular-value decomposition method. Once the Schmidt coefficients are obtained, one can obtain the entropy of entanglement as $E = -\sum_{nl}\lambda_{nl}\log_2\lambda_{nl}$. An estimation of the overall number of spatial modes generated is obtained via the Schmidt number $K = 1/\sum_{nl}\lambda_{nl}^2$, which can be interpreted as a measure

of the effective dimensionality of the system. Finally, the spiral spectrum is obtained as $P_l = \sum_n \lambda_{nl}$.

3.2.2 Numerical Results

For the sake of comparison, let us consider first the usual case of a QPM SLT crystal with no chirp, i.e., $\alpha = 0\,\mu m^{-2}$, and length $L = 20$ mm, pumped by a Gaussian beam with beam waist $w_0 = 100\,\mu m$ and wavelength $\lambda_p = 400$ nm. In this case, the integration of Eq. (3.4) leads to [135]

$$\Psi(\mathbf{p},\mathbf{q}) = C \exp\left(-\frac{w_0^2}{4}|\mathbf{p}+\mathbf{q}|^2\right)\mathrm{sinc}\left(\frac{L|\mathbf{p}-\mathbf{q}|^2}{4k_p}\right). \tag{3.7}$$

The Schmidt coefficients are plotted in Fig. 3.2(a), and the corresponding spiral spectrum is shown in Fig. 3.3(a). The main contribution to the spiral spectrum comes from the spatial modes with $l = 0$. The entropy of entanglement for this case is $E = 6.4$ ebits and the Schmidt number is $K = 42.9$.

Nonzero values of the chirp parameter α lead to an increase of number of generated modes, as it can be readily seen in Fig. 3.2(b) for $\alpha = 10 \times 10^{-6}\ \mu m^{-2}$ and $w_0 = 100\ \mu$m. This broadening effect is also reflected in the corresponding broadening of spiral spectrum, as shown in Fig. 3.3(b). Indeed, Fig. 3.4(a) shows that the entropy of entanglement increases with increasingly larger values of the chirping parameter, even though for a given value of w_0, its increase saturates for large values of α. For $w_0 = 300\,\mu m$ and $\alpha = 10 \times 10^{-6}\,\mu m^{-2}$, we reach a value of $E = 16.6$ ebits. On the contrary, the Schmidt number K rises linearly with α, as can be observed in Fig. 3.4(b), for all values of w_0. For sufficiently large values of w_0 and α, K reaches values of several thousands of spatial modes, i.e. $K = 87113$ for the same w_0 and α. For large values of E, a further increase of E requires an even much larger increase of the number of spatial modes involved, which explain why an increase of the number of modes involved only produces a modest increase of the entropy of entanglement. Notice that the spiral spectrum presented in Fig. 3.3(b) is discrete. Notwithstanding, it might look continuous since it is the result from the presence of several hundreds of OAM modes with slightly decreasing weights.

We have discussed entanglement in terms of transverse modes which arise from the Schmidt decomposition of the two-photon amplitude and, as such, they attain appreciable values in the whole transverse plane. Alternatively, the existing spatial correlations between the signal and idler photons can also be discussed using second-order intensity correlation functions [136]. In this approach, correlations are quantified by the size of the

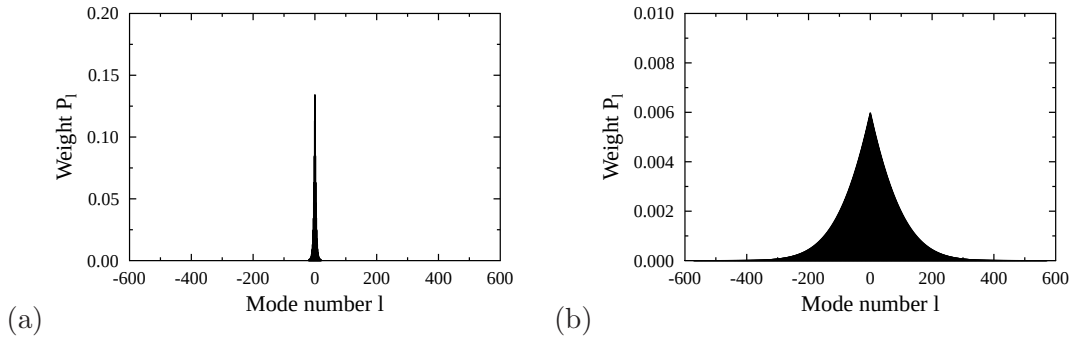

Figure 3.3: The spiral spectrum P_l for (a) $\alpha = 0\ \mu m^{-2}$ and (b) $\alpha = 10 \times 10^{-6}\ \mu m^{-2}$. The nonlinear crystal length is $L = 20$ mm and the pump beam waist is $w_0 = 100\ \mu m$.

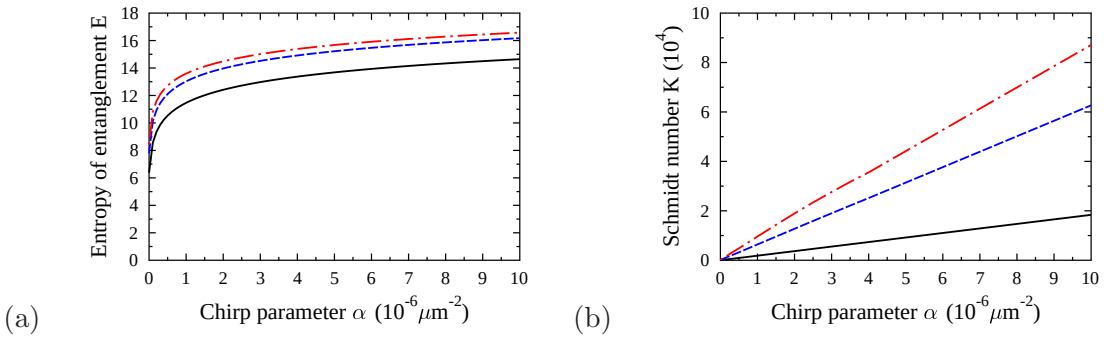

Figure 3.4: (a) The entropy of entanglement E and (b) the Schmidt number K as a function of the chirp parameter α for $w_0 = 100\ \mu m$ (solid black line), $w_0 = 200\ \mu m$ (dashed blue line) and $w_0 = 300\ \mu m$ (dotted-and-dashed red line).

correlated area ($\mathbf{\Delta p}$) where it is highly probable to detect a signal photon provided that its idler twin has been detected with a fixed transverse wave vector $\mathbf{q}$. We note that the azimuthal width of correlated area decreases with the increasing width of the distribution of Schmidt eigenvalues along the OAM winding number l. On the other hand, the increasing width of the distribution of Schmidt eigenvalues along the remaining number n results in a narrower radial extension of the correlated area. An increase in the number of modes K results in a diminishing correlation area, both in the radial and azimuthal directions. The correlated area drops to zero in the limit of plane-wave pumping, where attains the form of a δ function. The use of such correlations in parallel processing of information represents the easiest way for the exploitation of massively multi-mode character of the generated beams.

3.3 Generation of Photon Pairs With Nonzero Orbital Angular Momentum in a Ring Fiber

The observation of OAM entanglement in bulk materials has been already demonstrated [137–140], but in optical fibres it still represents a challenge. There are mainly two problems to overcome. On the one hand, the presence of inverse symmetry in ideally cylindrically-shaped silicon optical fibres excludes the existence of $\chi^{(2)}$ nonlinearity. For this reason, photon pairs in optical fibers are generally generated by means of an alternative nonlinear process (four-wave mixing) which utilizes instead the third-order nonlinearity of silicon [30, 141, 142]. Small values of the elements of $\chi^{(3)}$ nonlinear tensor can be compensated by increasing the interaction length of the fiber to give higher photon-pair fluxes. Unfortunately, this is accompanied by an equal enhancement of other effects, i.e., Raman scattering, that cause unwanted higher noise contributions to the generated flux. The inverse symmetry of silicon optical fibers can be broken by the method of thermal poling [143, 144] which provides a nonzero $\chi^{(2)}$ nonlinearity [145–147].

On the other hand, the propagation of photons with OAM in the usual step-index long optical fibers do not prevent cross-talk among modes with different OAM from being strong, which results in the fast deterioration of the purity of the OAM propagating modes. However, modern technology suggest also here a solution in the form of ring and vortex fibers with ring-shaped cores [148] that are more resistant against cross-talk. Here, we show that photon pairs entangled as OAM modes can be generated in this type of SiO_2 fiber with a thermal poling.

3.3.1 Theoretical Model of a Ring Fiber

The profile of the ring fiber considered here, with a ring-shaped core, is shown in Fig. 3.5. Since the location of two holes, serving for poling wires, is far away from the ring core (typically around 31 μm [149]), we can neglect their presence in the determination of optical fields in proximity of the core. This considerably simplifies subsequent calculations of the characteristics of propagating guided modes as one can assume modes with a rotational symmetry that solve the Maxwell equations.

In rotationally symmetric systems, the full electric ($\mathbf{E}$) and magnetic ($\mathbf{H}$) fields can be derived from their longitudinal components E_z and H_z. Moreover, they can be written as the product of a function that depends only on the azimuthal coordinate (θ), and an another function that depends only on the radial coordinate (r), i.e., E_z, $H_z \sim f(r)g(\theta)\exp[i(\beta z - \omega t)]$, where functions $f(r)$ and $g(\theta)$ describe spatial profiles of fields

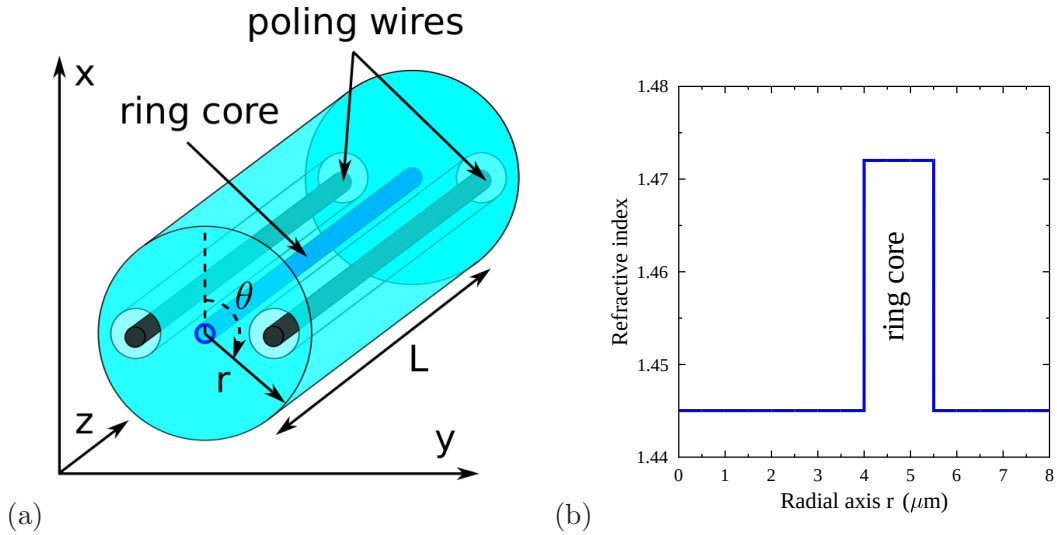

Figure 3.5: (a) Sketch of the vortex fiber with poling wires and (b) the radial profile of pump index of refraction around the fiber core for $\theta = 0$ deg for the fiber made of SiO_2 (at 1550 nm).

along the radial and azimuthal directions, respectively. The functions $f(r)$ and $g(\theta)$ thus satisfy the eigenvalue equations:

$$r^2\frac{\mathrm{d}^2 f(r)}{\mathrm{d}r^2} + r\frac{\mathrm{d}f(r)}{\mathrm{d}r} + r^2\left(\frac{\omega^2\varepsilon_r}{c^2} - \beta^2\right) f(r) - n^2 f(r) = 0, \tag{3.8}$$

$$\frac{\mathrm{d}^2 g(\theta)}{\mathrm{d}\theta^2} + n^2 g(\theta) = 0, \tag{3.9}$$

where β is the propagation constant (eigenvalue) of a guided mode with frequency ω; c denotes the velocity of light in the vacuum and ε_r means the relative dielectric permittivity. Radial profile of $\sqrt{\epsilon_r}$ is shown in Fig.3.5b. To simplify our calculations, we consider ε_r only as a scalar-function. Integer number n counts eigenmodes that are solutions of Eq.(3.9) describing azimuthal properties of optical fields. Details of procedure of solving Eq.(3.8) and (3.9) can be found in the Appendix A.3. Solutions of Eq.(3.9) have the form of harmonic functions with frequencies determined by n. On the other hand, solutions of Eq.(3.8) for a fixed value n are expressed in terms of the Bessel functions. For fixed values of frequency ω and index n, the continuity requirements on core boundaries admit only a discrete set of eigenmodes with suitable values of propagation constants β [150, 151]. If we take into account field polarizations, we reveal the usual guided modes of optical

fibers that are appropriate also for describing photon pairs. Spatial modes characterized by an OAM (winding) number l are th en obtained as suitable linear combinations of the above fiber eigenmodes $\mathbf{e}_\eta(\omega)$ classified by multi-index η that includes azimuthal number n, radial index of solutions of Eq. (3.8) and polarization.

At the single-photon level, the nonlinear process of SPDC converts a pump photon into a photon pair described by a state $|\psi\rangle$ given as a first-order perturbation solution of the Schrödinger equation:

$$|\psi\rangle = -\frac{i}{\hbar}\int_{-\infty}^{\infty} dt\, \hat{H}_I(t)|\mathrm{vac}\rangle; \tag{3.10}$$

$|\mathrm{vac}\rangle$ denotes the initial signal and idler vacuum state and $\hbar$ is the reduced Planck constant. The interaction nonlinear Hamiltonian $\hat{H}_I$ occurring in Eq. (3.10) is written in the radial coordinates as:

$$\begin{aligned}\hat{H}_I(t) &= 2\varepsilon_0 \int_{S_\perp} r dr d\theta \int_{-L}^{0} dz\, \chi^{(2)}(z) : \mathbf{E}_p^{(+)}(r,\theta,z,t) \\ &\quad \times \hat{\mathbf{E}}_s^{(-)}(r,\theta,z,t)\hat{\mathbf{E}}_i^{(-)}(r,\theta,z,t) + \mathrm{h.c.},\end{aligned} \tag{3.11}$$

where subscripts p, s and i denote in turn the pump, signal and idler fields. Symbol : is tensor shorthand with respect to three indexes of $\chi^{(2)}$ tensor and ε_0 denotes the vacuum permittivity and h.c. replaces the Hermitian conjugated term. Symbol $S_\perp$ means the transverse area of the fiber of length L. Nonlinear susceptibility $\chi^{(2)}$ with spatial periodic rectangular modulation such that it gives quasi-phase-matching of the interacting fields is assumed. Quasi-phase-matching is reached by thermal poling of the SiO_2 fiber that provides the following non-zero $\chi^{(2)}$ elements: $\chi^{(2)}_{xxx} \simeq 3\chi^{(2)}_{xyy}$ and $\chi^{(2)}_{xyy} = \chi^{(2)}_{yxx} = \chi^{(2)}_{yxy} =$ 0.021 pm/V [144].

The fiber is pumped by a strong (classical) pump beam which positive-frequency part $\mathbf{E}_p^{(+)}$ of the electric-field amplitude can be decomposed into the above introduced eigenmodes $\mathbf{e}_{p,\eta_p}(\omega_p)$ as:

$$\begin{aligned}\mathbf{E}_p^{(+)}(r,\theta,z,t) &= \sum_{\eta_p} A_{p,\eta_p} \int d\omega_p\, \mathcal{E}_p(\omega_p)\mathbf{e}_{p,\eta_p}(r,\theta,\omega_p) \\ &\quad \times \exp\left(i[\beta_{p,\eta_p}(\omega_p)z - \omega_p t]\right).\end{aligned} \tag{3.12}$$

In Eq. (3.12), A_{p,η_p} gives the amplitude of mode η_p and $\mathcal{E}_p$ denotes the normalized pump amplitude spectrum. Similarly, the negative-frequency parts $\hat{\mathbf{E}}_s^{(-)}$ and $\hat{\mathbf{E}}_i^{(-)}$ of the signal

and idler electric-field operators can be written as:

$$\begin{aligned}\hat{\mathbf{E}}_a^{(-)}(r,\theta,z,t) &= \sum_{\eta_a}\int d\omega_a \sqrt{\frac{\hbar\omega_a}{4\pi\varepsilon_0\bar{n}_a c}}\,\hat{a}^\dagger_{a,\eta_a}(\omega_a) \\ &\times \mathbf{e}^*_{a,\eta_a}(r,\theta,\omega_a)\exp\left(i[\beta_{a,\eta_a}(\omega_a)z-\omega_a t]\right), \quad a=s,i, \end{aligned} \tag{3.13}$$

where $\bar{n}_a$ stands for an effective refractive index of field a. The creation operators $\hat{a}^\dagger_{a,\eta_a}(\omega_a)$ give a photon into field a with multi-index η_a and frequency ω_a.

Using Eq.(3.10-3.13), the state $|\psi\rangle$ describing a photon pair at the output face of the fiber can be written as a quantum superposition comprising states of all possible eigenmode combinations (η_s,η_i):

$$\begin{aligned}|\psi\rangle &= -\frac{i}{c}\sum_{\eta_s,\eta_i}\sum_{\eta_p} A_{p,\eta_p}\int d\omega_s \int d\omega_i \sqrt{\frac{\omega_s\omega_i}{\bar{n}_s\bar{n}_i}}\mathcal{E}_p(\omega_s+\omega_i) \\ &\times I_{\eta_p,\eta_s\eta_i}(\omega_s,\omega_i)\hat{a}^\dagger_{s,\eta_s}(\omega_s)\hat{a}^\dagger_{i,\eta_i}(\omega_i)|\text{vac}\rangle. \end{aligned} \tag{3.14}$$

Function $I_{\eta_p,\eta_s\eta_i}(\omega_s,\omega_i)$ quantifies the strength of interaction among the indicated modes at the given signal and idler frequencies,

$$\begin{aligned}I_{\eta_p,\eta_s\eta_i}(\omega_s,\omega_i) &= \int_{S_\perp} r dr d\theta \int_{-L}^{0} dz\,\chi^{(2)}(z)\exp[i\Delta\beta_{\eta_p,\eta_s\eta_i}(\omega_s,\omega_i)z]; \\ &: \mathbf{e}_{p,\eta_p}(r,\theta,\omega_s+\omega_i)\mathbf{e}^*_{s,\eta_s}(r,\theta,\omega_s)\mathbf{e}^*_{i,\eta_i}(r,\theta,\omega_i) \end{aligned} \tag{3.15}$$

$\Delta\beta_{\eta_p,\eta_s\eta_i}(\omega_s,\omega_i)\equiv\beta_{p,\eta_p}(\omega_s+\omega_i)-\beta_{s,\eta_s}(\omega_s)-\beta_{i,\eta_i}(\omega_i)$ characterizes phase-mismatch (PM) of the nonlinear interaction among individual modes.

Using the state $|\psi\rangle$ in Eq. (3.14), a signal photon-number density $n_{\eta_s}(\omega_s)$ observed in mode η_s is computed along the formula

$$n_{\eta_s}(\omega_s) = \sum_{\eta_i}\int d\omega_i \langle\psi|\hat{a}^\dagger_{s,\eta_s}(\omega_s)\hat{a}^\dagger_{i,\eta_i}(\omega_i)\hat{a}_{s,\eta_s}(\omega_s)\hat{a}_{i,\eta_i}(\omega_i)|\psi\rangle. \tag{3.16}$$

3.3.2 Numerical Results

In the analysis, we consider an SiO_2 fiber with a ring-shaped core created by doping the base material with 19.3 mol% of GeO_2 (for details, see [152]). The SPDC process is pumped by a monochromatic beam of wavelength $\lambda_{p0}=0.775$ μm that effectively couples the power of 1 W into the fiber. The fiber was designed such that photon pairs are emitted around the wavelength 1.550 μm used in fiber communication systems. A right-handed circularly polarized $\text{HE}^p_{21,R}$ mode with OAM number $l=1$ (for the nomenclature, see [150])

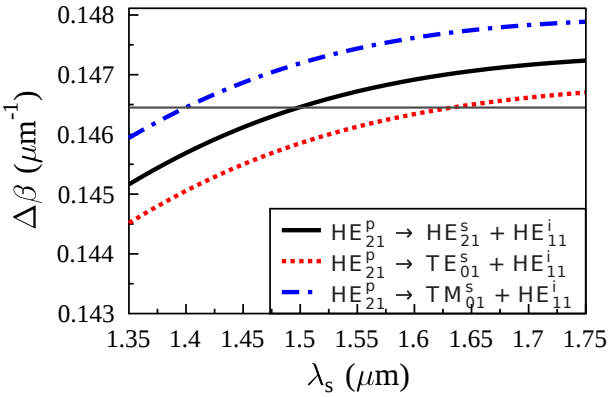

Figure 3.6: Phase mismatch $\Delta\beta_{\eta_p,\eta_s\eta_i}$ as it depends on signal wavelength λ_s for three different combinations of eigenmodes fulfilling the OAM selection rule. The horizontal grey line indicates the maximum of spatial spectrum of $\chi^{(2)}$ modulation expressed in $-\Delta\beta$. The period of modulation $\Lambda = 42.9$ μm is chosen such that perfect PM occurs for $\lambda_{s0} = 1.5$ μm and process $\mathrm{HE}^{\mathrm{p}}_{21,\mathrm{R}} \rightarrow \mathrm{HE}^{\mathrm{s}}_{21,\mathrm{R}}, +\mathrm{HE}^{\mathrm{i}}_{11,\mathrm{R}}$.

has been found suitable for the pump beam. It gives minimal crosstalk with other pump modes (namely TM_{01}) at the given wavelength. It also belongs, together with modes TE_{01} and TM_{01}, to the group of the most stable guided modes. The generated signal and idler photons fulfil the energy conservation law ($\omega_p = \omega_s + \omega_i$) and also the selection rule for OAM numbers ($l_{\eta_p} = l_{\eta_s} + l_{\eta_i}$) that originates in the radial symmetry of the nonlinear interaction. Under these conditions, efficient photon-pair generation has been found for a signal photon in mode $\mathrm{HE}^{s}_{21,R}$ ($l_s = 1$) and an idler photon in mode $\mathrm{HE}^{i}_{11,R}$ or $\mathrm{HE}^{i}_{11,L}$ ($l_i = 0$) which represent the right- and left-handed polarization variants of the same spatial mode. As the phase-matching curves in Fig.3.6 show, also other efficient combinations of signal and idler modes are possible, namely $\mathrm{HE}_{21,R} \rightarrow \mathrm{TE}^{s}_{01} + \mathrm{HE}^{i}_{11}$ and $\mathrm{HE}_{21,R} \rightarrow \mathrm{TM}^{s}_{01} + \mathrm{HE}^{i}_{11}$.

However, quasi-phase-matching reached via the periodic modulation of $\chi^{(2)}$ nonlinearity allows to separate different processes. The right choice of period Λ of $\chi^{(2)}$ nonlinearity tunes the desired process that is exclusively selected provided that the $\chi^{(2)}$ spatial spectrum is sufficiently narrow. For our fiber, the $\chi^{(2)}$ spatial spectrum has to be narrower than 1×10^{-3} $\mu\mathrm{m}^{-1}$. This is achieved in general for fibers longer than 1 cm. The analyzed fiber 1 m long with the width of spatial spectrum equal to 7.6×10^{-6} $\mu\mathrm{m}^{-1}$ allows to separate the desired process from the other ones with the precision better than 1:100.

According to Fig. 3.7 the greatest values of signal photon-number density n_{s,η_s} occur for mode $\mathrm{HE}^{s}_{21,R}$ with an OAM number $l = +1$ around the wavelength $\lambda_s = 1.5$ μm. The full width at the half of maximum of the peak equals $\Delta\lambda_s = 0.96$ nm. The second largest

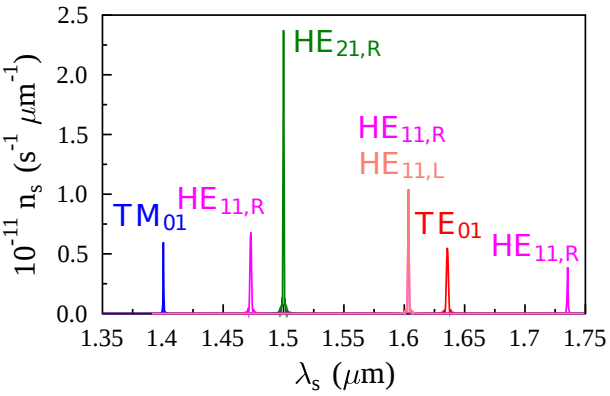

Figure 3.7: Signal photon-number density n_{η_s} as a function of signal wavelength λ_s for a 1 m-long fiber with period $\Lambda = 42.9$ μm. Different modes recognized in the signal field are indicated.

contribution belongs to the processes involving modes $\mathrm{HE}^s_{11,R}$ and $\mathrm{HE}^s_{11,L}$ that interact with mode $\mathrm{HE}_{21,R}$. They build a common peak found at the wavelength $\lambda_s = 1.603$ μm. In signal photon-number density n_{s,η_s}, there also exits two peaks of mode $\mathrm{HE}^s_{11,R}$ that form pairs with the peaks created by modes TM_{01} and TE_{01}. These peaks are shifted towards lower and larger wavelengths, respectively, due to their propagation constants. Whereas the peak belonging to mode TM^s_{01} occurs at the lower wavelength $\lambda = 1.4$ μm, the peak given by mode TE^s_{01} is located at the longer wavelength $\lambda = 1.635$ μm. Spectral shifts of these peaks allow their efficient separation by frequency filtering. The generated photon-pair field is then left in the state with a signal photon in mode $\mathrm{HE}^s_{21,R}$ and an idler photon either in state $\mathrm{HE}^i_{11,R}$ or $\mathrm{HE}^i_{11,L}$. The weights of both possible idler states $\mathrm{HE}^i_{11,R}$ and $\mathrm{HE}^i_{11,L}$ in quantum superposition are the same which gives a linear polarization of the overall idler field. The fiber 1 m long provides around 240 photon pairs per 1 s and 1 μW of pumping in these modes. Strong spectral correlations between the signal and idler frequencies result in fast temporal correlations between the signal and idler detection times occurring in the time window 7 ps long. We note that the analysed process can also be considered in its left-handed polarization variant, in which the pump beam propagates as a $\mathrm{HE}_{21,L}$ mode.

Quasi-phase matching allows also other efficient combinations of modes. For example, the pump beam in mode $\mathrm{HE}_{11,R}$ (or $\mathrm{HE}_{11,L}$) with $l_p = 0$ provides spectrally broad-band SPDC that may give photon pairs with temporal correlations at fs time-scale. Also photon pairs entangled in OAM numbers can be obtained in this configuration. We note that vortex fibers [120] are also suitable for SPDC as they provide similar conditions for photon-pair generation as the analyzed ring fibers. Moreover, their additional core gives better

stability to the modes participating in the nonlinear interaction. Both ring and vortex fibers thus have a large potential to serve as versatile fiber sources of photon pairs in OAM states useful both in metrology and quantum communications.

Summary of this Section

In Section 3.2, we have presented a new way to increase significantly the amount of two-photon spatial entanglement generated in SPDC by means of the use of chirped quasi-phase-matching nonlinear crystals. This opens the door to the generation of high entanglement under various experimental conditions, such as different crystal lengths and sizes of the pump beam. QPM engineering can also be an enabling tool to generate truly massive spatial entanglement, with state of the art QPM technologies [130] potentially allowing to reach entropies of entanglement of tens of ebits. Therefore, the promise of reaching extremely high degrees of entanglement, offered by the use of the spatial degree of freedom, can be fulfilled with the scheme put forward here. The experimental tools required are available nowadays. The use of extremely high degrees of spatial entanglement, as consider here, would demand the implementation of high aperture optical systems. For instance, for a spatial bandwidth of $\Delta\mathbf{p} \sim 2\mu m^{-1}$, the aperture required for $\lambda_p = 400$ nm is $\Delta\theta \sim 4^\circ - 6^\circ$.

In Section 3.3, a ring fiber with thermally induced $\chi^{(2)}$ nonlinearity and periodical poling has been presented as a promising source of photon pairs being in eigenmodes of orbital angular momentum. Spontaneous parametric down-conversion is pumped by a beam with nonzero orbital angular momentum that has been transferred into one of the down-converted beams. Several mutually competing nonlinear processes exploiting different modes occur in the fiber simultaneously. However, they can be spectrally separated. Other configurations also allow for the emission of spectrally broad-band photon pairs as well as photon pairs entangled in orbital-angular-momentum numbers. This makes the analyzed ring fiber useful for many integrated fiber-based applications.

Publications related to the content of this Section

The main results presented in this chapter have been published in the following papers:

J. Svozilík, J. Peřina Jr., and J. P. Torres, Phys. Rev. A 86, 052318 (2012).
D. Javůrek, J. Svozilík, and J. Peřina Jr., submitted to Opt. Lett.

Chapter 4

Anderson Localization of partially coherent light and Quantum Random Walk of Photons with tunable decoherence

4.1 Introduction

More than fifty years ago, P. W. Anderson described in a seminal paper [153] how diffusion in the process of electron transport in a disordered (*random*) semiconductor lattice can be arrested, leading to the localization of the wavefunction in a small region of space, the so-called *Anderson localization*. This unique phenomena has been observed in a myriad of physical systems [154], including electron gas [155], matter-waves (atoms) [156–158] and acoustic waves [159]. The observation of transverse localization of light in a photonic system was predicted by De Raedt et al. [160], considering the similarities existing between the Schrodinger equation and Maxwell equations. This led to the observation of Anderson localization in photonic systems [161–164] in various scenarios.

The underlying physical principles that lead to Anderson localization are also responsible for changes on the spreading of the wavefunction in a quantum random walk (QRW, see Appendix B), which since its first description have become a fundamental paradigm in quantum science [165, 166]. The idea of QRWs was originally conceived by Aharonov *et al.* [167] as an extension of the well-known classical random walk (CRW) [168]. The main distinguishing feature of a QRW, compare to a CRW, is the possibility of interference

between the multiple paths that can be simultaneously traversed by a quantum walker, enabling thus a faster spreading of the uncertainty of location of the walker than in the classical case [169, 170].

The temporal evolution of a quantum system, such as a QRW, depends on the presence, and specific characteristics, of the environmental effects (decoherence) which can modify it [171]. In most cases, the influence of decoherence during the evolution of a quantum walker transforms an originally pure state into a mixed state, lowering the uncertainty about the location of the walker as it propagates. In the limiting case, when all cross-interference terms between different lattice sites are completely erased, the state of pure diffusive classical propagation is reached [170].

QRWs have been theoretically explored for the case of one-dimensional lattices [169, 172], and experimentally implemented by means of different physical platforms, such as photon-based systems [163, 173–177], optical lattices [178] and waveguide arrays [179]. Also, QRWs have been implemented using trapped ions [180] and nuclear magnetic resonance systems [181]. In a sense, generalizations of quantum protocols such as the Shor's factorization algorithm [182] and the Groover's searching algorithm [183] can also be analyzed in similar terms, since they can be viewed as quantum random walks. The consequences of introducing static disorder in a quantum random walk (leading to Anderson localization) has been studied, for example, for one dimensional [184–186] and two-dimensional [187] systems.

In Section 4.2 we describe a versatile and highly-scalable experimental setup for the realization of discrete two-dimensional quantum random walks with a single-qubit coin and tunable degree of decoherence. The proposed scheme makes use of a small number of simple optical components arranged in a multi-path Mach-Zehnder-like configuration, where a weak coherent state is injected. Environmental effects (decoherence) are generated by a spatial light modulator, which introduces pure dephasing in the transverse spatial plane, perpendicular to the direction of propagation of the light beam. By controlling the characteristics of this dephasing, one can explore a great variety of scenarios of quantum random walks: pure quantum evolution (ballistic spread), fast fluctuating environment leading to a diffusive classical random walk, and static disorder resulting in the observation of Anderson localization.

In Section 4.3, we propose an experimental configuration to observe transverse Anderson localization of partially coherent light beams with a tunable degree of first-order coherence. The scheme utilizes entangled photons propagating in disordered waveguide arrays, and is based on the unique relationship between the degree of entanglement of a pair of photons and the coherence properties of the individual photons constituting the

pair. The scheme can be readily implemented with current waveguide-on-a-chip technology, and surprisingly, the tunability of the coherence properties of the individual photons is done at the measurement stage, without resorting changes of the light source itself.

4.2 Implementation of a Spatial Two-Dimensional Quantum Random Walk with Tunable Decoherence

Although the implementation of one-dimensional QRWs has showed to be useful when describing several quantum information systems, there is a great interest in expanding the concept to multidimensional lattices. Along these lines, two-dimensional QRWs provide a powerful tool for modeling complex quantum information and energy transport systems [188, 189]. Notwithstanding, their realization represents a challenge because of the need of a four-level coin operation [187, 190, 191]. One way to overcome this drawback is to make use of different degrees of freedom of photons, such as polarization and orbital angular momentum, as it has been shown in [189]. Another approach is to mimic the two-dimensional QRWs evolution by performing two subsequent one-dimensional QRWs [192, 193].

Here, we make use of the latter approach to put forward an experimental setup for the realization of two-dimensional QRWs. We include the environmental effects (decoherence) as pure dephasing by means of the introduction of random phase patterns, generated by a spatial light modulator (SLM), which can be different from site to site (*spatial disorder*). By controlling the degree of decoherence, we study the transition from the quantum ballistic spreading to the diffusive classical walk. Also, by adding static disorder, we show the possibility of observing Anderson localization [153]. Importantly, our proposal provides a versatile, highly-scalable experimental setup, which may be used as a tool for understanding quantum processes whose underlying physics can be somehow traced to the concept of random walks, such as energy transport in photosynthetic light-harvesting complexes [194, 195] and material band gap structures [196].

4.2.1 A two-dimensional quantum random walk with dephasing

A typical discrete quantum random walk comprises two operations: a coin-tossing operation and a shift operation (see Appendix B). Here, the coin-tossing operation is performed in the Hilbert space $\mathcal{H}_p$ spanned by vectors $\{|H\rangle, |V\rangle\}$, corresponding to the photon polarization. The random walk is performed in the Hilbert space $\mathcal{H}_X \otimes \mathcal{H}_Y$, corresponding to the position of the photon in the transverse plane, spanned by vectors $\{|i, j\rangle\}$ (i, j in-

tegers), which indicate sites (i, j) in the transverse plane $(i, j = ... - 2, -1, 0, 1, 2...)$. The global quantum system thus evolve in the Hilbert space

$$\mathcal{H} = \mathcal{H}_X \otimes \mathcal{H}_Y \otimes \mathcal{H}_p. \tag{4.1}$$

The state of the system is described by the density matrix $\hat{\rho}^{(n)}$, which is transformed to a new density matrix each step n via the CP map

$$\hat{\rho}^{(n+1)} = \hat{P}^{(n)} \hat{S}_Y \hat{H} \hat{S}_X \hat{H} \hat{\rho}^{(n)} \hat{H}^\dagger \hat{S}_X^\dagger \hat{H}^\dagger \hat{S}_Y^\dagger \hat{P}^{(n)\dagger}. \tag{4.2}$$

$\hat{H}$ denotes the Hadamard operator

$$\hat{H} = \frac{1}{\sqrt{2}} \begin{pmatrix} 1 & 1 \\ 1 & -1 \end{pmatrix}, \tag{4.3}$$

which acts on the polarization degree of freedom. The operators $\hat{S}_X$ and $\hat{S}_Y$, which describe the walker's shift n the transverse dimensions x and y, independently, read as

$$\hat{S}_X = \sum_{i,j} |i-1, j, H\rangle\langle i, j, H| + |i+1, j, V\rangle\langle i, j, V|, \tag{4.4}$$

and

$$\hat{S}_Y = \sum_{i,j} |i, j-1, H\rangle\langle i, j, H| + |i, j+1, V\rangle\langle i, j, V|. \tag{4.5}$$

The coupling of the quantum walker with the environment is described by pure dephasing [197]. The form of the unitary dephasing operator considered here can be written as

$$\hat{P}^{(n)} = \sum_{ij} e^{-\frac{i}{2}\phi_{ij}^{(n)} \hat{\sigma}_z} |i, j\rangle\langle i, j|, \tag{4.6}$$

where $\phi_{ij}^{(n)}$ is a random phase matrix and $\hat{\sigma_z}$ is the Pauli operator. Inspection of Eq. (4.6) shows that $\phi_{ij}^{(n)}$ represents a newly introduced phase difference between the horizontal and vertical polarizations at each site. Concerning this, we will consider three physically relevant scenarios, that can be easily implemented in the set-up proposed here. In the general case, the phase differences $\phi_{ij}^{(n)}$ are independent random variables, but with the same probability distribution. Moreover, the ensemble of phase differences $\phi_{ij}^{(n)}$ can change from step n to step $n+1$. In the following, we will refer to this case as a QRW influenced by *dynamical spatial disorder*.

The easiest probability distribution that we can consider is an uniform probability

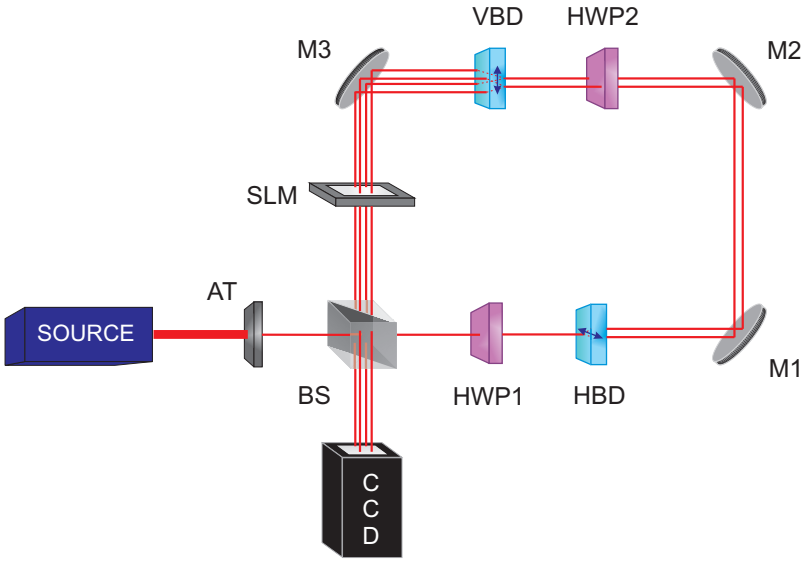

Figure 4.1: General scheme for the implementation of a two-dimensional random walk with decoherence. AT: attenuator; BS: beam splitter; HWP1 and HWP2: half-wave plates that act as coins in the random walk; HBD and VBD: horizontal and vertical beam displacers; M1,M2 and M3: mirrors; SLM: spatial light modulator; CCD: spatial light sensor with single-photon sensitivity.

distribution. If phases can be chosen arbitrarily between the extreme values $-\zeta$ and ζ, there is a constant probability $1/(2\zeta)$ to obtain any phase in this interval. $\zeta = \pi$ is the maximal phase which we can have between the two orthogonal polarizations. $\zeta = 0$ corresponds to the absence of any spatial disorder. If phases do not change during propagation, even though they might differ from site to site, i.e. $\phi_{ij}^{(n)} = \phi_{ij}^{(n+1)}$, then we have *static spatial disorder*. Finally, if all phase differences are the same for all sites, but they can still change from one step to the following, we have *dynamical dephasing without spatial disorder*.

The probability of detecting a photon in the site (i, j) is

$$p^{(n)}(i,j) = \langle i,j|Tr_p[\hat{\rho}^{(n)}]|i,j\rangle, \tag{4.7}$$

where the density matrix that describes the whole system is traced out over the polarization degree of freedom (Tr_p).

The spreading of the uncertainty of photon location is characterized by the dependence of the variance on the step index n

$$V^{(n)} = \sum_{i,j} p^{(n)}(i,j) \left|\mathbf{r}_{ij} - \mu\right|^2 . \tag{4.8}$$

where $\mathbf{r}_{ij} = (i,j)$ represents the lattice site with indexes (i,j) and μ is the mean position, i.e., $\mu = \sum_{i,j} p^{(n)}(i,j)\mathbf{r}_{ij}$.

4.2.2 Proposal of the Experimental Setup

The main building block of the QRW setup is the multi-path Mach-Zehnder-like configuration shown in Fig. 4.1. It allows to make several runs of the QRW without the necessity of using a large amount of optical components, as it is the case, for instance, of the experiment described in [174]. A similar scheme, based on a single-path Mach-Zehnder-like configuration has been used [163, 175]. However in these cases, the walker moves in time, whereas in our proposal the walker moves in the two-dimensional transverse plane, offering a way to simplify the experimental implementation of the two-dimensional QRW.

As source of photons one can use a highly attenuated short coherent pulse, prepared by the combination of a photon source and attenuator (AT), generating the initial state

$$|\Psi^{(0)}\rangle = |0,0\rangle \otimes \frac{1}{\sqrt{2}} \left(|H\rangle + i|V\rangle\right), \tag{4.9}$$

where $(0,0)$ is the central site. The duration of the pulse has to be sufficiently smaller than the time-of-fly through the setup in one cycle. The transverse size of the Gaussian beam profile of the pulse has to be carefully chosen, so that two adjacent sites are not overlapping in the space due to diffraction. For instance, by making use of a Gaussian beam of 2 mm beam waist, corresponding to a Rayleigh range of 23.6 m (for a wavelength $\lambda = 532$ nm), along with typical-sized optical components, we could in principle perform a QRW of approximately more than 20 steps. The number of steps can be further improved by applying smaller beams together with a re-focusing system placed along the walker's path. Alternatively, a spontaneous parametric down-conversion source can be used, provided each down-converted photon is generated in a pure state. Then, the photon is transmitted via the beam splitter (BS) to the system.

To get a clearer picture of the working of the quantum random walk, let us consider in detail the quantum state of the photon in its first passage through the system. First, the polarization state of the photon is changed by the half-wave plate (HWP1) to $\frac{1}{2}|0,0\rangle \otimes [(1+i)|H\rangle + (1-i)|V\rangle]$, i.e., the Hadamard ($\hat{H}$) operation is applied. After this transformation, the photon is displaced by the horizontal beam displacer (HBD) along

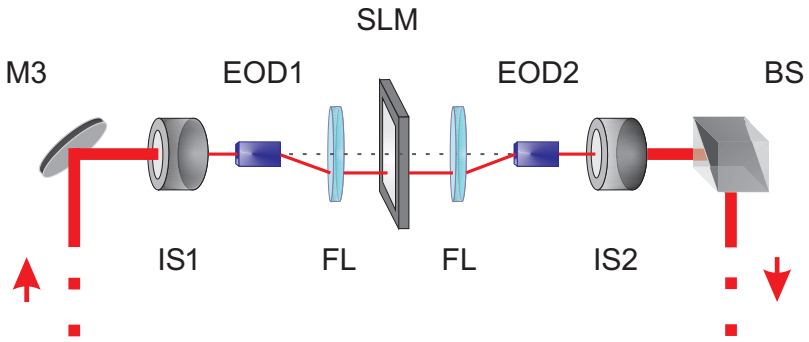

Figure 4.2: Detail of the SLM part of the setup allowing to generate dynamical spatial disorder. M3: mirror; EOD1 and EOD2: electro-optic deflectors; FL: Fourier lens; SLM: spatial light modulator; BS: beam splitter; IS1 and IS2: imaging systems

the x axis according to its polarization, as described by the shift operator $\hat{S}_X$. The photon is now in the state $\frac{1}{2}\left[(1+i)|-1,0,H\rangle+(1-i)|1,0,V\rangle\right]$. A second half-wave plate (HWP2) implements a new Hadamard transformation, which transforms the quantum state to $\frac{1}{\sqrt{8}}\{(1+i)\left(|-1,0,H\rangle+|-1,0,V\rangle\right)+(1-i)\left(|1,0,H\rangle-|1,0,V\rangle\right)\}$. The vertical beam displacer (VBD) shifts the position of the photon along the y axis. After this, the quantum state of the photon reads:

$$\begin{aligned}|\Psi^{(1)}\rangle \;=\; & \frac{1}{\sqrt{8}}\left[(1+i)\left(|-1,-1,H\rangle+|-1,1,V\rangle\right)\right.\\ & \left.+(1-i)\left(|1,-1,H\rangle-|1,1,V\rangle\right)\right].\end{aligned} \tag{4.10}$$

The spatial light modulator (SLM) is used to introduce random phases, given by the phase-matrix $\phi_{ij}^{(n)}$. After the photon passes through the SLM, the whole cycle is repeated with high probability. If not, the photon escapes through the other output port of the beam-splitter, which directs it towards a highly sensitive (single-photon sensitivity) intensified CCD camera with integrated photo-multipliers, which allows to spatially resolve a weak signal with a high efficiency ($\sim$90%) [198]. Moreover, losses in the setup can be compensated by an increase of the amplitude of pulse. The size of whole array of beams can be reduced by an auxiliary imaging system in order to fit on the limited size of sensitive area of CCD.

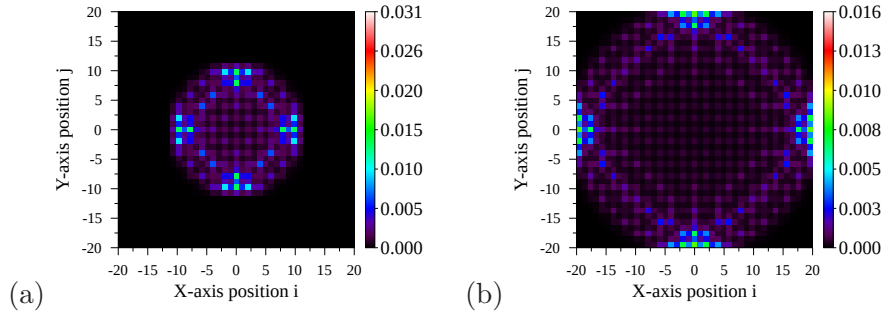

Figure 4.3: Probability distribution function $p^{(n)}(i,j)$, corresponding to the position of the photon, for a two-dimensional quantum random walk with no dephasing after (a) 10 steps and (b) 20 steps.

Fast exchange of phase matrices

A typical SLM has a response time in the order of tens of ms, which means that it is too slow for a fast phase-mask exchange. For this reason, the transmission SLM shown in Fig. 1 has to be supplemented by additional components as it is shown in Fig. 4.2, which allows us to effectively generate the dynamical spatial disorder and dynamical dephasing without spatial disorder for a limited amount of steps. The time of exchange of phase matrices can be done now in tens of ps [199, 200], which is three-orders faster than it is indeed necessary in our experimental proposal, with a typical time of flight of the pulse in the order of ns. The scheme in Fig. Fig.4.2 operates in the following manner. At the beginning, the size of the whole array of beams is reduced by an imaging system (IS1) to fit into the electro-optical deflector (EOD1). The EOD1, together with a Fourier lens (FL), serve to address different regions of the SLM along either the vertical or horizontal direction, which realize then the random phase-matrices $\phi_{ij}^{(n)}$ in all steps. Just changing the directions of deflection of the array, both types of dynamical disorders can be simulated. The EOD2 (and another FL) then serve to return all beams back to the original direction of propagation, so that all beams remain in the same position in the traverse plane at all time.

4.2.3 Quantum random walk

Let us consider first the case when the SLM does not introduce any phase shift ($\phi_{ij}^{(n)} = 0$ for all (i,j)). This corresponds to the case $\zeta = 0$. Figure 4.2.2 shows the probability distribution function $p^{(n)}(i,j)$ for (a) $n = 10$ and (b) $n = 20$ steps. In both cases, the

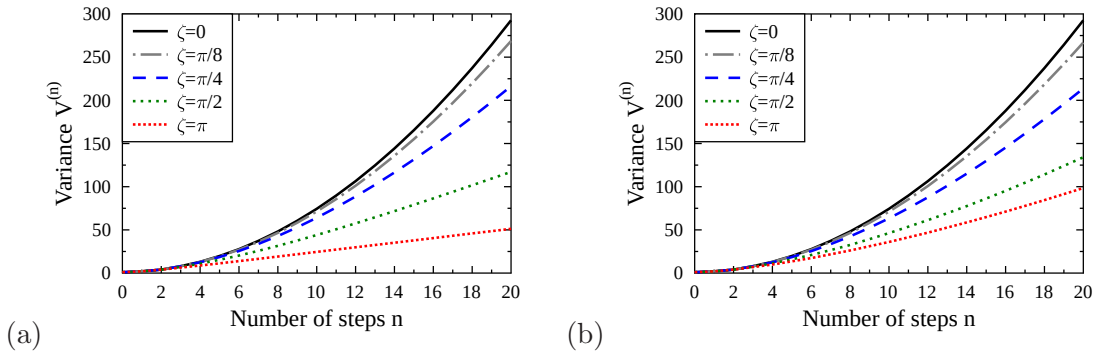

Figure 4.4: Spreading of the position of the photon ($V^{(n)}$) as a function of the number of steps for several values of ζ and different types of dephasing. a) Dynamical spatial disorder. b) Dynamic dephasing without spatial disorder. The results are obtained averaging over 500 different realizations of the matrix $\phi_{ij}^{(n)}$.

distribution shows a symmetrical shape around the lines $x = 0$ and $y = 0$, with four groups of peaks located along the x and y axes. The resulting symmetry comes from the specific initial quantum state chosen in Eq. (4.9). When the number of steps is increased, the peaks move further away from the central site $(0, 0)$. The shapes obtained in Fig.4.2.2 correspond to the probability distributions of a two-dimensional Grover walk [188, 192]. The walker propagates with ballistic speed, characterized by a quadratic dependence of the variance $V^{(n)}$ with the step index, i.e., $V^{(n)} \approx n^2$. This case is shown in Figs. 4.4(a) and (b), corresponding to the case with $\zeta = 0$.

4.2.4 Quantum Random Walk Affected by Dephasing

The dephasing effect introduced by the SLM allows to induce a transition from the quantum to the classical random walk via two mechanisms. First, as shown in Fig.4.4(a), by means of dynamical spatial disorder. The phase-matrix $\phi_{ij}^{(n)}$ shows independent and randomly chosen values for each site, and it is refreshed each step. The case $\zeta = 0$ corresponds to the QRW with no dephasing. Increasing the amount of disorder, characterized by a corresponding increase of the parameter ζ, reduce the spreading of $V^{(n)}$ as can be seen in Fig.Fig.4.4(a). In the limiting case, which is reached for $\zeta = \pi$, the observed dependence ($\sim n$) of variance $V^{(n)}$ is a direct indication of the transition to the classical regime of random walks.

The classical limit can also be reached by means of dynamical dephasing without spatial disorder, as it is shown in Fig.Fig.4.4(b). The reduction of the uncertainty of the

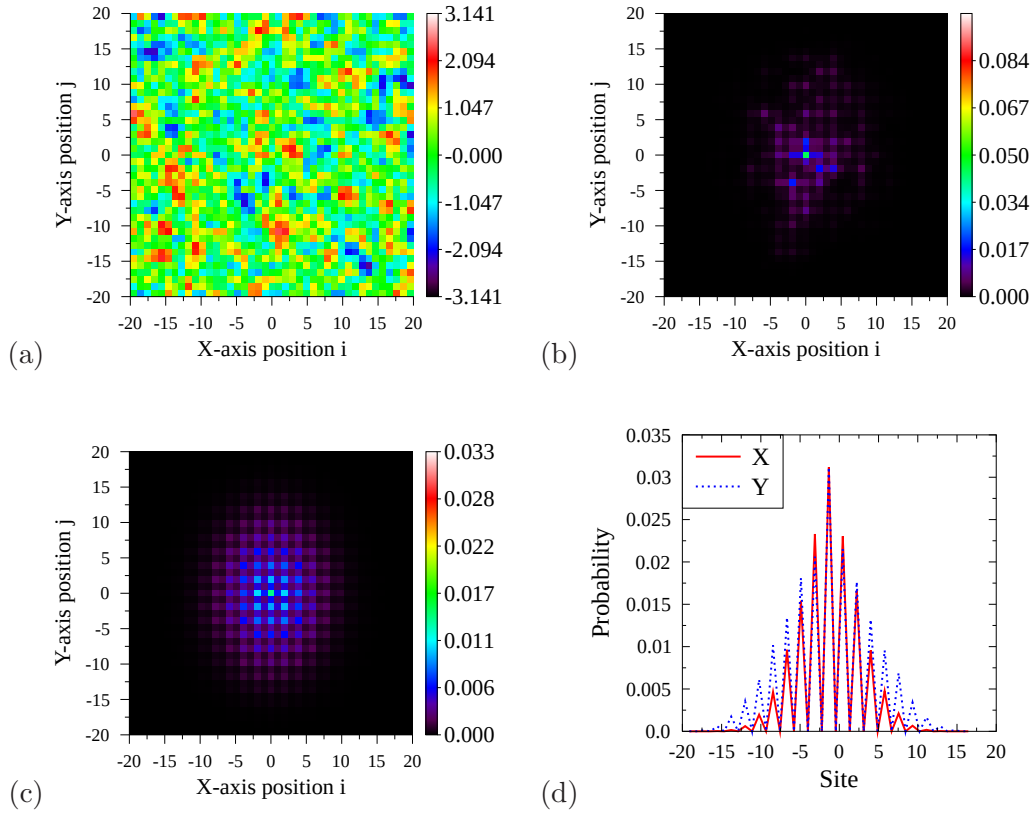

Figure 4.5: Observation of the spatial Anderson localization. (a) Example of a matrix $\phi_{ij}^{(n)}$ for $\zeta = \pi$ that leads to the Anderson localization. (b) Corresponding probability distribution $p^{(n)}(i,j)$ after 20 steps. (c) Averaged probability distribution over 500 realizations. (d) Cuts of the data shown in Fig. 5(c) along the X and Y axes passing the site (0,0).

photon position is less dramatic than in the case with dynamical spatial disorder. For the dynamical spatial disorder, $V^{(n)} \sim 51.25$ for $\zeta = \pi$ after 20 steps. On the contrary, for dynamical dephasing without spatial disorder, we have $V^{(n)} \sim 98.45$ under the same conditions. Indeed, the n-dependence of the typical deviation, characteristic of the classical regime, it is not yet reached after 20 steps, as is readily observed in Fig.Fig.4.4(b).

4.2.5 Anderson Localization

In the context of our discussion, the Anderson localization is the reduction of spreading of the uncertainty of the photon position [153]. We will demonstrate that this effect can also be observed in the set-up considered here. In [162], Anderson localization was observed

in the transverse plane of a light beam passing through a crystal with random static fluctuations of the index of refraction. Since the randomness in the index of refraction is affecting only the phase of the propagating beam, it is possible to imitate these phase-fluctuations with a SLM, under the consideration of static spatial disorder, since Anderson localization does not appear with dynamical spatial disorder.

In Fig.4.2.4(a) we present a typical profile of the phase-matrix $\phi_{ij}^{(n)}$, independent of n, which leads to beam localization. Fig.4.2.4(b) shows the corresponding probability distribution of the photon position for this specific phase profile. Notice that it contains a strong peak located in the middle of the lattice. The presence of Anderson localization is confirmed in Fig.4.2.4(c), where we show the averaged probability distribution function for $\zeta = \pi$, exhibiting an exponential suppression of probabilities for sites distant from the center. For the sake of clarity, we also plotted in Fig.4.2.4(d) two cuts of the averaged probability distribution along the X and Y axes, to highlight this feature.

4.3 Measurement-Based Tailoring of Anderson Localization of Partially Coherent light

In most cases, as in the previous section, the input state in a quantum random walk is chosen to be fully coherent. Since Anderson localization is a consequence of interference effects, one can dare thinking that an initial coherent state is thus necessary to observe Anderson localization. However, Čapata et al. [201] have shown that even a partially coherent input light beam can lead to Anderson localization in a disordered waveguide array (WGA). Partially coherent beams can be described as a superposition of orthogonal coherent modes, where the modal coefficients are random variables that are uncorrelated with one another [202, 203]. Therefore, according to [201], since spreading of each mode, being a coherent mode, can be arrested in a random medium with static disorder, the whole partially coherent beam should also suffer localization in a similar way to a fully coherent beam.

Here we propose an experimental scheme which could lead to the observation of Anderson localization of partially coherent beams with a tunable degree of first-order coherence. The approach is based on two basic ingredients. On the one hand, a single-photon in a pure quantum state (Von Neumann entropy $E = 0$) is arguably the most simple example of a photonic state which shows first-order coherence [204]. Mixed single-photon quantum states do not show first-order coherence. On the other hand, the degree of entanglement of a pure two-photon state (photons A and B) is directly related to the purity of the

quantum state of the photon A (B), which results from tracing out all degrees of freedom corresponding to photon B (A). The Von Neumann entropy of the quantum state that describes photon A (B) could be used as a measure of the degree of entanglement of the paired photons.

Consequently, the manipulation of the degree of entanglement of the two-photon state can effectively tailor the first-order coherence of the signal (idler) photon [205], generating a one-photon quantum state which is mixed, and thus partially coherent. Anderson localization (*co-localization*) of entangled photon fields in disordered waveguides has been presented in [206, 207]. However, in that case the goal was to look for Anderson localization of the two photons that form the entangled pair, while here entanglement is a tool to tailor the degree of coherence of one of the subsystems (photon A or photon B) which form the entangled pair.

4.3.1 Proposed Experimental Scheme

In general, the quantum description of a pure entangled two-photon state (photons A and B) writes

$$|\Psi\rangle = \int dp \int dq\, \Psi(p,q)\hat{a}_A^\dagger(p)\hat{a}_B^\dagger(q)|0\rangle \tag{4.11}$$

where p and q represent the transverse wavevectors of photons A and B, respectively, $\hat{a}_A^\dagger(p)$ and $\hat{a}_A^\dagger(q)$ creation operators of photons in modes A and B and $\Psi(p,q)$ is the mode function that describes the properties of the biphoton [88]. For monochromatic fields, the positive-frequency electric-field operators are expressed as

$$\hat{E}_A^{(+)}(x) \sim \int dp\, \hat{a}_A(p) \exp\left(ipx\right), \tag{4.12}$$

$$\hat{E}_B^{(+)}(y) \sim \int dq\, \hat{a}_B(q) \exp\left(iqy\right). \tag{4.13}$$

We note that temporal dependence of the electric-field operators has been omitted for the sake of simplicity. Defining $\Psi(x,y) = \int dp \int dq\, \Psi(p,q) \exp(-ipx - iqy)$, the normalized pure entangled two-photon state given by Eq.(4.11) can be written as

$$|\Psi\rangle = \int dx \int dy\, \Psi\left(x,y\right) |x\rangle_A |y\rangle_B, \tag{4.14}$$

where we have defined $|x\rangle_A \equiv \hat{E}_A^{(-)}\left(x\right)|0\rangle_A$ and $|y\rangle_B \equiv \hat{E}_B^{(-)}\left(y\right)|0\rangle_B$. Notice that the two-photon amplitude $\Psi(x,y)$ corresponds to the second-order correlation function $\Psi(x,y) = {}_A\langle 0|_B\langle 0|\hat{E}_B^{(+)}(y)\hat{E}_A^{(+)}(x)\rangle$.

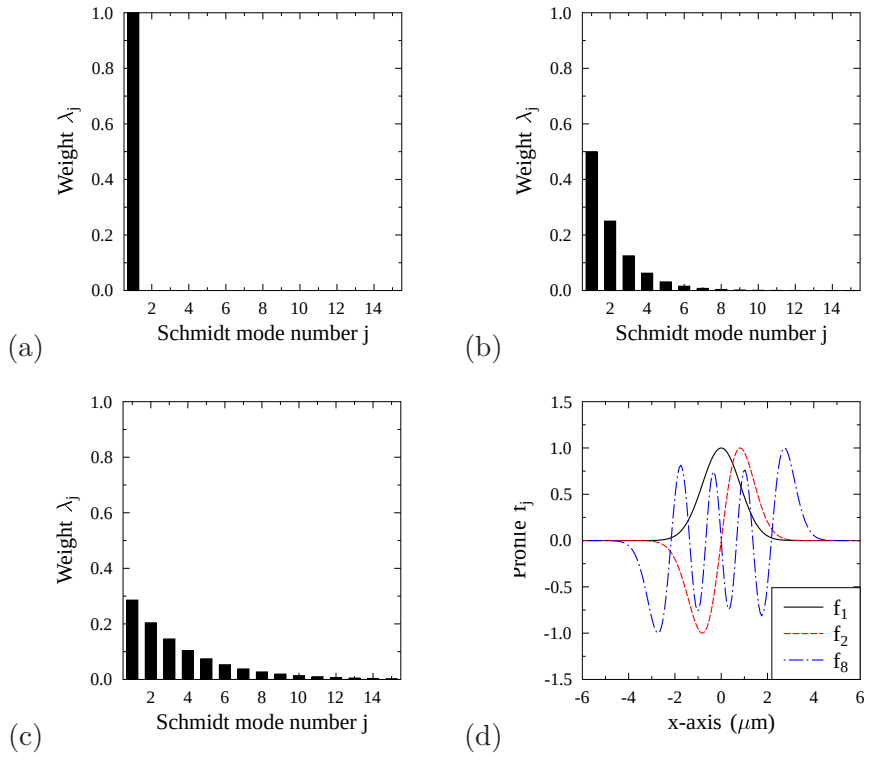

Figure 4.6: Schmidt mode decomposition. Here we show the first 15 Schmidt modes of the Schmidt decomposition for three cases: a) a separable state with $\gamma_0 = 0.5$, (b) an entangled state with $\gamma_0 = 1.5$ and (c) an entangled state with $\gamma_0 = 3$. The shape of some selected Schmidt modes (see the legend) are plotted in (d) for $\gamma_0 = 1.5$. In all cases $\sigma_0 = 1\ \mu m$.

The two-photon amplitude Ψ can be described by a Schmidt decomposition (defined in the Subsection 1.1.1) of the form

$$\Psi(x,y) = \sum_{j=1}^{N} \sqrt{\lambda_j} f_j(x)\, g_j(y) \tag{4.15}$$

λ_j are the Schmidt eigenvalues and $\{f_j\}$ and $\{g_j\}$ are the Schmidt modes corresponding to photons A and B. For the sake of simplicity, the two-photon amplitude $\Psi(x,y)$ is approximated by the Gaussian function

$$\Psi(x,y) \sim \exp\left[-\alpha\,(x+y)^2 - \beta\,(x-y)^2\right]. \tag{4.16}$$

In this case, the Schmidt modes correspond to Hermite functions of order j [208, 209].

Some representative cases are shown in Fig.4.6(d).

The parameters characterizing the spatial correlations between photons A and B, α and β, can be expressed using more suitable parameters that describe characteristics of photon A: its rms beam width (σ_0) and the beam width-spatial bandwidth product (γ_0), here denoted as incoherence,

$$\alpha = \frac{1}{4\sigma_0^2}\left(2\gamma_0^2 \pm \gamma_0\sqrt{4\gamma_0^2-1}\right), \tag{4.17}$$

$$\beta = \frac{1}{4\sigma_0^2}\left(2\gamma_0^2 \mp \gamma_0\sqrt{4\gamma_0^2-1}\right). \tag{4.18}$$

The derivation of Eq.(4.17) and Eq.(4.18) is included in the Appendix C.1. In general, $\gamma_0 \geq 0.5$ and is related to the Schmidt number, $K = 2\gamma_0$, which is a measure of the size of the mode distribution involved in Eq.(4.15). This number K is defined by Eq.(1.8). For $\alpha = \beta$, there is not entanglement between photons A and B, the Schmidt decomposition contains a single mode (see Fig.4.6(a)) and γ_0 attains its minimum value, i.e., $\gamma_0 = 0.5$. This case yields a pure and first-order coherent photon. In all other cases, the spectrum of the Schmidt decomposition contains several modes. Fig.4.6(b) shows the weight of the first 15 Schmidt modes (eigenvalues λ_j) for $\gamma_0 = 1.5$ and Fig.4.6(c) for $\gamma_0 = 3$.

The key point of our scheme is the presence of a detection scheme that projects the photon B into a restricted set of modes before detection, being a particular case the projection into a single Schmidt mode g_j. In this way, the number of modes that describe the quantum state of photon A after detection of photon B would be correspondingly reduced. Importantly, the first-order coherence of photon A depends on the number of modes onto which the photon B is projected. Projection of photon B into a specific single mode renders effectively photon A into a first-order coherent photon. On the contrary, detection of photon B into an increasing number of modes results into a partially coherent signal photon with a decreasing degree of coherence. Therefore, this can thus be appropriately called tailoring of the first-order coherence by heralding detection.

By tailoring the first-order coherence of a single photon, we also tailor the characteristics of the Anderson localization. The projection and detection of photon B into a finite number M of modes is represented by the quantum operator $\hat{Y}_B = \sum_{j=1}^{M} |g_j\rangle_B\langle g_j|_B$ with $|g_j\rangle = \int dy g_j(y)|y\rangle_B$. After detection, the *truncated* quantum state of photon A reads as

$$\hat{\rho}_A = \mathrm{Tr}_B\left[|\Psi\rangle\langle\Psi|\hat{Y}_B\right] = \sum_{j=1}^{min(N,M)} \lambda_j |f_j\rangle_A\langle f_j|_A \tag{4.19}$$

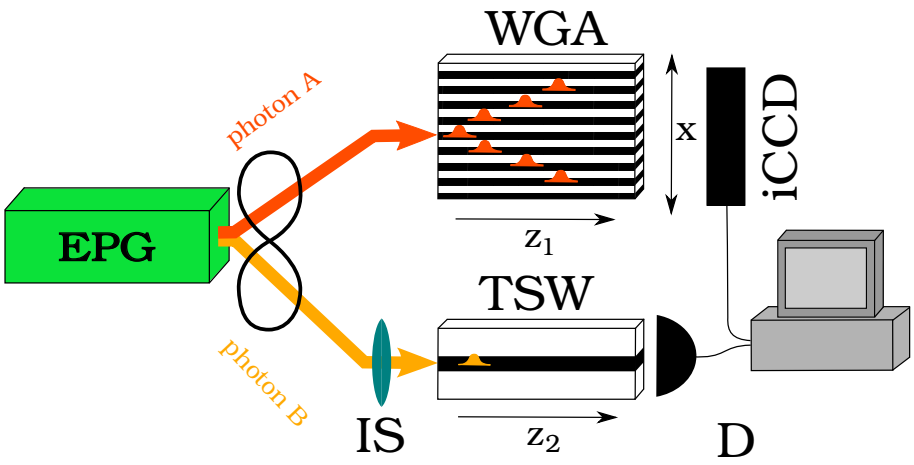

Figure 4.7: Sketch of the experimental configuration proposed to observe Anderson localization of partially coherent photons in a disordered waveguide array (WGA). The three-slab waveguide (TSW) allows propagation of different numbers of guided modes depending on its core size. EPG: The Entangled-photons generator is the source of photon pairs; iCCD: intensified CCD; D: single-photon detector; IS: Imaging System.

corresponding to an incoherent superposition of $min\,(N, M)$ modes with weights λ_j.

A sketch of the experimental configuration considered is shown in Fig.4.7. A pair of entangled photons (A and B) is generated. Photon A is injected into a one-dimensional waveguide array (WGA) with refractive index profile $n_A(x)$. The waveguide array contains 101 layers of semiconductor material $Al_xGa_{1-x}As$ with the index of reflection taken from [90]. The whole structure is created by alternating two different layers: $Al_{0.3}Ga_{0.7}As$ and $Al_{0.8}Ga_{0.2}As$ of the same thickness 0.6 μm. The disorder is induced by randomizing the index of refraction of each layer, etc. $n_A(x) = n_A^0(x) + \Delta n_A(x)$. The probability distribution of the random disturbances $\Delta n_A(x)$ is described by a Gaussian function characterized by its typical standard deviation δ.

On the other hand, the photon B can propagate in different three-slab waveguide (TSW) with refractive index profile $n_B(y)$, and different sizes of the core of the waveguide. The material of the core is $Al_{0.3}Ga_{0.7}As$ and two surrounding layers are made of $Al_{0.8}Ga_{0.2}As$. The layers surrounding the core are considered to be infinite in their thickness. The number of guided modes supported depends on the core size [see Fig.4.8(a)], so the three-slab waveguide effectively selects a certain amount of modes of photon B, effectively tailoring the first-order coherence of photon A. A three-slab waveguide has been chosen for simplicity, and because its suitability for integration on a chip altogether with the WGA.

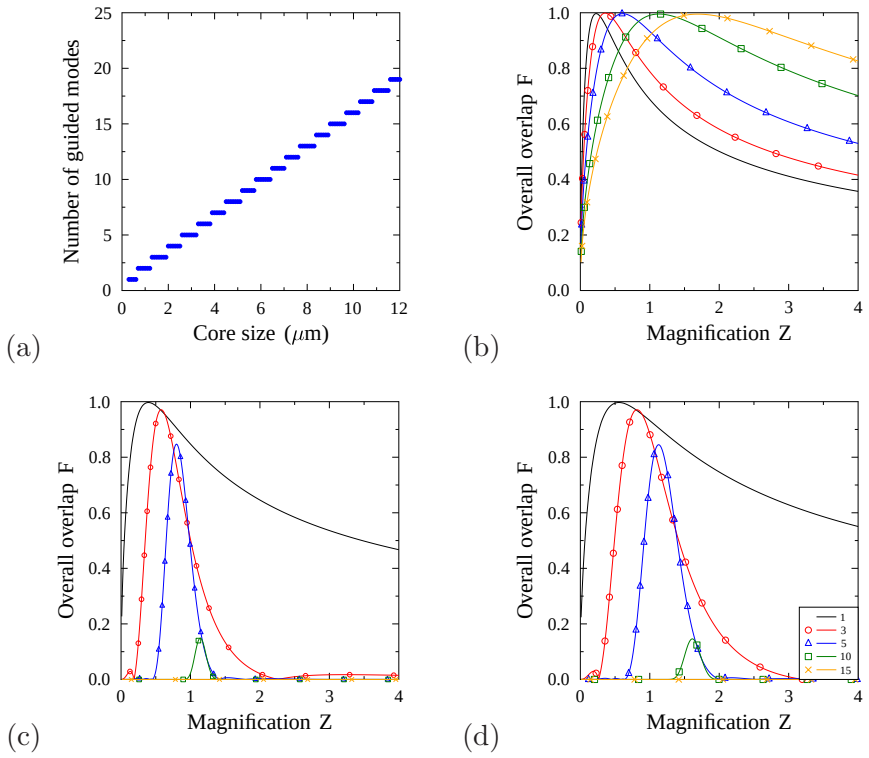

Figure 4.8: (a) Number of guided modes supported by the three-slab waveguide (TSW) as a function of the core size of the waveguide. (b), (c) and (d) show the overall spatial overlap factor between Schmidt modes $\{g_j\}$ and guided modes of the three-slab waveguide $\{v_j\}$, as given by the product $F = \prod_j |d_{jj}|$, as a function of the magnification factor Z of the imaging system. Three different cases, with different value of γ_0, are considered. (b) $\gamma_0 = 0.5$, (c) $\gamma_0 = 1.5$ and (d) $\gamma_0 = 3$. In all cases $\sigma_0 = 1\ \mu m$. The five curves in each plot correspond to five different three-slab waveguides supporting various amount of modes, as given by the legend in (d).

The evolution of the spatial shape of photons A and B, in the waveguide array and the three-slab waveguide, respectively, can be conveniently described by means of the guided modes supported by each waveguide, $\{u_i(x)\}$ for the WGA and $\{v_j(y)\}$ for the TSW [210]. The guided modes are obtained as solutions of the Helmholtz equations

$$\Delta u_i(x) + \left[n_A^2(x)k_0^2 - \kappa_i^2\right] u_i(x) = 0, \tag{4.20}$$

$$\Delta v_j(y) + \left[n_B^2(y)k_0^2 - \mu_j^2\right] v_j(y) = 0, \tag{4.21}$$

where κ_i and μ_j are the corresponding propagation constants. The index of refraction is considered to be homogeneous along the direction of propagation (along the z-axis in

both waveguides). Equation (4.20) has been solved using the finite element method [211] whereas Eq.(4.21) has been solved by the semi-analytical method [150]. The polarization of photons A and B is transverse electric (TE), i.e. parallel to the surface boundary between layers, and their wavelengths are 1550 nm, far below the bang-gap of the material. Therefore absorption can be omitted in our model. Moreover, the propagation distance z_1 of photon A has been restricted to 0.5 mm in order to prevent reaching the reflective boundaries of WGA.

The coupling of the input photons, characterized by the Schmidt modes f_n and g_m, to the corresponding waveguides, characterized by modes u_i and v_j, is expressed via the coupling coefficients

$$c_{ni} = \int dx f_n(x) u_i^*(x), \tag{4.22}$$

$$d_{mj} = \int dy g_m(y) v_j^*(y). \tag{4.23}$$

Using coefficients c_{ni} and d_{mj} the quantum state of two photons after their propagation at distances z_1 and z_2 in the two waveguides is

$$|\Psi\rangle = \sum_n \sqrt{\lambda_n} \sum_{ij} c_{ni} d_{n_j} \exp\left(i\kappa_i z_1 + i\mu_j z_2\right) |u_i\rangle_A |v_j\rangle_B, \tag{4.24}$$

where $|u_i\rangle_A \equiv \int dx u_i(x)|x\rangle_A$ and $|v_j\rangle_B \equiv \int dy v_j(y)|y\rangle_B$. We can write $z_1 = z_2 = z$ without losing generality.

Detection of photon B after projection via a three-slab waveguide is represented by the operator $\hat{Y}_B = \sum_{i=j}^{n_{max}} |v_j\rangle_B \langle v_j|_B$, where n_{max} refers to the limited amount of guided modes present in the specific three-slab waveguide considered. For fixed values of γ_0 and σ_0, the spatial profile of photon B is the same, but the spatial profiles of the guided modes $\{v_j\}$ differ in their sizes for waveguides with different core size. Modes of the Schmidt decomposition $\{g_j(y)\}$ and guide modes in the TSW $\{v_j(y)\}$ can be ordered by its mode order ($j = 1, 2, ...$), with modes with the same order having similar spatial shapes. In order to maximize the spatial overlap between the Schmidt modes and the guided modes, we include an imaging system (IS) designed to maximize the overall spatial overlap factor $F = \prod_j |d_{jj}|$. Fig. 4.8(b), (c) and (d) show the overall spatial overlap factor as a function of the magnification factor (Z) of the imaging system for five different three-slab waveguides which support 1, 3, 5, 10 and 15 guided modes, respectively. For instance, for $\sigma_0 = 1\mu$m and $\gamma_0 = 3$, the optimum magnification factors are 0.55, 0.82, 1.13, 1.61 and 2.03.

On the contrary, since we are interested in the Anderson localization of photon A after

propagation in the disordered waveguide array, the spatial profile of photon A is detected by an intensified coupled-charge detector (iCCD), which allows to detect electromagnetic signals at the single photon level. Detection of a photon in each pixel of the iCCD is represented via the photon-number operator $\hat{n}_A(x) = \hat{E}_A^{(-)}(x)\,\hat{E}_A^{(+)}(x)$. After detection of photon B, the spatial shape of the photon A at distance z in the WGA is described by the photon-number spatial distribution

$$p_A(x) = Tr_A\left[\hat{\rho}_A \hat{n}_A(x)\right] = \sum_{m,n} \sqrt{\lambda_m \lambda_n} I(m,n) \times \sum_{i,j} c_{mi} c_{nj}^* \exp\left\{iz\left(\kappa_i - \kappa_j\right)\right\} u_i(x)\, u_j^*(x), \tag{4.25}$$

where $I(m,n) = \sum_j d_{mj} d_{nj}^*$. The width of photon A can be characterized by its effective beam width

$$w_{eff} = \left\langle \frac{\left[\int dx p_A(x)\right]^2}{\int dx p_A^2(x)} \right\rangle, \tag{4.26}$$

where $\langle\rangle$ refer to averaging over an ensemble of random realizations of a disordered WGA.

In order to analyze the results presented in the next section, it is important to take into account that the beam size σ_0 and the incoherence γ_0 of photon A, defined in Eqs.(4.17) and (4.18), corresponds to values before projection and detection of photon B. Therefore, after filtering mediated by the spatial mode projection of photon B using the TSW, the first-order correlation function of photon A at the input of WGA writes

$$G_A^{(1)}(x,x') = \sum_{m,n} \sqrt{\lambda_n \lambda_m} I(m,n)\, f_n(x)\, f_m^*\left(x'\right). \tag{4.27}$$

One can obtain the values of σ and γ for photon A via equations Eq.(C.5), Eq.(C.8) and Eq. (C.9) in the Appendix C.1.

If photon B propagates in a TSW that supports a single propagating mode, the size of photon A will corresponds to the size of that single mode, independently of the value of σ_0. When other modes are added via an increase of the guiding capability of TSW, the beam size σ reaches its initial value σ_0, as it is shown in Fig.4.9(a) for a photon with $\sigma_0 = 1\mu$m.

A similar behavior of the value of γ is also shown in Fig. 4.9(b), where a strong dependence on the effectiveness of the coupling to the TSW is observed. When coupling to a single mode, $\gamma = 0.5$, independently of the value of γ_0. When the number of propagating modes in TSW is enlarged, the value of γ, even though is smaller than γ_0, also converges

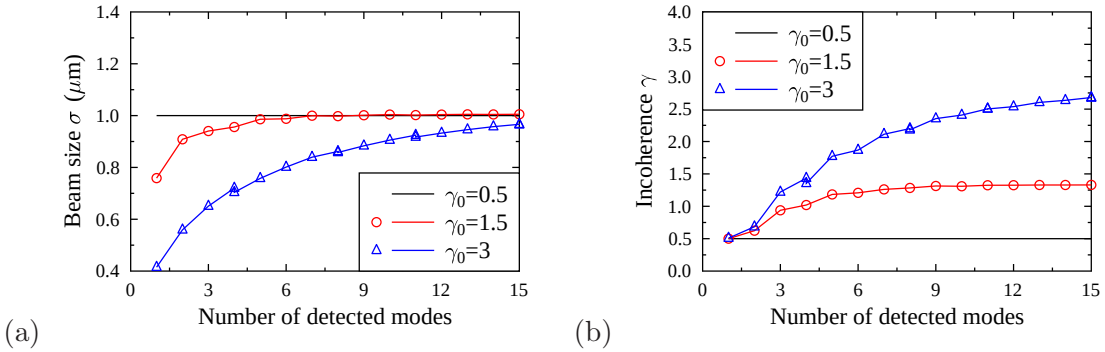

Figure 4.9: (a) Beam size σ and (b) Incoherence γ of photon A when photon B propagate in different TSWs, and afterwards is detected. Each TSW is designed to support a different number of guided modes, as indicated in the axis. We consider three different two-photon states (see legend in (b)), characterized by $\gamma_0 = 0.5$, $\gamma_0 = 1$ and $\gamma_0 = 3$. In all cases, $\sigma_0 = 1\,\mu m$.

to γ_0, since now propagation in the waveguide does not effectively filter the input state.

4.3.2 Results

For the sake of comparison, we first consider a separable two-photon state ($K = 1$), so the Schmidt decomposition contains a single mode, as shown in Fig.4.6(a). Photon A is in a first-order coherent state, and since there is no entanglement, there is also no dependence on the characteristics of the propagation of photon A on photon B being projected and detected. As expected, when no disorder is considered ($\delta = 0$), the photon A diffracts the least in comparison to other cases considered in Figs.4.10(c) and (e), which corresponds to entangled paired photons. When disorder is introduced ($\delta = 0.02$), photon A turns out to be localized, with the size of the output probability distribution being almost equal to the input probability. Anderson localization is the result of the coupling of photon A to localized guided modes of the disordered WGA $\{u_i(x)\}$.

We now consider two examples with two-photon entangled states with $\gamma_0 = 1.5$ and $\gamma_0 = 3$. This corresponds to two-photon states with Schmidt number $K = 3$ and $K = 6$, and entropy of entanglement $E = 2$ and $E = 3.021$. The Schmidt decompositions are shown in Fig.4.6(b) and (c). Unlike the coherent case (γ_0=0.5), the size of photon A depends on the amount of propagating modes of the TSW used. This phenomena is more visible with the ordered WGA, as shown in Fig.4.10(c) and (e). Note that each Hermite function $\{f_i\}$ for $i > 1$ contains high spatial components that spread even faster than the narrow Gaussian profile given by f_1, but in the overall, they might have a smaller impact

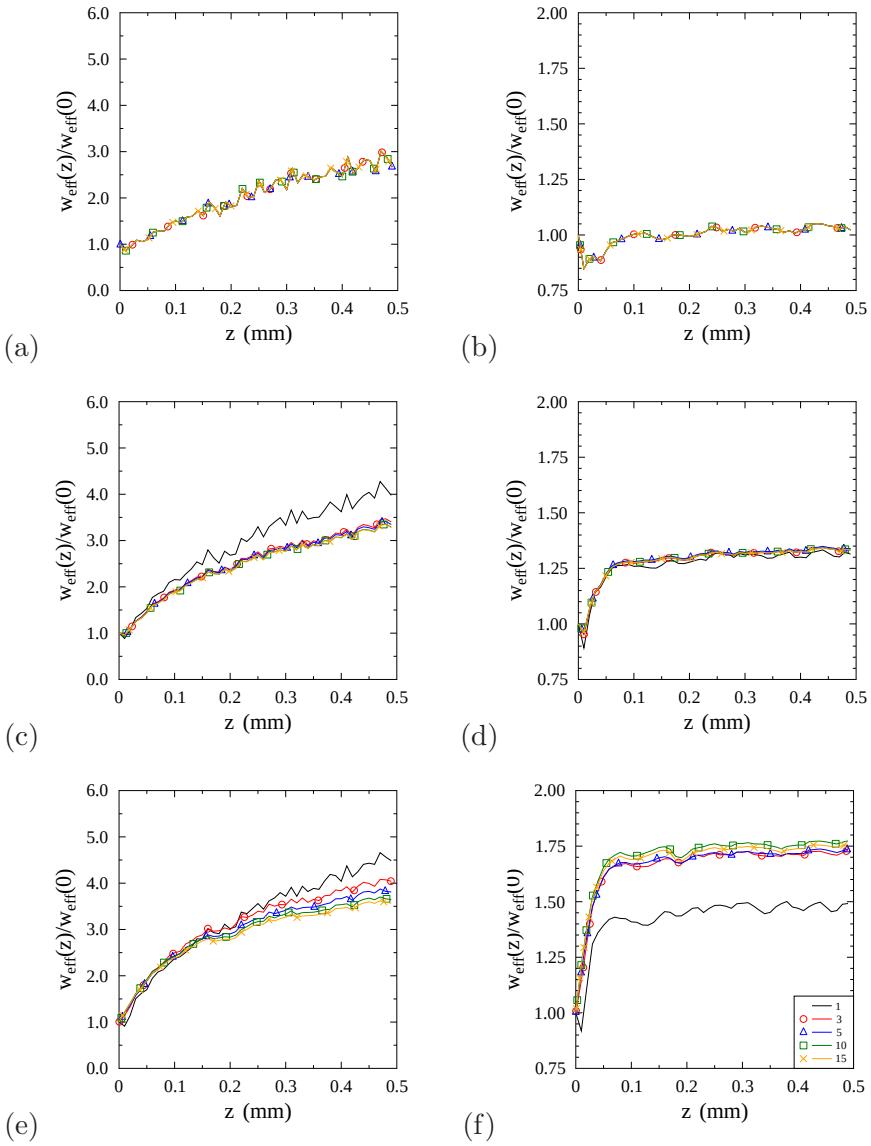

Figure 4.10: Spreading of the size of photon A after propagation in the WGA, as given by the ratio $w_{eff}(z)/w_{eff}(0)$. Photons A and B are part of a two-photon state with three different values of the amount of entanglement, but with the same value of $\sigma_0 = 1\ \mu m$. (a) and (b) correspond to a non-entangled two-photon state with $\gamma_0 = 0.5$ (K=1). (c) and (d) corresponds to an entangled state with $\gamma_0 = 1.5$ (K=3), while for (e) and (f) we have $\gamma_0 = 3$ (K=6). (a),(c) and (e) correspond to the propagation of photon A in a non-disordered WGA, while (b),(d) and (f) corresponds to the propagation of photon A in a disordered WGA with $\sigma = 0.02$. We present averaged results obtained over 100 different realizations of WGA. The curves in all plots represent propagation of photon B in different TSW which support distinct amounts of guided modes, as shown in the legend in (f). This legend is valid for all plots.

on the final size of photon A due to decreasing weights λ_j for a given state.

For a disordered WGA with $\delta = 0.02$ the effect of the partially coherent nature of photon A values on its propagation of is more visible, as seen in Fig.4.10(d) and (f). The lower the degree of coherence, the broader is the output effective width of the spatially localized photon A. Moreover, Hermite functions $\{f_i\}$ with increasing order localize with a higher ratio $w_{eff}(L)/w_{eff}(0)$ than the fundamental Hermite function f_1. Our calculations also predict a noticeable dependence of the amount of localization expected, shown in Fig.4.10, on important experimental values such as the magnification factor of the imaging system or the effectiveness of the coupling to the TSW. Therefore, if one would use a different optimization function F for the imaging system, differences in Fig.4.10(d) and (f) could be more visible.

Summary of this Section

We have shown in Section 4.2 a new, highly scalable and easily implemented experimental configuration to observe spatial two-dimensional random walks under a great variety of circumstances, by means of the implementation of two consecutive one-dimensional random walks. The proposal makes use of only a small amount of simple optics components, and allows us to simulate many different quantum systems and protocols based on the quantum random walk concept. Additionally, by carefully controlling the amount and type of disorder present in the system, we have shown the effects of different environmental effects: dynamical spatial disorder, dynamical dephasing without spatial disorder and static spatial disorder. The last case drove us to the observation of Anderson localization. The control of environmental effects is paramount importance in nearly all quantum systems. In some cases, it is even crucial to understand the dynamics experimentally observe.

In Section 4.3, we have presented an experimental scheme for the observation of transverse Anderson localization of partially coherent light with a tunable degree of coherence. The degree of coherence is tuned by injecting one photon of a fully coherent two-photon entangled state in a waveguide with a finite and controllable amount of propagating modes. The system can be integrated on a semiconductor chip, since both the disordered waveguide array (WGA) and the three-slab waveguide TSW considered were designed with this goal in mind. Therefore our proposal is experimentally feasible taking into an account nowadays mature semiconductor technologies.

Publications related to the content of this Section

The main results presented in this chapter have been published in the following papers:

J. Svozilík, R. de J. Leon-Montiel, and J. P. Torres, Phys. Rev. A **86**, 052327 (2012).
J. Svozilík, J. Peřina Jr. , and J. P. Torres, Phys. Rev. A **89**, 053808 (2014).

Conclusions

On the one hand, this thesis has been devoted to the investigation of new sources of quantum entanglement of photons, and also to the design of new sources that can produce paired photons lacking entanglement. We have considered both bulk crystals and waveguides. On the other hand, we have considered new applications based on the presence of entanglement between pairs of photons. For instance, how to use entanglement to generate a source of light with a tunable first-order coherence.

In this thesis, more specifically:

- We have shown that the Spontaneous Parametric Down Conversion in Brag Reflection Waveguides can be used as a highly versatile source of entangled, as well as non-entangled, paired photons. Precisely, we have designed and analyzed new waveguide structures:

    1. That can generate paired photons that lack any frequency correlations between them (a separable quantum states) without decreasing the length of a waveguide or requiring a strong filtering of emitted photons. The photons can be made spectrally indistinguishable, if necessary. [Section 2.2]
    2. That can generate polarization-entangled photon pairs, for its use in multi-frequency QKD networks, with an enormous bandwidth ($\sim$ 160 nm for a type II configuration!!). [Section 2.3]

- We have demonstrated that polarization-entangled paired photons generated in a semiconductor Bragg reflection waveguide clearly violate the CHSH inequality, so it can be considered an expedient source of high-quality polarization-entangled two-photon states. [Section 2.4]

- We have presented a new way how to increase significantly the amount of two-photon spatial entanglement (massive spatial entanglement) generated via SPDC by

means of the use of state of the art chirped quasi-phase-matching nonlinear crystals. [Section 3.2]

- We have demonstrated a novel method of SPDC generation of entangled photon pairs in the OAM degree of freedom based on the periodically poled silica fibers with a thermally induced non-linearity. [Section 3.3]

- We have shown a new, highly scalable and easily implementable experimental configuration to observe the spatial two-dimensional random walks under a great variety of circumstances, which allow to simulate many different quantum systems and protocols based on the quantum random walk concept, under the presence of diverse environmental effects: dynamical spatial disorder, dynamical dephasing without spatial disorder and static spatial disorder. The last case drove us to the observation of Anderson localization. [Section 4.2]

- We have proposed an experimental scheme for the observation of transverse Anderson localization of partially coherent light with a tunable degree of coherence. The degree of coherence is tuned by injecting one photon of a fully coherent two-photon entangled state into waveguides with a different finite amount of supported guided modes. Our proposal is experimentally feasible taking into an account nowadays mature semiconductor technologies. [Section 4.3]

It is also worthy to mention, that the evolution of communication systems and computing tools in our world seems to be unstoppable. There will be always a pushing force for higher transmitting rates, more complex computation tasks and higher securities of communication channels. Where classical technologies might be touching theirs performance boundaries, the quantum world can offer further enhancement to step over these classical limits. One of the most distinguishing and peculiar feature of the quantum world is entanglement, that not only has profound theoretical implications for our understanding of Nature, but it can also provide some possible practical applications in a not-so-distant future.

Appendices

Appendix A

Searching for all Guided Modes in Waveguides

The search for all non-radiative guided modes that can propagate in a waveguide represents a mathematical challenge in many occasions. We describe here three different methods for obtaining these modes under various circumstances. All methods considered here share the consideration of longitudinal homogeneity of waveguides that significantly reduces the complexity of the calculation. The first two methods are dedicated to the analysis of BRWs. The transfer matrix method is the simplest one and offers a deep physical insight into the functionality of Bragg reflectors. The other method used to analyze BRW is a numerical method based on the finite element method in a scalar formulation, which can be applied for 1D or 2D BRWs with a simple rectangular structure. The last method considered in this appendix describes a procedure for solving the Helmholtz equation for ring fibres.

A.1 Transfer Matrix Approach

The simplest case of a periodically stratified media, composed of two layers of thickness t_1 and t_2 that alternate with a period $\Lambda = t_1 + t_2$, has been mathematically analysed by Yeh and his co-workers [212, 213]. We only mention the most important results that are essential for BRWs. As it can be found in [212], the refractive index profile along the y-axis for the simplest structure can be expressed as

$$n(y) = \begin{cases} n_2 & n\Lambda < y < n\Lambda + t_2, \\ n_1 & n\Lambda + t_2 < y < (n+1)\Lambda, \end{cases} \tag{A.1}$$

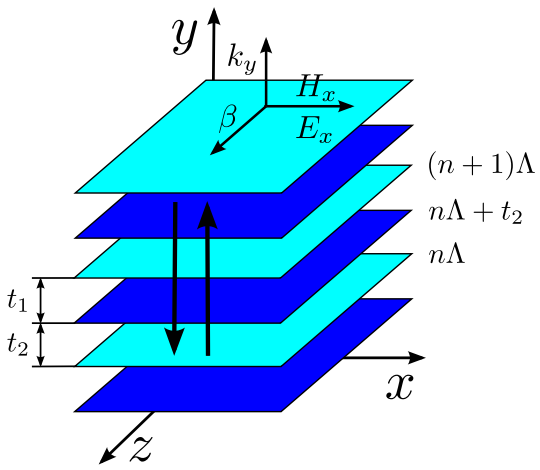

Figure A.1: Stratified medium with two alternating layers representing a Bragg reflector.

where n_1 and n_2 are refraction indices of layers, as shown in Fig.A.1. According to the orientation of **E** and **H** with respect to the interfaces between layers, we can distinguish two polarizations - the traverse electric field (TE), where only non-zero components are E_x, H_y and H_z, and the traverse magnetic field (TM), with non-vanishing components H_x, E_y and E_z. For a description of propagation is sufficient only to take into account E_x (H_x), because other components are related to them by the Maxwell equations. The continuity requirements on the layers interfaces lead to differences in the form of fields transformation relations. A field propagating along the z-axis, with the propagation constant β, can be written as $E(y,z) = E(y)\, e^{i\beta.z}$, where $E(y)$ is the traverse profile of the TE field. The electric field in each layer can be expressed as a sum of two counter-propagating waves. The expression for the first layer in a single period n is

$$E(y,z) = \left(a_n.e^{ik_y(x-n\Delta)} + b_n.e^{-ik_y(x-n\Delta)}\right) e^{i\beta z}. \tag{A.2}$$

For the second one, the coefficients only interchange $(a_n, b_n) \leftrightarrow (c_n, d_n)$. Enforcing boundary conditions for TE waves at the interface between layers, one can easily find the transformation matrices between (a_n, b_n) coefficients

$$\begin{pmatrix} a_{n-1} \\ b_{n-1} \end{pmatrix} = \begin{pmatrix} A_{TE} & B_{TE} \\ C_{TE} & D_{TE} \end{pmatrix} \begin{pmatrix} a_n \\ b_n \end{pmatrix}, \tag{A.3}$$

where the matrix elements are:

$$
\begin{aligned}
A_{TE} &= e^{-ik_{1y}t_1}\left[\cos\left(k_{2y}t_2\right) - \frac{i}{2}\left(\frac{k_{2y}}{k_{1y}} + \frac{k_{1y}}{k_{2y}}\right)\sin\left(k_{2y}t_2\right)\right], \\
B_{TE} &= e^{ik_{1y}t_1}\left[-\frac{i}{2}\left(\frac{k_{2y}}{k_{1y}} + \frac{k_{1y}}{k_{2y}}\right)\sin\left(k_{2y}t_2\right)\right], \\
C_{TE} &= e^{-ik_{1y}t_1}\left[\frac{i}{2}\left(\frac{k_{2y}}{k_{1y}} + \frac{k_{1y}}{k_{2y}}\right)\sin\left(k_{2y}t_2\right)\right], \\
D_{TE} &= e^{ik_{1y}t_1}\left[\cos\left(k_{2y}t_2\right) + \frac{i}{2}\left(\frac{k_{2y}}{k_{1y}} + \frac{k_{1y}}{k_{2y}}\right)\sin\left(k_{2y}t_2\right)\right].
\end{aligned} \tag{A.4}
$$

Coefficients of the transfer matrix for the TM wave are equal to

$$
\begin{aligned}
A_{TM} &= e^{-ik_{1y}t_1}\left[\cos\left(k_{2y}t_2\right) - \frac{i}{2}\left(\frac{n_1^2k_{2y}}{n_2^2k_{1y}} + \frac{n_2^2k_{1y}}{n_1^2k_{2y}}\right)\sin\left(k_{2y}t_2\right)\right], \\
B_{TM} &= e^{ik_{1y}t_1}\left[-\frac{i}{2}\left(\frac{n_2^2k_{1y}}{n_1^2k_{2y}} - \frac{n_1^2k_{2y}}{n_2^2k_{1y}}\right)\sin\left(k_{2y}t_2\right)\right], \\
C_{TM} &= e^{-ik_{1y}t_1}\left[\frac{i}{2}\left(\frac{n_2^2k_{1y}}{n_1^2k_{2y}} - \frac{n_1^2k_{2y}}{n_2^2k_{1y}}\right)\sin\left(k_{2y}t_2\right)\right], \\
D_{TM} &= e^{ik_{1y}t_1}\left[\cos\left(k_{2y}t_2\right) + \frac{i}{2}\left(\frac{n_1^2k_{2y}}{n_2^2k_{1y}} + \frac{n_2^2k_{1y}}{n_1^2k_{2y}}\right)\sin\left(k_{2y}t_2\right)\right].
\end{aligned} \tag{A.5}
$$

It is relevant to stress that for $n_2^2k_{1y} = n_1^2k_{2y}$ the Brewster angle is reached and both reflected and incident TM waves are mutually independent.

From solid state theory [214] is well-known that a periodic potential induced by atoms in crystal lattices governs the movement of electrons in the form of Bloch waves. In the same way, fields in a periodic photonic structure, as introduced in Eq.(A.1), exhibit similar behaviour as electrons, when the position is translated by a multiple of period Λ. According to the Floquet theorem, for a wave propagating in a layered media, $E_K(y+\Lambda, z) = e^{iK\Lambda}E_K(y)e^{i\beta z}$, where K is the Bloch wave-number and $E_K(y+\Lambda) = E_K(y)$ is a periodic function. Including this, the transformation (translation) matrix Eq.(A.3) is then equal to the phase-shift $e^{iK\Lambda}$ that is the solution of eigenvalue equation

$$
\begin{pmatrix} A & B \\ C & D \end{pmatrix}\begin{pmatrix} a_n \\ b_d \end{pmatrix} = e^{iK\Lambda}\begin{pmatrix} a_n \\ b_d \end{pmatrix}. \tag{A.6}
$$

In compliance with the Floquet theorem, the exponential function on the right is the eigenvalue of the transformation matrix on the left side. Solving this equation for K allows us to find the relationship of K with β and ω

$$K(\beta,\omega) = \frac{1}{\Delta}\cos^{-1}\left[\frac{1}{2}(A+D)\right]. \tag{A.7}$$

For $|\frac{1}{2}(A+D)| < 1$ the Bloch wave number is a real number and represents a freely propagating wave. On the other hand, for $|\frac{1}{2}(A+D)| > 1$ $K = \frac{m\pi}{\Lambda} + iK_i$, where K_i is the imaginary part of K, Bloch waves are evanescent. For the functionality of BRWs, the most important situation is $|\frac{1}{2}(A+D)| = 1$, because in that situation, the wave-number K lies in the photonic (forbidden) stop-band of the layered structure. In this event, the wave is not propagated, but fully reflected, in a layered medium - that is the underlying principle of BRWs. Modes that are based on this principle are called Bragg modes. The optimal reflection is reached when a wave acquires in each layer $\pi/4$ phase-shift $(t_1.k_{1y} = t_2.k_{2y} = \pi/4)$, which ensures that K lies in the middle of a stop-band. Note that when the Brewster angle is reached for TM waves, the width of these stop-bands shrinks to zero.

Having the basic matrix formalism for layered media in our hand, we proceed with the simplest case of 1D BRWs with the core in the center surrounded by two Bragg reflectors. More details can be found in [215] as only main results are shown here. For the purpose of obtaining the dispersion relation of guided Bragg modes from the Helmholtz equation

$$\Delta\vec{E} + \left[k_0^2 n^2(y) - \beta^2\right]\vec{E} = 0, \tag{A.8}$$

the electromagnetic field is considered to have the form

$$\vec{E}(y,z,t) = \vec{E}(y)e^{(i\beta z - i\omega\cdot t)}. \tag{A.9}$$

The transverse wave-number of guided modes in each layer of the Bragg reflector is equal to

$$k_{iy} = \sqrt{k_0^2 n_i^2 - \beta^2} \quad for\, i = 1,2. \tag{A.10}$$

Firstly, we consider the case of TE mode. For the lowest order Bragg mode, the electric field in the core can be described as

$$E_x(y) = \begin{cases} C_1\cos(k_c.y) & \frac{t_c}{2} \geq |y|, \\ C_2.E_{K,TE}\left(y - \frac{t_c}{2}\right)e^{iK_{TE}\left(y-\frac{t_c}{2}\right)} & \frac{t_c}{2} < |y|. \end{cases} \tag{A.11}$$

where $E_{K,TE}\left(y - \frac{t_c}{2}\right)$ describes Bragg modes in the claddings, originating from the Floquet theorem for the Bloch number K_{TE}. In the Bragg reflector (cladding), we use an expression

introduced earlier for a layered structure [Eq. (A.2)] and express the electric field in the cladding as

$$E_x(y) = \begin{cases} a_n e^{ik_{1y}\left(y-\frac{t_c}{2}-n\Lambda\right)} + b_n e^{-ik_{1y}\left(y-\frac{t_c}{2}-n\Lambda\right)} & n\Lambda \le \left(y-\frac{t_c}{2}\right) \le n\Lambda + t_1, \\ c_n e^{ik_{2y}\left(y-\frac{t_c}{2}-n\Lambda-t_1\right)} + d_n e^{-ik_{2y}\left(y-\frac{t_c}{2}-n\Lambda-t_1\right)} & n\Lambda + t_1 \le \left(y-\frac{t_c}{2}\right) \le (n+1)\Lambda. \end{cases} \tag{A.12}$$

Using the continuity requirements for E_x and H_z $\left(\sim \frac{\partial E_x}{\partial y}\right)$ at the interface between the core and adjacent claddings, the obtained dispersion relation is

$$\frac{1}{k_c}\cot\left(\frac{t_c k_c}{2}\right) = \left(\frac{-i}{k_{1y}}\right)\frac{e^{iK_{TE}\Lambda} - A_{TE} + B_{TE}}{e^{iK_{TE}\Lambda} - A_{TE} - B_{TE}}. \tag{A.13}$$

Secondly, we focus on the TM mode that takes the form

$$H_x(y) = \begin{cases} C_1\cos(k_c.y) & 0 \le y \le \frac{t_c}{2},\ n_1^2 k_{2y} < n_2^2 k_{1y}, \\ C_1\sin(k_c.y) & 0 \le y \le \frac{t_c}{2},\ n_1^2 k_{2y} > n_2^2 k_{1y}, \\ C_2.H_{K,TM}\left(y-\frac{t_c}{2}\right)e^{iK_{TM}\left(y-\frac{t_c}{2}\right)} & \frac{t_c}{2} < y. \end{cases} \tag{A.14}$$

The function $H_{K,TM}(y)$ has the same form of Eq.(A.12) for the Bloch vector K_{TM}. The boundary requirements for H_x and E_z $\left(\sim \frac{\partial H_x}{\partial y}\right)$ lead to following dispersion relations

$$\frac{1}{k_c}\cot\left(\frac{t_c k_c}{2}\right) = \frac{-i}{k_1}\left(\frac{n_1}{n_c}\right)^2\frac{e^{iK_{TM}\Lambda} - A_{TM} + B_{TM}}{e^{iK_{TM}\Lambda} - A_{TM} - B_{TM}} \qquad n_1^2 k_2 < n_2^2 k_1 \tag{A.15}$$

and

$$k_c\cot\left(\frac{t_c k_c}{2}\right) = ik_1\left(\frac{n_c}{n_1}\right)^2\frac{e^{iK_{TM}\Lambda} - A_{TM} - B_{TM}}{e^{iK_{TM}\Lambda} - A_{TM} + B_{TM}} \qquad n_1^2 k_2 > n_2^2 k_1. \tag{A.16}$$

Effective indices of Bragg modes are then obtained from Eq.(A.13), Eq.(A.15) and Eq.(A.16) for given waveguide parameters.

A.2 Numerical Methods Based on Discrete Approximations

Numerical methods based on discrete approximations, such as the finite element method (FEM) or the finite difference method (FDM), allow us directly determine all guided modes of a waveguide. We introduce only the principle of 2D-FEM method based on the Galerkin

approach. As it has been mentioned, waveguides are considered to be homogeneous in the longitudinal direction (along z-axis). Moreover, we assume that the width of the waveguide core (along x-axis) is larger than its thickness (along y-axis), and larger than other layers, then the influence of vertical boundaries can be neglected [151]. These premises simplify our calculation efforts and allow us to use the scalar finite element method (SC-FEM) [211, A13]. The main advantage of this method is a high resistance against spurious (non-physical) eigen-solutions as compared with the finite difference method. Moreover, resulting matrices for the SC-FEM of the generalized eigen-equation are usually smaller and also symmetrical. In the following, we briefly describe one of the FEM method called the Galerkin weighed residual method.

From the Maxwell equations, it is straightforward to derive the following equations for TE and TM guided modes in a 2D waveguide

$$\frac{\partial^2 E_x}{\partial x^2} + \frac{\partial^2 E_x}{\partial y^2} + \left(k_0^2 \epsilon_r - \beta^2\right) E_x = 0, \tag{A.17}$$

$$\frac{1}{\epsilon_r}\left[\frac{\partial^2 H_x}{\partial x^2} + \frac{\partial^2 H_x}{\partial y^2}\right] + \left(k_0^2 - \frac{\beta^2}{\epsilon_r}\right) H_x = 0. \tag{A.18}$$

Since both equations are formally similar, the only difference being caused by different continuity conditions on the boundaries, we only present here the solution of Eq. (A.17). In order to find an approximated solution of Eq. (A.17), the transverse area of the waveguide and surroundings is divided into many small areas (Fig.A.2), alias elements. In each element $e = (i, j)$ $E_x(x, y)$ is approximated by the function $u^e(x, y)$. The weighted residual function r^e is then defined as

$$r^e = \int_{\Omega^e} dS w^e \left[\frac{\partial^2 u^e}{\partial x^2} + \frac{\partial^2 u^e}{\partial y^2} - (\beta^2 - \epsilon_r \cdot k_0^2) u^e\right], \tag{A.19}$$

where the parameter Ω^e is the area of the given element e, with boundary Γ^e, and w^e is the weight function. In each element, the condition $r^e \approx 0$ must be fulfilled.

The shape of each element corresponds to the profile of the waveguide in a such way, that the boundaries of the element must be aligned with the position of the discontinuities of the relative permittivity $\epsilon_r(x, y)$. Since we are interested in a rectangular waveguide, the rectangular shape of elements was selected. The organization of the elements into the grid is illustrated in Fig.(A.2).

In each element, the unknown function u^e is expressed in the form of a summation

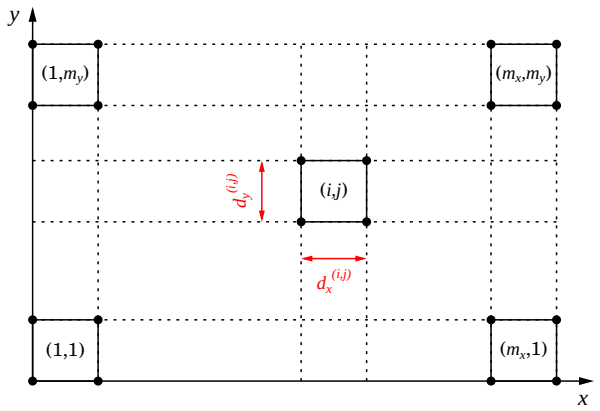

Figure A.2: Shape of the grid used in numerical calculations. Numbers of elements along the x and y axes are denoted as m_x and m_y, respectively; $d_x^{(i,j)}$ and $d_y^{(i,j)}$ mean lengths of an (i,j)-th element. The overall number of used nodes is $M = (m_x + 1)(m_y + 1)$.

$$u^e = \sum_{j=1}^{4} N_j^e u_j^e, \tag{A.20}$$

where $N_j^e(x,y)$ are the Lagrange interpolation polynomials in the given element e. The polynomial N_j^e corresponds to node $j = 1,2,3,4$ with the following form

$$\begin{aligned} N^e(x,y)_1 &= -\frac{x}{d_x^e} - \frac{y}{d_y^e} + \frac{xy}{d_x^e d_y^e} + 1, \\ N^e(x,y)_2 &= \frac{x}{d_x^e} - \frac{xy}{d_x^e d_y^e}, \\ N^e(x,y)_3 &= \frac{xy}{d_x^e d_y^e}, \\ N^e(x,y)_4 &= \frac{y}{d_y^e} - \frac{xy}{d_x^e d_y^e}. \end{aligned} \tag{A.21}$$

According to the formulation of Galerkin's method, the weight function corresponds to the interpolation functions $N_j^e(x,y), j = 1 \ldots 4$, so

$$\int_{\Omega^e} dS N_i^e \sum_{j=1}^{4} \left[\frac{\partial^2 N_j^e}{\partial x^2} + \frac{\partial^2 N_j}{\partial y^2} - (\beta^2 - \epsilon_r \cdot k_0^2) \right] u_j^e = 0. \tag{A.22}$$

Using relations

$$N_i^e \frac{\partial^2 N_j^e}{\partial x^2} = \frac{\partial}{\partial x}\left(N_i^e \frac{\partial N_j^e}{\partial x}\right) - \frac{\partial N_i^e}{\partial x}\frac{\partial N_j^e}{\partial x}, \tag{A.23}$$

$$N_i^e \frac{\partial^2 N_j^e}{\partial y^2} = \frac{\partial}{\partial y}\left(N_i^e \frac{\partial N_j^e}{\partial y}\right) - \frac{\partial N_i^e}{\partial y}\frac{\partial N_j^e}{\partial y}, \tag{A.24}$$

we obtain

$$\int_{\Omega^e} dS \quad \left[\tfrac{\partial}{\partial x}\left(N_i^e \tfrac{\partial N_j^e}{\partial x}\right) - \tfrac{\partial N_i^e}{\partial x}\tfrac{\partial N_j^e}{\partial x} + \tfrac{\partial}{\partial y}\left(N_i^e \tfrac{\partial N_j^e}{\partial y}\right) - \right.$$
$$\left. - \tfrac{\partial N_i^e}{\partial y}\tfrac{\partial N_j^e}{\partial y} - (\beta^2 - \epsilon_r \cdot k_0^2) N_i^e N_j^e \right] u_j^e = 0. \tag{A.25}$$

Equation (A.25) can be now rewritten as

$$\sum_{j=1}^{4} (-R_{ij}^e + G_{ij}^e + T_{ij}^e) u_j^e = \beta^2 \sum_{j=1}^{4} E_{ij}^e u_j^e; \qquad \forall i = 1 \ldots 4. \tag{A.26}$$

where we define the matrices

$$R_{ij}^e = \int_{\Omega^e} dS \left[\frac{\partial N_i(x,y)}{\partial x}\frac{\partial N_j(x,y)}{\partial x} + \frac{\partial N_i(x,y)}{\partial y}\frac{\partial N_j(x,y)}{\partial y}\right], \tag{A.27}$$

$$G_{ij}^e = \int_{\Omega^e} dS \left[\frac{\partial}{\partial x}\left(N_i^e \frac{\partial N_j^e}{\partial x}\right) + \frac{\partial}{\partial y}\left(N_i^e \frac{\partial N_j^e}{\partial y}\right)\right]$$
$$= \oint_{\Gamma^e} d\vec{s} \left[N_i^e \frac{\partial N_j^e}{\partial x}\vec{x} + N_i^e \frac{\partial N_j^e}{\partial y}\vec{y}\right], \tag{A.28}$$

$$T_{ij}^e = k_0^2 \int_{\Omega^e} dS \epsilon_r N_i^e N_j^e, \tag{A.29}$$

$$E_{ij}^e = \int_{\Omega^e} dS N_i^e N_j^e. \tag{A.30}$$

All these components of the matrices are calculated for all nodes in each element. In Eq. (A.28) the Green's theorem was used. The matrix components G_{ij}^e vanish on the internal boundaries between two neighboring elements. On the boundary Γ of the computation area, they are equal to zero according to the assumed Dirichlet condition $u|_{(x,y)\in\Gamma} = 0$.

Next, we can define the matrix K_{ij}^e corresponding to the left side of Eq. (A.26), i.e. $K_{ij}^e = -R_{ij}^e + G_{ij}^e + T_{ij}^e$. Each component of matrices K_{ij}^e and E_{ij}^e describes a correlation

between two nodes in the discreet grid. As a result, we obtain a generalized eigenvalue problem of the form $K\mathbf{u} = \beta^2 E\mathbf{u}$. The vector $\mathbf{u} = (u_1, u_2, \ldots, u_{N_n})$ describes the amplitude of the field in all nodes. By putting $\mathbf{u}$ to Eq. (A.20) the approximated distribution of the electric (magnetic) intensity field in an entire area is recovered.

Typically, it is necessary to use the sparse-matrix representation for large matrices and then to apply the iterative eigen-value solver, such as the Arnoldi algorithm [216]. But that is not necessary in this case, therefore the direct-solver of eiqen-problems from the Intel MKL library can be used.

A.3 Guided Modes in a Ring Fiber

In order to derive hybrid guided modes of a ring fibre[1] presented in Fig.3.5(a),we start with a re-writing the Helmholtz equation from the Cartesian coordinate system to the cylindrical system. This means solving

$$\Delta\mathbf{E} + k_0^2 \epsilon_r(\mathbf{r})\,\mathbf{E} = 0, \tag{A.31}$$

using the Laplacian operator Δ in the cylindrical form

$$\Delta = \frac{\partial^2}{\partial r^2} + \frac{1}{r}\frac{\partial}{\partial r} + \frac{1}{r^2}\frac{\partial^2}{\partial \theta^2} + \frac{\partial^2}{\partial z^2}. \tag{A.32}$$

For the magnetic field $\mathbf{H}$ the equation is similar. Fields $\mathbf{E}$ and $\mathbf{H}$ can be represented solely using longitudinal components along the z-axis [150, 151]. Considering the rotational symmetry of a fiber waveguide, the longitudinal component E_z can be express as

$$E_z(r, \theta, z) = f(r)g(\theta)e^{i\beta z}. \tag{A.33}$$

The expression Eq.(A.33) is the same for H_z. The partial differential equation Eq.(A.31) can be solved employing the variable separation method. The corresponding functions $f(r)$ and $g(\theta)$ describe azimuthal and lateral profiles of the electric (magnetic) field. Inserting Eq.(A.33) to Eq.(A.31), one obtains

$$\frac{r^2}{f(r)}\frac{\partial^2 f(r)}{\partial r^2} + \frac{r}{f(r)}\frac{\partial f(r)}{\partial r} + r^2\left[\epsilon_r(r) - n_{eff}\right]k_0^2 + \frac{1}{g(\theta)}\frac{\partial^2 g(\theta)}{\partial \theta^2} = 0. \tag{A.34}$$

[1] In the previous part of this appendix, solely guided modes (TE,TM) having significant (non-vanishing) one field component were considered. For the ring fibre, we need to abandon this simplification and look for a hybrid modes that poses all field components.

The lateral function $g(\theta)$ is considered to be an oscillating periodical function with the period n, therefore:

$$\frac{1}{g(\theta)}\frac{\partial^2 g(\theta)}{\partial\theta^2} = -n^2 \tag{A.35}$$

and

$$\frac{r^2}{f(r)}\frac{\partial^2 f(r)}{\partial r^2} + \frac{r}{f(r)}\frac{\partial f(r)}{\partial r} + r^2\left[\epsilon_r(r) - n_{eff}\right]k_0^2 = n^2. \tag{A.36}$$

Solutions of Eq.(A.35) are equal to:

$$g(\theta) = \sin(n\theta + \phi) \quad for \quad E_z, \tag{A.37}$$

$$g(\theta) = \cos(n\theta + \phi) \quad for \quad H_z, \tag{A.38}$$

ϕ is a constant phase-shift. Solutions of Eq. (A.36) have to reflect a complexity of the spatial azimuthal profile of a waveguide. The profile, which is shown in Fig.3.5 (b), can be disintegrated to the three separated areas, that the relative susceptibility reads

$$\epsilon_r(r) = \begin{cases} \epsilon_1 & 0 \le r < r_1, \\ \epsilon_2 & r_1 \le r \le r_2, \\ \epsilon_3 & r_2 < r < \infty. \end{cases} \tag{A.39}$$

Upper limit ∞ has been set from a convention and also considering the localization of field in the proximity of the ring core. It is clear, that the final solution has the form of a sum of contributions originating in each interval of the azimuthal coordinate r. A solution of Eq.(A.36) for the electric field E_z is given by

$$E_z(r,\theta,z) = e^{i\beta z}\left\{\begin{array}{c} A_n I_n(k_1 r)\, rect_{[0,r_1]}(r) \\ +\left[B_n J_n(k_2 r) + C_n Y_n(k_2 r)\right] rect_{[r1,r_2]}(r) \\ +D_n K_n(k_3 r)\, rect_{[r_2,\infty]}(r) \end{array}\right\}\sin(n\theta + \phi) \tag{A.40}$$

and for the magnetic field H_z

$$H_z(r,\theta,z) = e^{i\beta z}\left\{\begin{array}{c} E_n I_n(k_1 r)\, rect_{[0,r_1]}(r) \\ +\left[F_n J_n(k_2 r) + G_n Y_n(k_2 r)\right] rect_{[r1,r_2]}(r) \\ +H_n K_n(k_3 r)\, rect_{[r_2,\infty]}(r) \end{array}\right\}\cos(n\theta + \phi), \tag{A.41}$$

where J_n (Y_n) is the Bessel function of the first (second) kind and I_n (K_n) is the modified Bessel function of the first (second) kind. The function $rect_{[a,b]}(r)$ is equal to 1 for $r \in \langle a, b\rangle$ and 0 elsewhere. Constants $A_n, B_n, ..$ etc. are calculated as a solution of the characteristic equation as we explain in following lines. The magnitude of transversal wave-vector in each area has form

$$k_1^2 = \beta^2 - k_0^2\epsilon_1, \tag{A.42}$$
$$k_2^2 = k_0^2\epsilon_2 - \beta^2, \tag{A.43}$$
$$k_3^2 = \beta^2 - k_0^2\epsilon_3. \tag{A.44}$$

Missing components of an electromagnetic field can be straightforwardly derived from the Maxwell equations. Electric field components write as:

$$E_r(r,\theta) = \frac{i}{\omega^2\epsilon_r\epsilon_0\mu - \beta^2}\left[\beta\frac{\partial E_z}{\partial r} + \frac{\mu\omega}{r}\frac{\partial H_z}{\partial \theta}\right] \tag{A.45}$$

and

$$E_\theta(r,\theta) = \frac{i}{\omega^2\epsilon_r\epsilon_0\mu - \beta^2}\left[\frac{\beta}{r}\frac{\partial E_z}{\partial \theta} - \mu\omega\frac{\partial H_z}{\partial r}\right]. \tag{A.46}$$

Magnetic field components are following:

$$H_r(r,\theta) = \frac{i}{\omega^2\epsilon_r\epsilon_0\mu - \beta^2}\left[\beta\frac{\partial H_z}{\partial r} - \frac{\omega\epsilon_r\epsilon_0}{r}\frac{\partial E_z}{\partial \theta}\right] \tag{A.47}$$

and

$$H_\theta(r,\theta) = \frac{i}{\omega^2\epsilon_r\epsilon_0\mu - \beta^2}\left[\frac{\beta}{r}\frac{\partial H_z}{\partial \theta} + \omega\epsilon_r\epsilon_0\frac{\partial E_z}{\partial r}\right]. \tag{A.48}$$

The next basic step towards the characteristic equation is utilization of continuity requirements at interfaces of the core and inner-and-outer claddings at $r = r_1, r_2$ for E_z, H_z, E_θ and H_θ. All eight conditions put together can be written as

$$\begin{aligned}
&E_z\left(r = r_1^-, \theta\right) = E_z\left(r = r_1^+, \theta\right), \qquad &&H_z\left(r = r_1^-, \theta\right) = H_z\left(r = r_1^+, \theta\right),\\
&E_z\left(r = r_2^-, \theta\right) = E_z\left(r = r_2^+, \theta\right), \qquad &&H_z\left(r = r_2^-, \theta\right) = H_z\left(r = r_2^+, \theta\right),\\
&E_\theta\left(r = r_1^-, \theta\right) = E_z\left(r = r_1^+, \theta\right), \qquad &&H_\theta\left(r = r_1^-, \theta\right) = H_\theta\left(r = r_1^+, \theta\right),\\
&E_\theta\left(r = r_2^-, \theta\right) = E_z\left(r = r_2^+, \theta\right), \qquad &&H_\theta\left(r = r_2^-, \theta\right) = H_\theta\left(r = r_2^+, \theta\right).
\end{aligned} \tag{A.49}$$

Super-scripts + and - mean left and right sides of the interface placed in the position r. Inserting Eq.(A.40) and Eq.(A.41) to Eq.(A.45-A.48), one obtains a set of equations from Eq.(A.49) for an unknown vector $\mathbf{u} = (A_n, B_n, C_n, D_n, E_n, F_n, G_n, H_n)^T$. The set of equations can be reorganised to the matrix X as follows

$$\begin{pmatrix}
I_n(k_1r_1) & -J_n(k_2r_1) & -Y_n(k_2r_1) & 0 & 0 \\
0 & J_n(k_2r_2) & Y_n(k_2r_2) & -K_n(k_3r_2) & 0 \\
-\frac{n\beta I_n(k_1r_1)}{r_1k_1^2} & -\frac{n\beta J_n(k_2r_1)}{r_1k_2^2} & -\frac{n\beta Y_n(k_2r_1)}{r_1k_2^2} & 0 & \frac{\omega\mu I_n'(k_1r_1)}{k_1} \\
0 & \frac{n\beta J_n(k_2r_2)}{r_2k_2^2} & \frac{n\beta Y_n(k_2r_2)}{r_2k_2^2} & \frac{n\beta K_n(k_3r_2)}{r_2k_3^2} & 0 \\
0 & 0 & 0 & 0 & I_n(k_1r_1) \\
0 & 0 & 0 & 0 & 0 \\
-\frac{\omega\epsilon_0\epsilon_1 I_n'(k_1.r_1)}{k_1} & -\frac{\omega\epsilon_0\epsilon_2 J_n'(k_2r_1)}{k_2} & -\frac{\omega\epsilon_0\epsilon_2 Y_n'(k_2r_1)}{k_2} & 0 & \frac{n\beta.I_n(k_1r_1)}{r_1k_1^2} \\
0 & \frac{\omega\epsilon_0\epsilon_2 J_n'(k_2r_2)}{k_2} & \frac{\omega\epsilon_0\epsilon_2 Y_n'(k_2r_2)}{k_2} & \frac{\omega\epsilon_0\epsilon_3 K_n'(k_3r_2)}{k_3} & 0
\end{pmatrix}$$

$$\begin{pmatrix}
0 & 0 & 0 \\
0 & 0 & 0 \\
\frac{\omega\mu J_n'(k_2r_1)}{k_2} & \frac{\omega\mu Y_n'(k_2r_1)}{k_2} & 0 \\
-\frac{\omega\mu J_n'(k_2r_2)}{k_2} & -\frac{\omega\mu Y_n'(k_2r_2)}{k_2} & -\frac{\omega\mu K_n'(k_3r_2)}{k_3} \\
-J_n(k_2r_1) & -Y_n(k_2r_1) & 0 \\
J_n(k_2r_2) & Y_n(k_2r_2) & -K_n(k_3r_2) \\
\frac{n\beta J_n(k_2r_1)}{r_1k_2^2} & \frac{n\beta Y_n(k_2r_1)}{r_1k_2^2} & 0 \\
-\frac{n\beta J_n(k_2r_2)}{r_2k_2^2} & -\frac{n\beta Y_n(k_2r_2)}{r_2k_2^2} & -\frac{n\beta K_n(k_3r_2)}{r_2k_3^2}
\end{pmatrix}
\begin{pmatrix} A_n \\ B_n \\ C_n \\ D_n \\ E_n \\ F_n \\ G_n \\ H_n \end{pmatrix}
= \begin{pmatrix} 0 \\ 0 \\ 0 \\ 0 \\ 0 \\ 0 \\ 0 \\ 0 \end{pmatrix}, \quad \text{(A.50)}$$

that writes in the simplest form $X\mathbf{u} = 0$. The apostrophe in Eq.(A.50) denotes $\frac{\partial}{\partial r}$. A non-trivial solution of this equation imposes the condition on the determinant of X that must be equal to zero. This requirement results into the characteristic equation (etc. the dispersion equation) for the propagation constant β of hybrid modes of order n. Based on the knowledge of β, the profile of whole electromagnetic field of a guided mode can be constructed using Eq.(A.45-A.48). We have generally considered only hybrid modes, which have significantly contributing most of $\mathbf{E}, \mathbf{H}$ components, however for some values of n the characteristic equation factorizes in a such way, that only-electric (TE) or only-magnetic (TM) modes are recovered.

Appendix B

Classical and Quantum Random Walk

Here, we make a short overview of the fundamentals of random walks. We start with the classical random walk (CRW) and later on we introduce the concept of quantum random walk (QRW), which represents an advance tool for many quantum computing algorithms [8]. We review both discrete and continuous versions of QRWs.

B.1 Classical Random Walk

We start with the simple case of a classical random walk, which is usually considered as a Markovian process (or chain), where each step depends only on the actual position and the transition probabilities of leaving this position to the next ones. The Brownian movement is a typical example of a classical randomn walk. Classical random walks play an important role in the modern financial theory, chemistry and biology [168].

The fundamental principle can be understand using the simplest case of walking on a line, as shown in Fig.B.1(a). However, one can also consider more complicated topological structures in many dimensions. In the current position i, the classical walker has some probability of going to the left $P_L(i)$ or to the right $P_R(i)$, in each step, but it can do only one particular movement. Without loosing a generality, let set $P_L(i) = P_R(i) = 0.5$. Then, after n-steps the probability distribution of finding the walker in the position i is equal to

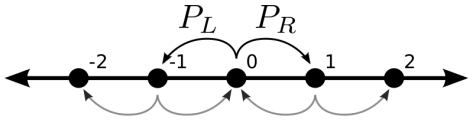

(a)

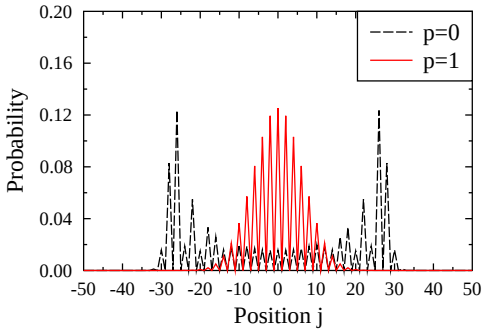

(b)

Figure B.1: (a) Simple random walk on a line. (b) Position probabilities of detecting a walker after 40 steps for QRW with a different strength of decoherence (see the legend). Note, that the CRW corresponds to p equal to 1.

$$P(i,n) = \begin{cases} \frac{1}{2^n}\begin{pmatrix} n \\ \frac{n+i}{2} \end{pmatrix} & i = -n, -n+2, ..., n-2, n, \\ 0 & i = -n+1, -n+3, ...n-1, \\ 0 & |i| > n, \end{cases} \tag{B.1}$$

which corresponds to components of the Pascal triangle. The standard deviation σ depends on the amount of steps via the function $\sim \sqrt{n}$, which reflects a diffusive propagation. The probability distribution after 40 steps is depicted in Fig.B.1(b) for p=1.

B.2 Discrete Quantum Random Walk

The main principle of a quantum random walk is the superposition of probability amplitudes, or in other words, the interference effect. This allows the walker to move faster $\sigma \sim n$. This corresponds to a ballistic propagation.

We first consider the discrete quantum random walk (DQRW), which is a quantum mechanic analogy of the classical one [167]. The walker moves in the position Hilbert space $\mathcal{H}_P$ which is spanned by position (site) vectors $\{|j\rangle : j \in \mathcal{Z}, \langle i|j\rangle = \delta_{ij}\}$. The decision of where to go (coin-tossing) is done in the coin Hilbert space $\mathcal{H}_c$ spanned by vectors $\{|\uparrow\rangle, |\downarrow\rangle\}$. The stroboscopic coherent evolution of DQRW is given by the operator $\hat{U} = \hat{S}\hat{H}$. The coin-tossing is represent an unitary operator, usually by the Hadamard

operator, with matrix representation

$$\hat{H} = \frac{1}{\sqrt{2}} \begin{pmatrix} 1 & 1 \\ 1 & -1 \end{pmatrix}. \tag{B.2}$$

The operator $\hat{H}$ creates superposition states of input states. In a general case, the coin-tossing operator can be parametrized by α, θ, ψ and expressed as

$$\hat{H}(\alpha, \theta, \phi) = \begin{pmatrix} \sqrt{\alpha} & \sqrt{1-\alpha}e^{i\theta} \\ \sqrt{1-\alpha}e^{i\theta} & -\sqrt{\alpha}e^{i(\theta+\phi)} \end{pmatrix}. \tag{B.3}$$

The Hadamard operator is recovered for $\alpha = 0.5$ and $\theta = \psi = 0$. The operator $\hat{S}$ is responsible for the walker jump to next position according to the result of tossing

$$\hat{S} = \sum_i \left(|i+1, \uparrow\rangle\langle i, \uparrow| + |i-1, \downarrow\rangle\langle i, \downarrow| \right). \tag{B.4}$$

Now, let us consider the walker in an initial state $|\psi(0)\rangle$, the next step is $|\psi(1)\rangle = \hat{U}|\Psi(0)\rangle$, so after performing n-steps, the final state is $|\psi(n)\rangle = \hat{U}^n|\psi(0)\rangle$. An example of coherent evolution for the initial state $|\psi(0)\rangle = |0\rangle \otimes \frac{1}{\sqrt{2}}(|\uparrow\rangle + |\downarrow\rangle)$ is depicted in Fig. B.1(b) for p=0.

To incorporate the effect of decoherence on the evolution of walker, density matrices have to be used. The density matrix $\hat{\rho}^{(n)}$ is in each step transformed to the next $\hat{\rho}^{(n+1)}$ via a completely positive (CP) map

$$\hat{\rho}^{(n+1)} = \hat{U}\hat{\rho}^{(n)}\hat{U}^\dagger, \tag{B.5}$$

Presence of decoherence induces the transition from the quantum regime to the classical regime. In the concept of QM measurement, this corresponds to a constant observation of the walker's actual state in both spaces, i.e., either the position or coin space. There are several equivalent ways how to introduce decoherence. Firstly, decoherence can be caused by a pure dephasing [197] represented by random phase kicks in each step (see the Eq.4.6 in the Section 3.2). Another source of decoherence is coupling the walker to a reservoir (bath), representing a typical fluctuating environment. The dynamic of a walker can be described via the Limblad equation in the following form

$$\hat{\rho}^{(n+1)} = (1-p)\,\hat{U}\hat{\rho}^n\hat{U}^\dagger + p \sum_{j \in \mathcal{H}_P} \hat{K}_j \hat{U}\hat{\rho}^{(n)}\hat{U}^\dagger \hat{K}_j^\dagger, \tag{B.6}$$

where $p \in \langle 0, 1\rangle$ is a dimensionless parameter describing the strength of the reservoir

coupling, and $\hat{K}_j$, for sites $j \in \mathcal{Z}$, are Kraus operators [8]. Only diagonal elements of the density matrix are preserved in the second non-unitary term of Eq.(B.6). Therefore, as the parameter p increases, off-diagonal terms of $\hat{\rho}$, representing correlations (mutual coherences), are washed out.

B.3 Continuous Quantum Random Walk

Now, we deal with the situation when the walker evolves continuously in time. Once again, the walker is moving between sites of an infinite line. Its coherent propagation can be described by the Hamiltonian

$$\hat{H} = \sum_{j \in \mathcal{Z}} \beta_j \hat{a}_j^\dagger \hat{a}_j + \sum_{\substack{k,l \in \mathcal{Z} \\ k \neq l}} \kappa_{k,l} \hat{a}_k^\dagger \hat{a}_l, \tag{B.7}$$

β_j are site energies and $\kappa_{k,l}$ are coupling (hoping) rates between different sites. Note that this Hamiltonian also describes the tight-binding model of an electron hoping between different atom sites in a crystal lattice [217]. For the walk on a line, where the walker moves only between adjacent sites, couplings can be express as $\kappa_{k,l} = \kappa_{k,k+1}\delta_{k+1,l} + \kappa_{k,k-1}\delta_{k-1,l}$. The coherent evolution of the state $|\psi(t)\rangle$ is governed by the Schrödinger equation

$$\frac{\partial |\psi(t)\rangle}{\partial t} = \frac{1}{i}\hat{H}|\psi(t)\rangle. \tag{B.8}$$

This equation represents a set of ODEs that can be solved, for example, by the Runga-Kutta methods [218]. For the uniformly ordered sites on a line, the solution has the form of Bessel functions [170]. When decoherence is present, the walker's propagation is driven by the Limblad master equation for the density matrix [171]

$$i\frac{\partial \hat{\rho}}{\partial t} = \left[\hat{\rho}, \hat{H}\right] + \mathcal{L}\left[\hat{\rho}\right], \tag{B.9}$$

where $\mathcal{L}$ is the Limblad superoperator, which is responsible for the effects of the noisy environment. This superoperator can be written as

$$\mathcal{L}\left[\hat{\rho}\right] = \sum_i \gamma_i \left(\hat{A}_i \hat{\rho} \hat{A}_i^\dagger - \frac{1}{2}\hat{\rho}\hat{A}_i^\dagger \hat{A}_i - \frac{1}{2}\hat{A}_i^\dagger \hat{A}_i \hat{\rho} \right), \tag{B.10}$$

where $\hat{A}_i$ are Limblad operators. The coefficients γ_i reflect the interaction strength of sites i with the reservoir.

Appendix C

Quantifying the First-Order Coherence of the Single Photon

C.1 Amount of Incoherence

The density matrix that characterizes the quantum state of one of the photons that constitute the pair, for instance $\hat{\rho}_A$ for photon A, is obtained by tracing out the variables describing photon B, so

$$\hat{\rho}_A = \int dx \int dx' \rho_A(x, x') |x\rangle_A \langle x'|_A, \tag{C.1}$$

where

$$\rho_A(x, x') = \int dy \Psi(x, y) \Psi^* \left(x', y\right). \tag{C.2}$$

Notice that $\rho_A(x, x')$ is the well-known first-order correlation function $G_A^{(1)}(x, x')$ of photon A, defined as

$$G_A^{(1)}(x, x') = \mathrm{T}r \left[\hat{\rho}_A \hat{E}_A^{(-)}(x) \hat{E}_A^{(+)}\left(x'\right)\right], \tag{C.3}$$

where $\hat{E}_A^{(+)}$ and $\hat{E}_A^{(-)}$ are the positive- and negative-frequency electric-field operators [202]. The first-order correlation function for photon B is defined similarly.

Making use of Eqs.(4.16) and (C.1), we obtain

$$G_A^{(1)}(x, x') \sim \exp\left[-(\alpha+\beta) x^2 - (\alpha+\beta) x'^2 + \frac{(\alpha-\beta)^2}{2(\alpha+\beta)} \left(x + x'\right)^2\right]. \tag{C.4}$$

The Gaussian form of two-photon amplitude, as defined in Eq.(4.16), allows us to quantify

the width of photon A in the position space using $G_A^{(1)}(x,x')$. The rms spatial width of photon A is

$$\sigma^2 = \frac{\int dx\, x^2 G_A^{(1)}(x,x)}{\int dx\, G_A^{(1)}(x,x)} = \frac{\alpha+\beta}{16\alpha\beta}. \tag{C.5}$$

The two-photon amplitude $\Psi(p,q)$ in the transverse wave-number domain is equal to

$$\Phi(q,k) \sim \exp\left[-\frac{(q+k)^2}{16\alpha} - \frac{(q-k)^2}{16\beta}\right]. \tag{C.6}$$

Similarly to the case considered above, the first-order correlation function in transverse wave-number domain reads

$$G_A^{(1)}(q,q') = \mathrm{T}r\left[\hat{\rho}_A\, \hat{a}_A^{\dagger}(q)\hat{a}_A(q')\right]. \tag{C.7}$$

One can calculate the rms width of photon A in the transverse wave-number domain as

$$W^2 = \frac{\int dq\, q^2 G_A^{(1)}(q,q)}{\int dq\, G_A^{(1)}(q,q)} = \alpha+\beta. \tag{C.8}$$

Here we quantify the first-order coherence of photon A as the product of its spatial beam width (σ) by its width in the transverse wavevector domain (W)

$$\gamma = \sigma W = \frac{\alpha+\beta}{4\sqrt{\alpha\beta}}, \tag{C.9}$$

this parameter γ represents the amount of incoherence. For more details concerning quantification of coherence, see [219]. Making use of Eqs.(C.5) and (C.9) one easily obtains Eqs.(4.17) and (4.18) in the Section 4.3. The minimum value of γ is $\gamma = 0.5$. It corresponds to a separable two-photon state with $\alpha = \beta$. In this case, photon A (and photon B) show first-order coherence. For entangled states, photon A is described by an incoherent superposition of Hermite-Gauss modes, whose number increases with a corresponding increase of the degree of entanglement between photons A and B. Therefore, increasing values of γ correspond to photons with a lower degree of coherence.

List of author's publications

[A1] J. Svozilík, J. Peřina Jr, and J. P. Torres, "High spatial entanglement via chirped quasi-phase-matched optical parametric down-conversion," Phys. Rev. A **86**, 052318 (2012).

[A2] J. Svozilík, M. Hendrych, A. S. Helmy, and J. P. Torres, "Generation of paired photons in a quantum separable state in bragg reflection waveguides," Opt. Express **19**, 3115 (2011).

[A3] J. Svozilík, M. Hendrych, and J. P. Torres, "Bragg reflection waveguide as a source of wavelength-multiplexed polarization-entangled photon pairs," Opt. Express **20**, 15015 (2012).

[A4] A. Valles, M. Hendrych, J. Svozilík, R. Machulka, P. Abolghasem, D. Kang, B. J. Bijlani, A. S. Helmy, and J. P. Torres, "Generation of polarization-entangled photon pairs in a bragg reflection waveguide," Opt. Express **21**, 10841 (2013).

[A5] J. Svozilík and J. Peřina Jr., "Properties of entangled photon pairs generated in periodically poled nonlinear crystals," Phys. Rev. A **80**, 023819 (2009).

[A6] J. Svozilík and J. Peřina Jr., "Generation of entangled photon pairs in periodically poled nonlinear crystals," Proc. SPIE **7354**, 73540 (2009).

[A7] J. Svozilík and J. Peřina Jr., "Intense ultra-broadband down-conversion from randomly poled nonlinear crystals," Opt. Express **18**, 27130 (2010).

[A8] J. Peřina Jr. and J. Svozilík, "Randomly poled crystals as a source of photon pairs," Phys. Rev. A **83**, 033808 (2011).

[A9] J. Svozilík, A. Valles, M. Hendrych, and J. P. Torres, "Bragg reflection waveguides as a source of photon pairs: theory and experiments," Proc. SPIE **8072**, 80720 (2011).

[A10] J. Svozilík and J. Peřina Jr., "Intense ultra-broadband down-conversion from randomly poled nonlinear crystals," Proc. SPIE **8071**, 807105 (2011).

[A11] D. Javůrek, J. Svozilík, and J. Peřina Jr., "Entangled photon-pair generation in metallo-dielectric photonic bandgap structures," Proc. SPIE **8697**, 869727 (2012).

[A12] J. Svozilík, R. de Jesus León-Montiel, and J. P. Torres, "Implementation of a spatial two-dimensional quantum random walk with tunable decoherence," Phys. Rev. A **86**, 052327 (2012).

[A13] R. Machulka, J. Svozilík, J. Soubusta, J. Peřina Jr., and O. Haderka, "Spatial and spectral properties of the pulsed second-harmonic generation in a pp-ktp waveguide," Phys. Rev. A **87**, 013836 (2013).

[A14] J. Svozilík and J. Peřina Jr., "Higher-order stochastic quasi-phase-matching in spontaneous parametric down-conversion," Opt. Commun. **306**, 113 (2013).

[A15] R. de J. León-Montiel, J. Svozilík, L. J. Salazar-Serrano, and J. P. Torres, "Role of the spectral shape of quantum correlations in two-photon virtual-state spectroscopy," New J. Phys. **15**, 053023 (2013).

[A16] J. Svozilík, J. Peřina Jr., and J. P. Torres, "Measurement-based tailoring of anderson localization of partially coherent light," Phys. Rev. A **89**, 053808 (2014).

[A17] R. d. J. León-Montiel and J. P. Svozilík, J. Juan P. Torres, "Generation of a tunable environment for the simulation of excitonic transport in classical systems," submitted to Phys. Rev. E (2014).

[A18] D. Javůrek, J. Svozilík, and J. Peřina Jr., "Generation of photon pairs with nonzero orbital angular in a ring fiber," submitted to Opt. Express (2014).

[A19] D. Javůrek, J. Svozilík, and J. Peřina Jr., "Emission of oam entangled photon pairs in a nonlinear ring fiber utilizing spontaneous parametric down-conversion," submitted to Phys. Rev. A (2014).

[A20] D. Javůrek, J. Peřina Jr., and J. Svozilík, "Generation of photon pairs in nonlinear metal-dielectric layered structures," before submission to Phys. Rev. A (2014).

Bibliography

[1] M. Planck, "Ueber das gesetz der energieverteilung im normalspectrum," Ann. Phys. **309**, 553 (1901).

[2] A. Einstein, B. Podolsky, and N. Rosen, "Can quantum-mechanical description of physical reality be considered complete?" Phys. Rev. **47**, 777 (1935).

[3] E. Schrödinger and M. Born, "Discussion of probability relations between separatedsystems," Proc. Camb. Philos. Soc. **31**, 555 (1935).

[4] S. Weinberg, *Lectures on quantum mechanics* (Cambridge University Press, 2012).

[5] J. S. Bell, "On the einstein-podolsky-rosen paradox," Physics **1**, 195 (1964).

[6] J. F. Clauser, M. A. Horne, A. Shimony, and R. A. Holt, "Proposed Experiment to Test Local Hidden-Variable Theories," Phys. Rev. Lett. **23**, 880 (1969).

[7] V. Vedral, M. B. Plenio, M. A. Rippin, and P. L. Knight, "Quantifying entanglement," Phys. Rev. Lett. **78**, 2275 (1997).

[8] M. A. Nielsen and I. L. Chuang, *Quantum computation and quantum information* (Cambridge University Press, 2010).

[9] C. K. Law and J. H. Eberly, "Analysis and Interpretation of High Transverse Entanglement in Optical Parametric Down Conversion," Phys. Rev. Lett. **92**, 127903 (2004).

[10] C. K. Law, I. A. Walmsley, and J. H. Eberly, "Continuous Frequency Entanglement: Effective Finite Hilbert Space and Entropy Control," Phys. Rev. Lett. **84**, 5304 (2000).

[11] R. Horodecki, P. Horodecki, M. Horodecki, and K. Horodecki, "Quantum entanglement," Rev. Mod. Phys. **81**, 865 (2009).

[12] S. Walborn, A. De Oliveira, R. Thebaldi, and C. Monken, "Entanglement and conservation of orbital angular momentum in spontaneous parametric down-conversion," Phys. Rev. A **69**, 023811 (2004).

[13] G. Molina-Terriza, J. P. Torres, and L. Torner, "Twisted photons," Nature Phys. **3**, 305 (2007).

[14] J. T. Barreiro, N. K. Langford, N. A. Peters, and P. G. Kwiat, "Generation of hyperentangled photon pairs," Phys. Rev. Lett. **95**, 260501 (2005).

[15] D. Kang, L. Helt, S. V. Zhukovsky, J. P. Torres, J. Sipe, and A. Helmy, "Hyperentangled photon sources in semiconductor waveguides," Phys. Rev. A **89**, 023833 (2014).

[16] S. J. Freedman and J. F. Clauser, "Experimental test of local hidden-variable theories," Phys. Rev. Lett. **28**, 938 (1972).

[17] A. Aspect, J. Dalibard, and G. Roger, "Experimental test of bell's inequalities using time-varying analyzers," Phys. Rev. Lett. **49**, 1804 (1982).

[18] E. Moreau, I. Robert, L. Manin, V. Thierry-Mieg, J. Gérard, and I. Abram, "Quantum cascade of photons in semiconductor quantum dots," Phys. Rev. Lett. **87**, 183601 (2001).

[19] N. Akopian, N. Lindner, E. Poem, Y. Berlatzky, J. Avron, D. Gershoni, B. Gerardot, and P. Petroff, "Entangled photon pairs from semiconductor quantum dots," Phys. Rev. Lett. **96**, 130501 (2006).

[20] D. C. Burnham and D. L. Weinberg, "Observation of Simultaneity in Parametric Production of Optical Photon Pairs," Phys. Rev. Lett. **25**, 84 (1970).

[21] Y. H. Shih and C. O. Alley, "New type of einstein-podolsky-rosen-bohm experiment using pairs of light quanta produced by optical parametric down conversion," Phys. Rev. Lett. **61**, 2921 (1988).

[22] D. Bouwmeester, J.-W. Pan, K. Mattle, M. Eibl, H. Weinfurter, and A. Zeilinger, "Experimental quantum teleportation," Nature **390**, 575 (1997).

[23] P. G. Kwiat, E. Waks, A. G. White, I. Appelbaum, and P. H. Eberhard, "Ultrabright source of polarization-entangled photons," Phys. Rev. A **60**, 773 (1999).

[24] M. Savanier, A. Andronico, A. Lemaître, C. Manquest, I. Favero, S. Ducci, and G. Leo, "Nearly-degenerate three-wave mixing at 1.55 μm in oxidized algaas waveguides," Opt. Express **19**, 22582 (2011).

[25] R. Horn, P. Abolghasem, B. J. Bijlani, D. Kang, A. Helmy, and G. Weihs, "Monolithic source of photon pairs," Phys. Rev. Lett. **108**, 153605 (2012).

[26] N. Matsuda, H. Le Jeannic, H. Fukuda, T. Tsuchizawa, W. J. Munro, K. Shimizu, K. Yamada, Y. Tokura, and H. Takesue, "A monolithically integrated polarization entangled photon pair source on a silicon chip," Sci. Rep. **2**, 817 (2012).

[27] M. F. Saleh, B. E. Saleh, and M. C. Teich, "Modal, spectral, and polarization entanglement in guided-wave parametric down-conversion," Phys. Rev. A **79**, 053842 (2009).

[28] J. Lugani, S. Ghosh, and K. Thyagarajan, "Generation of modal-and path-entangled photons using a domain-engineered integrated optical waveguide device," Phys. Rev. A **83**, 062333 (2011).

[29] Q. Lin, F. Yaman, and G. P. Agrawal, "Photon-pair generation in optical fibers through four-wave mixing: Role of raman scattering and pump polarization," Phys. Rev. A **75**, 023803 (2007).

[30] X. Li, P. L. Voss, J. E. Sharping, and P. Kumar, "Optical-fiber source of polarization-entangled photons in the 1550 nm telecom band," Phys. Rev. Lett. **94**, 053601 (2005).

[31] C. H. Bennett and S. J. Wiesner, "Communication via one-and two-particle operators on Einstein-Podolsky-Rosen states," Phys. Rev. Let. **69**, 2881 (1992).

[32] C. H. Bennett, G. Brassard, C. Crépeau, R. Jozsa, A. Peres, and W. K. Wootters, "Teleporting an unknown quantum state via dual classical and Einstein-Podolsky-Rosen channels," Phys. Rev. Let. **70**, 1895 (1993).

[33] A. K. Ekert, "Quantum cryptography based on Bell's theorem," Phys. Rev. Lett. **67**, 661 (1991).

[34] D. Deutsch, "Quantum theory, the Church-Turing principle and the universal quantum computer," P. Roy. Soc. Lond. A. Mat. **400**, 97 (1985).

[35] P. W. Shor, "Polynomial-time algorithms for prime factorization and discrete logarithms on a quantum computer," SIAM J. Comput. **26**, 1484 (1997).

[36] L. K. Grover, "A fast quantum mechanical algorithm for database search," in "Proceedings of the twenty-eighth annual ACM symposium on Theory of computing," (ACM, 1996), p. 212.

[37] V. Giovannetti, S. Lloyd, and L. Maccone, "Advances in quantum metrology," Nature Photon. **5**, 222 (2011).

[38] S. F. Huelga, C. Macchiavello, T. Pellizzari, A. K. Ekert, M. B. Plenio, and J. I. Cirac, "Improvement of frequency standards with quantum entanglement," Phys. Rev. Lett. **79**, 3865 (1997).

[39] M. Nasr, B. Saleh, A. Sergienko, and M. Teich, "Dispersion-cancelled and dispersion-sensitive quantum optical coherence tomography," Opt. Express **12**, 1353 (2004).

[40] M. Sarovar, A. Ishizaki, G. R. Fleming, and K. B. Whaley, "Quantum entanglement in photosynthetic light-harvesting complexes," Nature Phys. **6**, 462 (2010).

[41] N. Lambert, Y.-N. Chen, Y.-C. Cheng, C.-M. Li, G.-Y. Chen, and F. Nori, "Quantum biology," Nature Phys **9**, 10 (2013).

[42] F. Caruso, A. W. Chin, A. Datta, S. F. Huelga, and M. B. Plenio, "Highly efficient energy excitation transfer in light-harvesting complexes: The fundamental role of noise-assisted transport," J. Chem. Phys. **131**, 105106 (2009).

[43] H. J. Hogben, T. Biskup, and P. Hore, "Entanglement and sources of magnetic anisotropy in radical pair-based avian magnetoreceptors," Phys. Rev. Lett. **109**, 220501 (2012).

[44] M. Fiorentino, S. M. Spillane, R. G. Beausoleil, T. D. Roberts, P. Battle, and M. W. Munro, "Spontaneous parametric down-conversion in periodically poled KTP waveguides and bulk crystals," Opt. Express **15**, 7479 (2007).

[45] K. Banaszek, A. B. U'Ren, and I. A. Walmsley, "Generation of correlated photons in controlled spatial modes by downconversion in nonlinear waveguides," Opt. Lett. **26**, 1367 (2001).

[46] F. Steinlechner, P. Trojek, M. Jofre, H. Weier, D. Perez, T. Jennewein, R. Ursin, J. Rarity, M. W. Mitchell, J. P. Torres *et al.*, "A high-brightness source of polarization-entangled photons optimized for applications in free space," Opt. Express **20**, 9640 (2012).

[47] A. Cowan and J. F. Young, "Mode matching for second-harmonic generation in photonic crystal waveguides," Phys. Rev. B **65**, 085106 (2002).

[48] K. Moutzouris, S. V. Rao, M. Ebrahimzadeh, A. De Rossi, M. Calligaro, V. Ortiz, and V. Berger, "Second-harmonic generation through optimized modal phase matching in semiconductor waveguides," Appl. Phys. Lett. **83**, 620 (2003).

[49] S. Ducci, L. Lanco, V. Berger, A. De Rossi, V. Ortiz, and M. Calligaro, "Continuous-wave second-harmonic generation in modal phase matched semiconductor waveguides," Appl. Phys Lett. **84**, 2974 (2004).

[50] A. S. Helmy, B. Bijlani, and P. Abolghasem, "Phase matching in monolithic Bragg reflection waveguides," Opt. Lett. **32**, 2399 (2007).

[51] J. Armstrong, N. Bloembergen, J. Ducuing, and P. Pershan, "Interactions between light waves in a nonlinear dielectric," Phys. Rev. **127**, 1918 (1962).

[52] M. Yamada, N. Nada, M. Saitoh, and K. Watanabe, "First-order quasi-phase matched $LiNbO_3$ waveguide periodically poled by applying an external field for efficient blue second-harmonic generation," App. Phys. Let. **62**, 435 (1993).

[53] B. R. West and A. Helmy, "Analysis and design equations for phase matching using bragg reflector waveguides," Selected Topics in Quantum Electronics, IEEE Journal of **12**, 431 (2006).

[54] B. R. West and A. S. Helmy, "Dispersion tailoring of the quarter-wave Bragg reflection waveguide," Opt. Express **14**, 4073 (2006).

[55] P. Abolghasem, M. Hendrych, X. Shi, J. P. Torres, and A. Helmy, "Bandwidth control of paired photons generated in monolithic Bragg reflection waveguides," Opt. Lett. **34**, 2000 (2009).

[56] I. Shoji, T. Kondo, A. Kitamoto, M. Shirane, and R. Ito, "Absolute scale of second-order nonlinear-optical coefficients," JOSA B **14**, 2268 (1997).

[57] J. L. P. Hughes, Y. Wang, and J. E. Sipe, "Calculation of linear and second-order optical response in wurtzite GaN and AlN," Phys. Rev. B **55**, 13630 (1997).

[58] N. Sanford, A. Davydov, D. Tsvetkov, A. Dmitriev, S. Keller, U. Mishra, S. DenBaars, S. Park, J. Han, and R. Molnar, "Measurement of second order susceptibilities of GaN and AlGaN," J. Appl. Phys. **97**, 053512 (2005).

[59] P. Abolghasem, J. Han, B. J. Bijlani, A. Arjmand, and A. S. Helmy, "Continuous-wave second harmonic generation in Bragg reflection waveguides," Opt. Lett. **34**, 9460 (2009).

[60] J.-B. Han, P. Abolghasem, D. Kang, B. J. Bijlani, and A. S. Helmy, "Difference-frequency generation in AlGaAs Bragg reflection waveguides," Opt. Lett. **35**, 2334 (2010).

[61] B. J. Bijlani and A. S. Helmy, "Bragg reflection waveguide diode lasers," Opt. Lett. **34**, 3734 (2009).

[62] B. J. Bijlani, P. Abolghasem, and A. S. Helmy, "Intracavity parametric fluorescence in diode lasers," in "CLEO: Science and Innovations," (Optical Society of America, 2011), p. PDPA3.

[63] P. P. Rohde, G. J. Pryde, J. L. O'Brien, and T. C. Ralph, "Quantum gate characterization in an extended Hilbert space," Phys. Rev. A **72**, 032306 (2005).

[64] I. A. Walmsley and M. G. Raymer, "Toward quantum-information processing with photons," Science **307**, 1733 (2005).

[65] P. Kok, W. J. Munro, K. Nemoto, T. C. Ralph, J. P. Dowling, and G. J. Milburn, "Linear optical quantum computing," Rev. Mod. Phys. **79**, 135 (2007).

[66] L. E. Vicent, A. B. U'Ren, R. Rangarajan, C. I. Osorio, J. P. Torres, L.Zhang, and I. A. Walmsley, "Design of bright, fiber-coupled and fully factorable photon pair sources," New J. Phys. **12**, 093027 (2010).

[67] T. Aichele, A. I. Lvovsky, and S. Schiller, "Optical mode characterization of single photons prepared by means of conditional measurements on a biphoton state," Eur. Phys. J. D **18**, 237 (2002).

[68] W. P. Grice, A. B. U'Ren, and I. A. Walmsley, "Eliminating frequency and space-time correlation in multiphoton states," Phys. Rev. A **64**, 063815 (2001).

[69] P. J. Mosley, J. S. Lundeen, B. J. Smith, P. Wasylczyk, A. B. U'Ren, C. Silberhorn, and I. A. Walmsley, "Heralded generation of ultrafast single photons in pure quantum states," Phys. Rev. Lett. **100**, 133601 (2008).

[70] J. P. Torres, F. Macià, S. Carrasco, and L.Torner, "Engineering the frequency correlations of entangled two-photon states by achromatic phase matching," Opt. Lett. **30**, 314 (2005).

[71] M. Hendrych, M. Mičuda, and J. P. Torres, "Tunable control of the frequency correlations of entangled photons," Opt. Lett. **32**, 2339 (2007).

[72] J. P. Torres, M. Hendrych, and A. Valencia, "Angular dispersion: an enabling tool in nonlinear and quantum optics," Adv. Opt. Photon. **2**, 319 (2010).

[73] Z. D. Walton, M. C. Booth, A. V. Sergienko, B. E. A. Saleh, and M. C. Teich, "Controllable frequency entanglement via auto-phase-matched spontaneous parametric down-conversion," Phys. Rev. A **67**, 053810 (2003).

[74] A. U'Ren, K. Banaszek, and I. Walmsley, "Photon engineering for quantum information processing," Quantum Inf. Comput. **3**, 480 (2003).

[75] S. Carrasco, J. P. Torres, L. Torner, A. V. Sergienko, B. E. Saleh, and M. C. Teich, "Spatial-to-spectral mapping in spontaneous parametric down-conversion," Phys. Rev. A **70**, 043817 (2004).

[76] A. Valencia, A. Ceré, X. Shi, G. Molina-Terriza, and J. P. Torres, "Shaping the waveform of entangled photons," Phys. Rev. Lett. **99**, 243601 (2007).

[77] X. Shi, A. Valencia, M. Hendrych, and J. Torres, "Generation of indistinguishable and pure heralded single photons with tunable bandwidth," Opt. Lett. **33**, 875 (2008).

[78] A. B. U'Ren, R. K. Erdmann, M. de la Cruz-Gutierrez, and I. A. Walmsley, "Generation of Two-Photon States with an Arbitrary Degree of Entanglement Via Nonlinear Crystal Superlattices," Phys. Rev. Lett. **97**, 223602 (2006).

[79] G. Laws, E. Larkins, I. Harrison, C. Molloy, and D. Somerford, "Improved refractive index formulas for the $al_xga_{1-x}n$ and $in_yga_{1-y}n$ alloys," J. Appl. Phys. **89**, 1108 (2001).

[80] S. Pezzagna, P. Vennéguès, N. Grandjean, A. D. Wieck, and J. Massies, "Submicron periodic poling and chemical patterning of gan," Appl. Phys. Lett. **87**, 062106 (2005).

[81] T. E. Chapuran, P. Toliver, N. A. Peters, J. Jackel, M. S. Goodman, R. J. Runser, S. R. McNown, N. Dallmann, R. J. Hughes, K. P. McCabe, J. E. Nordholt, C. G. Peterson, K. T. Tyagi, L. Mercer, and H. Dardy, "Optical networking for quantum key distribution and quantum communications," New J. Phys. **11**, 105001 (2009).

[82] A. L. Migdall, D. Branning, and S. Castelletto, "Tailoring single-photon and multiphoton probabilities of a single-photon on-demand source," Phys. Rev. A **66**, 053805 (2002).

[83] J. H. Shapiro and F. N. Wong, "On-demand single-photon generation using a modular array of parametric downconverters with electro-optic polarization controls," Opt. Lett. **32**, 2698 (2007).

[84] A. Fedrizzi, T. Herbst, A. Poppe, T. Jennewein, and A. Zeilinger, "A wavelength-tunable fiber-coupled source of narrowband entangled photons," Opt. Express **15**, 15377 (2007).

[85] H. C. Lim, A. Yoshizawa, H. Tsuchida, and K. Kikuchi, "Wavelength-multiplexed distribution of highly entangled photon-pairs over optical fiber," Opt. Express **26**, 22099 (2008).

[86] K. Thyagarajan, R. Das, O. Alibart, M. Micheli, D. B. Ostrowsky, and S. Tanzilli, "Increased pump acceptance bandwidth in spontaneous parametric downconversion process using Bragg reflection waveguides," Opt. Express **16**, 3577 (2008).

[87] D. Kang and A. S. Helmy, "Generation of polarization entangled photons using concurrent type-I and type-0 processes in AlGaAs ridge waveguides," Optics Lett. **37**, 1481 (2012).

[88] J. P. Torres, K. Banaszek, and I. A. Walmsley, "Engineering nonlinear optic sources of photonic entanglement," Prog. Optics **56**, 227 (2011).

[89] S. V. Zhukovsky, L. G. Helt, D. Kang, P. Abolghasem, A. S. Helmy, and J. E. Sipe, "Generation of maximally-polarization-entangled photons on a chip," Phys. Rev. A **85**, 013838 (2012).

[90] S. Gehrsitz, F. K. Reinhart, C. Gourgon, N. Herres, A. Vonlanthan, and H. Sigg, "The refractive index of Al(x)Ga(1-x)As below the band gap: Accurate determination and empirical modeling," J. Appl. Phys. **87**, 7825 (2000).

[91] A. Ling, A. Lamas-Linares, and C. Kurtsiefer, "Absolute emission rates of spontaneous parametric down-conversion into single transverse Gaussian modes," Phys. Rev. A **77**, 043834 (2008).

[92] S. Hill and W. K. Wootters, "Entanglement of a Pair of Quantum Bits," Phys. Rev. Lett. **78**, 5022 (1997).

[93] K. Wootters, "Entanglement of Formation of an Arbitrary State of Two Qubits," Phys. Rev. Lett. **80**, 2245 (1998).

[94] T. Yu and J. H. Eberly, "Quantum Open System Theory: Bipartite Aspects," Phys. Rev. Lett. **97**, 140403 (2006).

[95] Y. Kim and W. P. Grice, "Reliability of the beam-splitter–based Bell-state measurement," Phys. Rev. A **68**, 062305 (2003).

[96] P. P. Rohde and T. C. Ralph, "Frequency and temporal effects in linear optical quantum computing," Phys. Rev. A **71**, 032320 (2005).

[97] T. S. Humble and W. P. Grice, "Spectral effects in quantum teleportation," Phys. Rev. A **75**, 022307 (2007).

[98] W. Drexler, "Ultrahigh-resolution optical coherence tomography," J. Biomed. Opt. **9**, 47 (2004).

[99] A. Orieux, A. Eckstein, A. Lemaître, P. Filloux, I. Favero, G. Leo, T. Coudreau, A. Keller, P. Milman, and S. Ducci, "Direct bell states generation on a iii-v semiconductor chip at room temperature," Phys. Rev. Lett. **110**, 160502 (2013).

[100] N. Gisin, "Bell's inequality holds for all non-product states," Phys. Rev. A **154**, 201–202 (1991).

[101] A. Fine, "Hidden variables, joint probability, and the bell inequalities," Phys. Rev. Lett. **48**, 291 (1982).

[102] P. Abolghasem, J. Han, B. J. Bijlani, A. Arjmand, and A. S. Helmy, "Highly efficient second-harmonic generation in monolithic matching layer enhanced al ga as bragg reflection waveguides," IEEE Photon. Technol. Lett. **21**, 1462 (2009).

[103] P. Abolghasem, J.-B. Han, D. Kang, B. J. Bijlani, and A. S. Helmy, "Monolithic photonics using second-order optical nonlinearities in multilayer-core bragg reflection waveguides," IEEE J. Select. Topics Quantum Electron. **18**, 812 (2012).

[104] P. G. Kwiat, K. Mattle, H. Weinfurter, A. Zeilinger, A. V. Sergienko, and Y. Shih, "New high-intensity source of polarization-entangled photon pairs," Phys. Rev. Lett. **75**, 4337 (1995).

[105] L. Allen, M. W. Beijersbergen, R. J. C. Spreeuw, and J. P. Woerdman, "Orbital angular momentum of light and the transformation of laguerre-gaussian laser modes," Phys. Rev. A **45**, 8185 (1992).

[106] J. Nye and M. Berry, "Dislocations in wave trains," Proc. R. Soc. London, A **336**, 165 (1974).

[107] N. B. Baranova, B. Y. Zel'Dovich, A. V. Mamaev, N. Pilipetskii, and V. V. Shkukov, "Dislocations of the wavefront of a speckle-inhomogeneous field (theory and experiment)," Jetp. Lett. **33** (1981).

[108] J. Vaughan and D. Willetts, "Interference properties of a light beam having a helical wave surface," Opt. Commun. **30**, 263 (1979).

[109] G. D'Alessandro and G.-L. Oppo, "Gauss-laguerre modes: a "sensible" basis for laser dynamics," Opt. Commun. **88**, 130 (1992).

[110] A. M. Yao and M. J. Padgett, "Orbital angular momentum: origins, behavior and applications," Adv. Opt. Photon. **3**, 161 (2011).

[111] J. P. Torres and L. Torner, *Twisted Photons: Applications of Light with Orbital Angular Momentum* (John Wiley & Sons, 2011).

[112] G. Molina-Terriza, J. P. Torres, and L. Torner, "Management of the angular momentum of light: Preparation of photons in multidimensional vector states of angular momentum," Phys. Rev. Lett. **88**, 013601 (2001).

[113] S. Franke-Arnold, S. M. Barnett, E. Yao, J. Leach, J. Courtial, and M. Padgett, "Uncertainty principle for angular position and angular momentum," New J. Phys. **6**, 103 (2004).

[114] N. R. Heckenberg, R. McDuff, C. P. Smith, and A. G. White, "Generation of optical phase singularities by computer-generated holograms," Opt. Lett. **17**, 221 (1992).

[115] M. W. Beijersbergen, R. P. C. Coerwinkel, M. Kristensen, and J. P. Woerdman, "Helical-wavefront laser beams produced with a spiral phaseplate," Opt. Commun. **112**, 321 (1994).

[116] L. Marrucci, C. Manzo, and D. Paparo, "Optical spin-to-orbital angular momentum conversion in inhomogeneous anisotropic media," Phys. Rev. Lett. **96**, 163905 (2006).

[117] Y. Yan, J. Wang, L. Zhang, J.-Y. Yang, I. M. Fazal, N. Ahmed, B. Shamee, A. E. Willner, K. Birnbaum, and S. Dolinar, "Fiber coupler for generating orbital angular momentum modes," Opt. Lett. **36**, 4269 (2011).

[118] Y. Yan, Y. Yue, H. Huang, J.-Y. Yang, M. R. Chitgarha, N. Ahmed, M. Tur, S. J. Dolinar, and A. E. Willner, "Efficient generation and multiplexing of optical orbital angular momentum modes in a ring fiber by using multiple coherent inputs," Opt. Lett. **37**, 3645 (2012).

[119] S. A. Schulz, T. Machula, E. Karimi, and R. W. Boyd, "Integrated multi vector vortex beam generator," Opt. Express **21**, 16130 (2013).

[120] N. Bozinovic, Y. Yue, Y. Ren, M. Tur, P. Kristensen, H. Huang, A. E. Willner, and S. Ramachandran, "Terabit-scale orbital angular momentum mode division multiplexing in fibers," Science **340** (2013).

[121] G. Puentes, N. Hermosa, and J. P. Torres, "Weak measurements with orbital-angular-momentum pointer states," Phys. Rev. Lett. **109**, 040401 (2012).

[122] M. Padgett and R. Bowman, "Tweezers with a twist," Nature Phot. **5**, 343 (2011).

[123] P. Zhang, X.-F. Ren, X.-B. Zou, B.-H. Liu, Y.-F. Huang, and G.-C. Guo, "Demonstration of one-dimensional quantum random walks using orbital angular momentum of photons," Phys. Rev. A **75**, 052310 (2007).

[124] D. Kaszlikowski, P. Gnaciński, M. Żukowski, W. Miklaszewski, and A. Zeilinger, "Violations of local realism by two entangled n-dimensional systems are stronger than for two qubits," Phys. Rev. Lett. **85**, 4418 (2000).

[125] D. Collins, N. Gisin, N. Linden, S. Massar, and S. Popescu, "Bell inequalities for arbitrarily high-dimensional systems," Phys. Rev. Lett. **88**, 040404 (2002).

[126] G. Molina-Terriza, A. Vaziri, R. Ursin, and A. Zeilinger, "Experimental quantum coin tossing," Phys. Rev. Lett. **94**, 040501 (2005).

[127] S. S. R. Oemrawsingh, X. Ma, D. Voigt, A. Aiello, E. R. Eliel, G. W. 't Hooft, and J. P. Woerdman, "Experimental demonstration of fractional orbital angular momentum entanglement of two photons," Phys. Rev. Lett. **95**, 240501 (2005).

[128] A. Bruner, D. Eger, M. B. Oron, P. Blau, M. Katz, and S. Ruschin, "Temperature-dependent sellmeier equation for the refractive index of stoichiometric lithium tantalate," Opt. Lett. **28**, 194 (2003).

[129] S. Carrasco, J. P. Torres, L. Torner, A. Sergienko, B. E. A. Saleh, and M. C. Teich, "Enhancing the axial resolution of quantum optical coherence tomographyby chirped quasi-phase matching," Opt. Lett. **29**, 2429 (2004).

[130] M. B. Nasr, S. Carrasco, B. E. Saleh, A. V. Sergienko, M. C. Teich, J. P. Torres, L. Torner, D. S. Hum, and M. M. Fejer, "Ultrabroadband biphotons generated via chirped quasi-phase-matched optical parametric down-conversion," Phys. Rev. Lett. **100**, 183601 (2008).

[131] C. I. Osorio, G. Molina-Terriza, and J. P. Torres, "Correlations in orbital angular momentum of spatially entangled paired photons generated in parametric down-conversion," Phys. Rev. A **77**, 015810 (2008).

[132] J. Torres, A. Alexandrescu, and L. Torner, "Quantum spiral bandwidth of entangled two-photon states," Phys. Rev. A **68**, 050301 (2003).

[133] H. D. L. Pires, H. Florijn, and M. van Exter, "Measurement of the spiral spectrum of entangled two-photon states," Phys. Rev. Lett. **104**, 020505 (2010).

[134] A. Ekert and P. L. Knight, "Entangled quantum systems and the schmidt decomposition," American Journal of Physics **63**, 415–423 (1995).

[135] S. Walborn, A. De Oliveira, S. Pádua, and C. Monken, "Multimode hong-ou-mandel interference," Phys. Rev. Lett. **90**, 143601 (2003).

[136] M. Hamar, J. Peřina, O. Haderka, and V. Michálek, "Transverse coherence of photon pairs generated in spontaneous parametric down-conversion," Phys. Rev. A **81**, 043827 (2010).

[137] A. Mair, A. Vaziri, G. Weihs, and A. Zeilinger, "Entanglement of the orbital angular momentum states of photons," Nature **412**, 313 (2001).

[138] A. K. Jha, J. Leach, B. Jack, S. Franke-Arnold, S. M. Barnett, R. W. Boyd, and M. J. Padgett, "Angular two-photon interference and angular two-qubit states," Phys. Rev. Lett. **104**, 010501 (2010).

[139] A. C. Dada, J. Leach, G. S. Buller, M. J. Padgett, and E. Andersson, "Experimental high-dimensional two-photon entanglement and violations of generalized bell inequalities," Nature Phys. **7**, 677 (2011).

[140] R. Fickler, R. Lapkiewicz, W. N. Plick, M. Krenn, C. Schaeff, S. Ramelow, and A. Zeilinger, "Quantum entanglement of high angular momenta," Science **338**, 640 (2012).

[141] J. Fulconis, O. Alibart, W. Wadsworth, P. Russell, and J. Rarity, "High brightness single mode source of correlated photon pairs using a photonic crystal fiber," Opt. Express **13**, 7572 (2005).

[142] J. Fan, A. Migdall, and L. Wang, "Efficient generation of correlated photon pairs in a microstructure fiber," Opt. Lett. **30**, 3368 (2005).

[143] R. A. Myers, N. Mukherjee, and S. R. J. Brueck, "Large second-order nonlinearity in poled fused silica," Opt. Lett. **16**, 1732 (1991).

[144] E. Y. Zhu, L. Qian, L. G. Helt, M. Liscidini, J. E. Sipe, C. Corbari, A. Canagasabey, M. Ibsen, and P. G. Kazansky, "Measurement of $\chi(2)$ symmetry in a poled fiber," Opt. Lett. **35**, 1530 (2010).

[145] G. Bonfrate, V. Pruneri, P. Kazansky, P. Tapster, and J. Rarity, "Parametric fluorescence in periodically poled silica fibers," Appl. Phys. Lett. **75**, 2356 (1999).

[146] K. P. Huy, A. T. Nguyen, E. Brainis, M. Haelterman, P. Emplit, C. Corbari, A. Canagasabey, P. G. Kazansky, O. Deparis, A. A. Fotiadi, P. Mégret, and S. Massar, "Photon pair source based on parametric fluorescence in periodically poled twin-hole silica fiber," Opt. Express **15**, 4419 (2007).

[147] E. Y. Zhu, Z. Tang, L. Qian, L. G. Helt, M. Liscidini, J. E. Sipe, C. Corbari, A. Canagasabey, M. Ibsen, and P. G. Kazansky, "Direct generation of polarization-entangled photon pairs in a poled fiber," Phys. Rev. Lett. **108**, 213902 (2012).

[148] Y. Yue, Y. Yan, N. Ahmed, J.-Y. Yang, L. Zhang, Y. Ren, H. Huang, K. M. Birnbaum, B. I. Erkmen, S. Dolinar *et al.*, "Mode properties and propagation effects of optical orbital angular momentum (oam) modes in a ring fiber," IEEE Photon. J. **4** (2012).

[149] A. Canagasabey, C. Corbari, A. V. Gladyshev, F. Liegeois, S. Guillemet, Y. Hernandez, M. V. Yashkov, A. Kosolapov, E. M. Dianov, M. Ibsen *et al.*, "High-average-power second-harmonic generation from periodically poled silica fibers," Opt. Lett. **34**, 2483 (2009).

[150] A. W. Snyder and J. Love, *Optical waveguide theory*, vol. 190 (Springer, 1983).

[151] K. Kawano and T. Kitoh, *Introduction to Optical Waveguide Analysis: Solving Maxwell's Equations and the Schrödinger Equation* (Wiley Online Library, 2001).

[152] V. Brückner, *Elements of Optical Networking* (Springer Fachmedien Wiesbaden GmbH: Vieweg+Teubner Verlag, 2011).

[153] P. Anderson, "Absence of diffusion in certain random lattices," Phys. Rev. **109**, 1492 (1958).

[154] A. Lagendijk, B. van Tiggelen, and D. S. Wiersma, "Fifty years of anderson localization," Phys. Today **62**, 24 (2009).

[155] M. Cutler and N. Mott, "Observation of anderson localization in an electron gas," Phys. Rev. **181**, 1336 (1969).

[156] J. Chabé, G. Lemarié, B. Grémaud, D. Delande, P. Szriftgiser, and J. C. Garreau, "Experimental observation of the anderson metal-insulator transition with atomic matter waves," Phys. Rev. Lett. **101**, 255702 (2008).

[157] J. Billy, V. Josse, Z. Zuo, A. Bernard, B. Hambrecht, P. Lugan, D. Clément, L. Sanchez-Palencia, P. Bouyer, and A. Aspect, "Direct observation of anderson localization of matter waves in a controlled disorder," Nature **453**, 891 (2008).

[158] G. Roati, C. D`Errico, L. Fallani, M. Fattori, C. Fort, M. Zaccanti, G. Modugno, M. Modugno, and M. Inguscio, "Anderson localization of a non-interacting bose–einstein condensate," Nature **453**, 895 (2008).

[159] H. Hu, A. Strybulevych, J. Page, S. E. Skipetrov, and B. A. van Tiggelen, "Localization of ultrasound in a three-dimensional elastic network," Nature Phys. **4**, 945 (2008).

[160] H. De Raedt, A. Lagendijk, and P. de Vries, "Transverse localization of light," Phys. Rev. Lett. **62**, 47 (1989).

[161] D. S. Wiersma, P. Bartolini, A. Lagendijk, and R. Righini, "Localization of light in a disordered medium," Nature **390**, 671 (1997).

[162] T. Schwartz, G. Bartal, S. Fishman, and M. Segev, "Transport and Anderson localization in disordered two-dimensional photonic lattices," Nature **446**, 52–55 (2007).

[163] A. Schreiber, K. N. Cassemiro, V. Potocek, A. Gabris, I. Jex, and C. Silberhorn, "Decoherence and disorder in quantum walks: From ballistic spread to localization," Phys. Rev. Lett. **106**, 180403 (2011).

[164] A. Crespi, R. Osellame, R. Ramponi, V. Giovannetti, R. Fazio, L. Sansoni, F. De Nicola, F. Sciarrino, and P. Mataloni, "Anderson localization of entangled photons in an integrated quantum walk," Nature Photon. **7**, 322–328 (2013).

[165] B. L. Douglas and J. B. Wang, "Efficient quantum circuit implementation of quantum walks," Phys. Rev. A **79**, 052335 (2009).

[166] N. Shenvi, J. Kempe, and K. B. Whaley, "Quantum random-walk search algorithm," Phys. Rev. A **67**, 052307 (2003).

[167] Y. Aharanov, L. Davidovich, and N. Zagury, "Quantum random walks," Phys. Rev. A **48**, 1687 (1993).

[168] N. van Kampen, *Stochastic processes in physics and chemistry* (North holland, 2007).

[169] J. Kempe, "Quantum random walks - an introductory overview," CONTEMPORARY PHYSICS **44**, 307 (2003).

[170] V. Kendon, "Decoherence in quantum walks - a review," (2006).

[171] M. Schlosshauer, *Decoherence and the quantum-to-classical transition*, The Frontiers Collection (Springer, Berlin, 2007).

[172] A. Ambainis, E. Bach, A. Nayak, A. Vishwanath, and J. Watrous, "One-dimensional quantum walks," in "Proceedings of the thirty-third annual ACM symposium on Theory of computing," (ACM, New York, NY, USA, 2001), STOC '01, p. 37.

[173] A. Peruzzo, M. Lobino, J. C. F. Matthews, N. Matsuda, A. Politi, K. Poulios, X. Zhou, Y. Lahini, N. Ismail, K. Wörhoff, Y. Bromberg, Y. Silberberg, M. G. Thompson, and J. L. OBrien, "Quantum Walks of Correlated Photons," Science **329**, 1500 (2010).

[174] M. A. Broome, A. Fedrizzi, B. P. Lanyon, I. Kassal, A. Aspuru-Guzik, and A. G. White, "Discrete Single-Photon Quantum Walks with Tunable Decoherence," Phys. Rev. Lett. **104**, 153602 (2010).

[175] A. Schreiber, K. N. Cassemiro, V. Potocek, A. Gábris, P. J. Mosley, E. Andersson, I. Jex, and C. Silberhorn, "Photons Walking the Line: A Quantum Walk with Adjustable Coin Operations," Phys. Rev. Lett. **104**, 050502 (2010).

[176] D. Pandey, N. Satapathy, M. S. Meena, and H. Ramachandran, "Quantum walk of light in frequency space and its controlled dephasing," Phys. Rev. A **84**, 042322 (2011).

[177] L. Sansoni, F. Sciarrino, G. Vallone, P. Mataloni, A. Crespi, R. Ramponi, and R. Osellame, "Two-Particle Bosonic-Fermionic Quantum Walk via Integrated Photonics," Phys. Rev. Lett. **108**, 010502 (2012).

[178] R. Côté, A. Russell, E. E. Eyler, and P. L. Gould, "Quantum random walk with Rydberg atoms in an optical lattice," New J. Phys. **8**, 156 (2006).

[179] H. B. Perets, Y. Lahini, F. Pozzi, M. Sorel, R. Morandotti, and Y. Silberberg, "Realization of Quantum Walks with Negligible Decoherence in Waveguide Lattices," Phys. Rev. Lett. **100**, 170506 (2008).

[180] F. Zähringer, G. Kirchmair, R. Gerritsma, E. Solano, R. Blatt, and C. F. Roos, "Realization of a Quantum Walk with One and Two Trapped Ions," Phys. Rev. Lett. **104**, 100503 (2010).

[181] J. Du, H. Li, X. Xu, M. Shi, J. Wu, X. Zhou, and R. Han, "Experimental implementation of the quantum random-walk algorithm," Phys. Rev. A **67**, 042316 (2003).

[182] P. W. Shor, "Algorithms for quantum computation: discrete logarithms and factoring," in "Foundations of Computer Science, 1994 Proceedings., 35th Annual Symposium on," (IEEE, 1994), p. 124.

[183] L. K. Grover, "A fast quantum mechanical algorithm for database search," in "Proceedings of the twenty-eighth annual ACM symposium on Theory of computing," (ACM, 1996), p. 212.

[184] Y. Yin, D. E. Katsanos, and S. N. Evangelou, "Quantum walks on a random environment," Phys. Rev. A **77**, 022302 (2008).

[185] J. Peřina Jr, M. Centini, C. Sibilia, and M. Bertolotti, "Random nonlinear layered structures as sources of photon pairs for quantum-information processing," J. Rus. Laser Res. **30**, 508 (2009).

[186] J. Peřina Jr, M. Centini, C. Sibilia, and M. Bertolotti, "Photon-pair generation in random nonlinear layered structures," Phys. Rev. A **80**, 033844 (2009).

[187] N. Inui, Y. Konishi, and N. Konno, "Localization of two-dimensional quantum walks," Phys. Rev. A **69**, 052323 (2004).

[188] A. Oliveira, R. Portugal, and R. Donangelo, "Decoherence in two-dimensional quantum walks," Phys. Rev. A **74**, 012312 (2006).

[189] A. Schreiber, A. Gábris, P. Rohde, K. Laiho, M. Štefaňák, V. Potoček, C. Hamilton, I. Jex, and C. Silberhorn, "A 2D Quantum Walk Simulation of Two-Particle Dynamics," Science **336**, 55 (2012).

[190] K. Watabe, N. Kobayashi, M. Katori, and N. Konno, "Limit distributions of two-dimensional quantum walks," Phys. Rev. A **77**, 062331 (2008).

[191] C. S. Hamilton, A. Gábris, I. Jex, and S. M. Barnett, "Quantum walk with a four-dimensional coin," New J. of Phys. **13**, 013015 (2011).

[192] C. Di Franco, M. Mc Gettrick, T. Machida, and T. Busch, "Alternate two-dimensional quantum walk with a single-qubit coin," Phys. Rev. A **84**, 042337 (2011).

[193] C. Di Franco, M. Mc Gettrick, and T. Busch, "Mimicking the Probability Distribution of a Two-Dimensional Grover Walk with a Single-Qubit Coin," Phys. Rev. Lett. **106**, 080502 (2011).

[194] M. Mohseni, P. Rebentrost, S. Lloyd, and A. Aspuru-Guzik, "Environment-assisted quantum walks in photosynthetic energy transfer," The Journal of Chemical Physics **129**, 174106 (2008).

[195] M. B. Plenio and S. F. Huelga, "Dephasing-assisted transport: quantum networks and biomolecules," New J. Phys. **10**, 113019 (2008).

[196] H. Obuse and N. Kawakami, "Topological phases and delocalization of quantum walks in random environments," Phys. Rev. B **84**, 195139 (2011).

[197] J. Košík, V. Bužek, and M. Hillery, "Quantum walks with random phase shifts," Phys. Rev. A **74**, 022310 (2006).

[198] *ImagEM, EM-CCD Camera C9100-14 (Hamamatsu).*

[199] S. Hisatake, K. Shibuya, and T. Kobayashi, "Ultrafast traveling-wave electro-optic deflector using domain-engineered LiTaO[sub 3] crystal," Appl. Phys. Lett. **87**, 081101 (2005).

[200] S. Hisatake, K. Tada, and T. Nagatsuma, "Linear time-to-space mapping system using double electrooptic beam deflectors," Opt. Express **16**, 21753 (2008).

[201] D. Čapeta, J. Radić, A. Szameit, M. Segev, and H. Buljan, "Anderson localization of partially incoherent light," Phys. Rev. A **84**, 011801 (2011).

[202] L. Mandel and E. Wolf, *Optical coherence and quantum optics* (Cambridge university press, 1995).

[203] D. N. Christodoulides, E. D. Eugenieva, T. H. Coskun, M. Segev, and M. Mitchell, "Equivalence of three approaches describing partially incoherent wave propagation in inertial nonlinear media," Phys. Rev. E **63**, 035601 (2001).

[204] U. M. Titulaer and R. J. Glauber, "Density operators for coherent fields," Phys. Rev. **145**, 1041 (1966).

[205] A. Valencia, J. P. Torres *et al.*, "Tailoring the spectral coherence of heralded single photons," Opt. Lett. **34**, 1177 (2009).

[206] A. F. Abouraddy, G. Di Giuseppe, D. N. Christodoulides, and B. E. A. Saleh, "Anderson localization and colocalization of spatially entangled photons," Phys. Rev. A **86**, 040302 (2012).

[207] G. Di Giuseppe, L. Martin, A. Perez-Leija, R. Keil, F. Dreisow, S. Nolte, A. Szameit, A. F. Abouraddy, D. N. Christodoulides, and B. E. A. Saleh, "Einstein-podolsky-rosen spatial entanglement in ordered and anderson photonic lattices," Phys. Rev. Lett. **110**, 150503 (2013).

[208] K. W. Chan and J. H. Eberly, "Observable phase entanglement," arXiv preprint quant-ph/0404093 (2004).

[209] J. Peřina Jr, "Quantum properties of counterpropagating two-photon states generated in a planar waveguide," Phys. Rev. A **77**, 013803 (2008).

[210] S. Karbasi, K. W. Koch, and A. Mafi, "Modal perspective on the transverse anderson localization of light in disordered optical lattices," JOSA B **30**, 1452 (2013).

[211] J.-M. Jin, J. Jin, and J.-M. Jin, *The finite element method in electromagnetics* (Wiley New York, 2002).

[212] P. Yeh, A. Yariv, and C.-S. Hong, "Electromagnetic propagation in periodic stratified media. i. general theory," JOSA **67**, 423 (1977).

[213] P. Yeh, *Optical waves in layered media*, Wiley series in pure and applied optics (Wiley, 2005).

[214] N. Ashcroft and N. Mermin, *Solid State Physics* (Cengage Learning India Private Limited, 2011).

[215] B. R. West and A. S. Helmy, "Properties of the quarter-wave bragg reflection waveguide: theory," JOSA B **23**, 1207 (2006).

[216] Y. Saad, *Iterative methods for sparse linear systems* (Siam, 2003).

[217] N. W. Ashcroft and N. D. Mermin, *Solid State Physics* (Wiley, 1981).

[218] W. H. Press, *Numerical recipes 3rd edition: The art of scientific computing* (Cambridge university press, 2007).

[219] J. Peřina, *Quantum statistics of linear and nonlinear optical phenomena* (Springer, 1991).